Award Number: DE-FE 31548

Project Title: HIGH TEMPERATURE ELECTROCHEMICAL SENSORS FOR IN-SITU CORROSION MONITORING IN COAL-BASED POWER GENERATION BOILERS

Principal Investigator: Dr. Xingbo Liu
(304) 293-3339
Xingbo.Liu@mail.wvu.edu

Project Period: Jan 1, 2018, to Dec 31, 2022

Recipient Organization: West Virginia University

Submission Date: Mar 31, 2023

DUNS Number: **929332658**

Recipient Organization (Name and Address): West Virginia University
Morgantown, West Virginia 26506

Project/Grant Period (Start Date, End Date): 01/01/2018 to 12/31/2022

Reporting Period End Date: Dec 31, 2022

Report Term or Frequency: Final Technical Progress Report

Signature of Submitting Official (electronic signatures (i.e., Adobe Acrobat) are acceptable)

03/31/2023

HIGH TEMPERATURE ELECTROCHEMICAL SENSORS FOR IN-SITU CORROSION MONITORING IN COAL-BASED POWER GENERATION BOILERS

1. EXECUTIVE SUMMARY

In this project, we successfully achieved the goals we proposed: ① optimization and development of electrochemical sensor, ② sensor construction and package, ③ sensor testing @Longview Power Plant and data analysis, ④ lab-scale sensor optimization and corrosion database development, ⑤ electrochemical and corrosion monitoring validation and ⑥ TEA.

2. OBJECTIVES

The primary objectives of this project are (1) to validate the effectiveness of our pervious electrochemical sensor for high temperature (HT) corrosion in coal-based power generation boilers; (2) to optimize our HT sensor (current in technology readiness level (TRL) 6 to reach TRL-7, and (3) to develop a pathway toward commercialization of such technology.

Based on our project timeline, the milestone updates in this quarter mainly include “Task 1 Project Management”, “Subtask 2.1 Design & construct sensors”, “Task 3 Developing signal processing and communication instruments”, “Subtask 5.1 Lab-scale sensor optimization”, “Subtask 5.2 Electrochemical and corrosion monitoring validation” and “Subtask 6.1 NPV model & uncertainty analysis”.

3. ACCOMPLISHMENTS

Table 1. Milestone Status Report

Milestone Number	Assoc. SOPO Task(s)	Milestone Title/ Description	Planned Completion Date	Actual Completion Date	Percent Completed	Verification Method	Comments
M1	Task 2.1	Design & construct sensors/Design and	6/30/2018	9/30/2018	100%	Designed by CAD; Fabricated by	Design had been finished early, but it

		fabricate the sensor and support system				machining work	took too long to fabricate the sensor out.
M2	Task 2.2	Sensor Packaging/Develop a package providing high safety and performance	9/30/2018	09/30/2018	100%	Design and testing in Lab	Delayed by the sensor fabrication
M3	Task 4.2	Sensor testing	12/31/2018	12/19/2018	100%	Temperature control and observation of the electrochemical noise signals	The testing during phase 1 has been finished
M4	Task 6.1	NPV model & uncertainty analysis/Complete the NPV model and uncertainty analysis	6/30/2019	12/30/2022	100%	Unscented Kalman filter, Modeling and testing	
M5	Task 6.2	NEMS model and economic analysis/Complete the NEMS model	6/30/2020	12/30/2022	100%		

		and economic analysis					
M6	Task 6.2	Accurate reporting of in-situ info/Demonstrate the corrosion sensor can accurately report in-situ information on corrosion progress of the most critical components (superheater tubes and water wall tubes) in a utility-scale A-USC boiler.	12/31/2020	12/30/2022	100%	The in-situ corrosion information revealed by the corrosion sensor will be verified through the model used to simulate the working environment	The model is still in progress to optimize the calculation process; The accuracy of the calculation of corrosion rate by utilizing the EN data is still being optimized.

4. PROGRESS OF THE PROJECT

Corrosion requires prevention and maintenance across many industries, and the total direct cost of corrosion for industrialized countries has typically been estimated to be 3% of GDP. A 2002 study initiated by the National Association of Corrosion Engineers estimated that 25% of that cost could be saved using known preventive techniques. That study also segmented the United States' estimated $276B direct annual cost of corrosion into different industries. The utilities industry has a large corrosion burden of $47.9B—with $7B direct, or $17.3B indirect, costs for electrical utilities. The estimated direct costs for fossil fuels is $1.9B, of which the Electric Power Research Institute estimates a large portion ($590M) is due to fireside corrosion—the target of this project. But the indirect costs may be higher, as it is estimated that 50% of unplanned downtime in power plants is caused by contaminants in the water-steam circuit, primarily due to corrosion. Corrosion becomes an even greater challenge as fossil fuel-power stations move to ultra-supercritical operation to enhance efficiency. The higher temperatures cause more corrosion and make monitoring more difficult.

Task 1 Project Management and Planning

The WVU management team is responsible for project management activities: reporting, organizing, and hosting project meetings, tracking project milestones, and substantiating the decision metrics.

Task 2 Sensor Development & Optimization

Task 2.1 Design & construct sensors

The set-up of electrochemical sensor

Figure 1 depicts the schematic of the electrochemical sensor set-up. It is clearly shown that it includes three units: electrochemical sensor, data acquisition system and temperature controller. The main body of this sensor is made of 304 stainless steel which can effectively resist high temperature oxidation. All the lead wires, i.e., nichrome, are shielded in the stainless-steel tube to avoid undesirable oxidation. In the electrochemical sensor, there are several electrodes/parts: two identical working electrodes, one reference electrode, an electric resistor and one thermocouple. All these signals including the electrical resistance, the potential noise between the reference electrode and one working electrode, the current noise between two identical working electrodes, the actual exposure temperature, are monitored and recorded by the data acquisition system. The actual exposure temperature on the surface of these working electrode is automatically controlled by the feed of compressed air. The flow rate of compressed air is automatically adjustable based on the difference between the actual temperature and target temperature.

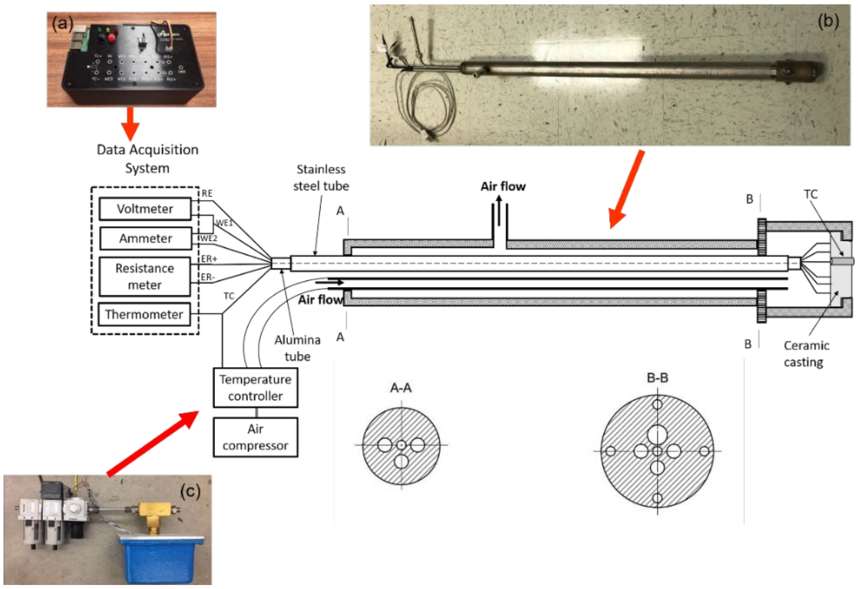

Figure 1: the schematic of the electrochemical sensor set-up

In the electrochemical sensor, the electric resistance and thermocouple are commercially available. The working electrode is TP347H, the same materials used as the superheat in the Longview Power Plant. The reference electrode is a platinum rod with a diameter of 5 mm.

Task 2.2 Sensor packaging

Data acquisition system

① Requirements

For the data acquisition system, named PIECES therefore after, its requirements for each measurement type are described in detail below.

TC: The thermocouple requires a voltage measurement between its two terminals. This voltage indicates the temperature differential between the sensor in the boiler and the cold junction at the measurement interface in PIECES. To refer this temperature differential to an absolute temperature, PIECES must include a temperature sensor. Additionally, a mathematical conversion function is applied to convert the thermocouple voltage value to a temperature value—the conversion function depends on the type of thermocouple, which was not known at the time of PIECES hardware design. To determine generic thermocouple measurement requirements, Figure 2 shows the temperature-to-voltage relationship for several standard thermocouple types over the temperature range of interest—room temperature, the expected temperature range in the boiler (300°C-450°C), as well as the temperature for ultra-supercritical boilers (760°C). The Figure 2 also shows the slope with respect to temperature and the error range. These thermocouple characteristics come from Fluke’s online calculator. Based on these characteristics, the requirements for measuring the thermocouple include a ±100 mV range to provide overhead for up to 60 mV readings, an offset of 100 µV or less to keep the uncalibrated measurement offset on the same order as the thermocouple error (the offset can be further calibrated to reduce the temperature uncertainty), and a resolution of 50µV or less to resolve 2°C temperature changes for the least sensitive thermocouples.

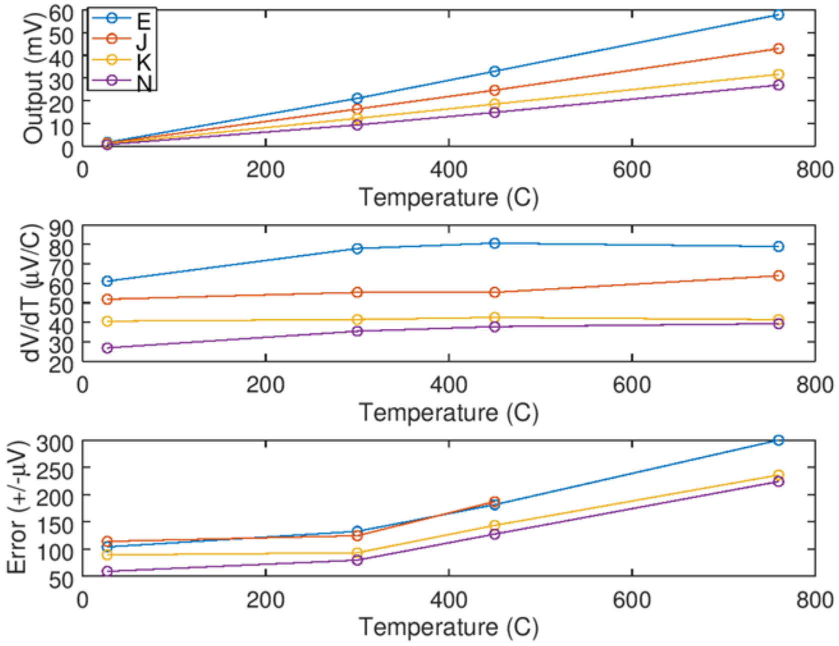

Figure 2: Standard thermocouple characteristics. (top) Voltage-to-temperature relationship. (middle) Slope of voltage with respect to temperature (i.e., Seebeck coefficient). (bottom) Standard limit of error in terms of voltage.

ER: The electric resistance sensor requires a measurement of the resistance of a wire inside the sensor. The expected range of resistance values is 0.1Ω to 5Ω, and it is desired to resolve resistance changes of 0.01Ω. For such small resistance values, the resistance of the cable becomes a significant source of error, so it is recommended to use a four-point Kelvin connection where separate pairs of leads are used to stimulate and measure the resistor.

Table 2. Sensor measurement requirements. Spectral noise given at 0.1Hz.

		Min	Max	Offset	Resolution	Sample Rate
TC		-100mV	100mV	100µV	50µV	<10sps
ER		0.1Ω	5Ω	0.1Ω	0.01Ω	<10sps
ECN	Voltage	-300mV	300mV	100µV	10^{-12} V^2/Hz	<10sps
	Current	-50µA	50µA	50nA	2.5×10^{-20} A^2/Hz	<10sps

ECN: The ECN sensor requires multiple measurement options. If a reference electrode is used, then voltage should be measured between each working electrode and the reference electrode. Otherwise, voltage should be measured between each pair of working electrodes.

This voltage measurement should have a high input impedance. In addition to voltage measurement, current should be measured between every pair of working electrodes. The current measurement should not affect the WE voltages, so a very small shunt resistor or a transimpedance amplifier should be used to convert the current into a voltage for measurement.

ECN measurement requirements can be determined from the data of the previous sensor (Figure 3). The current covers a range from 1.6µA to 20.5µA, so a ±50µA range and a 50nA uncalibrated offset is sufficient. The voltage covers a range from -192mV to 7.8mV, so a ±300mV range and a 100µV uncalibrated offset is sufficient. Since the ECN data will be analyzed in spectral form, the critical resolution requirement is the low-frequency noise, which should be low enough to not affect the measurement. Noise accumulates as a sum of squares, so if the squared noise density of the measurement interface is 30-times less than the squared noise density of the sensor, then the measurement interface will have approximately 0.1% effect on the measurement. The corresponding voltage and current noise for 0.1% effect at 0.1Hz is 10-12 V2/Hz and 2.5x10-20 A2/Hz, respectively. Although this resolution only specifies the noise at one frequency, a chopper-modulated input will typically be used in precision interfaces, which keeps the noise relatively flat at lower frequencies, where the sensor noise increases.

Other requirements: The measurement capabilities should be configurable to handle sensors with different sampling rates, different combinations of electrodes, etc. For all of the measurement types, the sample rate does not need to be greater than a few samples per second. To handle different combinations of electrodes, the electrode connectors should be individual and interchangeable. Banana connectors will be used since they are standard on electrochemical measurement equipment.

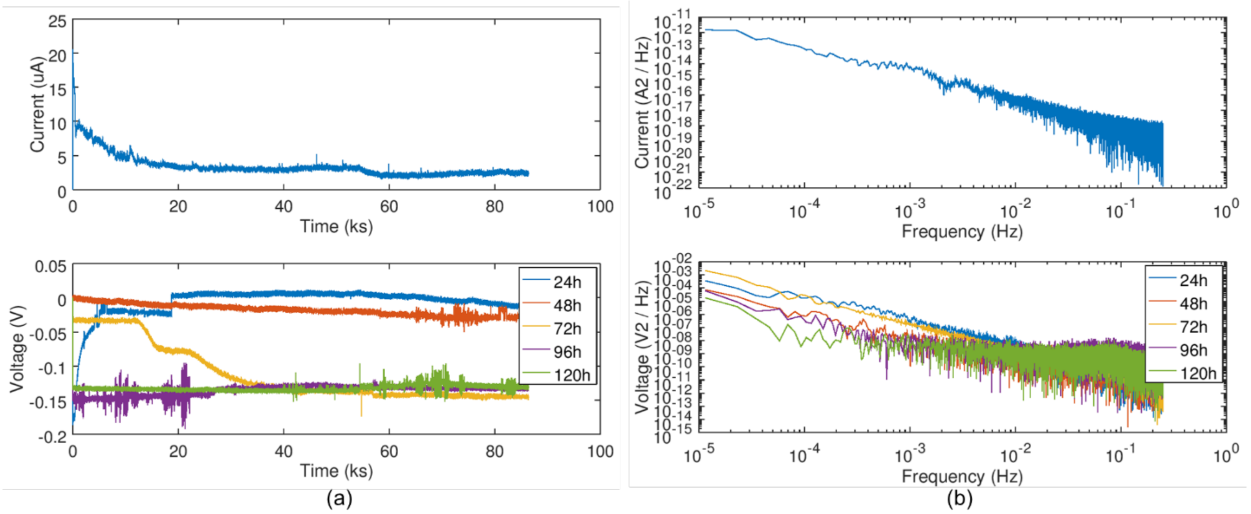

(a) (b)

Figure 3: Electrochemical noise (ECN) measurements from the original WVU corrosion sensor. Both current (top) and voltage (bottom) are shown. (a) Time-series data. (b) Frequency-domain data via FFT.

② Design

A modular approach has been used in the design of PIECES. This approach helps to minimize cost and risk in this first prototype. Figure 4 shows the architecture of PIECES. The Front Panel and Measurement Board are custom circuit boards, while the Embedded Controller and Radio are off-the-shelf modules. The Front Panel provides the physical user interface and provides the central set of electrical connections. Only minimal electronics components are placed on the Front Panel (just LEDs and buttons) because the purpose of the Front Panel is to connect to the sensors and to be a “dock” for the other modules. The Measurement Board and Embedded Controller attach to the bottom of the Front Panel. The bulk of the components are placed on the smaller Measurement Board; placing the components on a smaller board reduces the assembly cost, which is based on board area for small volume manufacturing. Separating the measurement circuitry also minimizes the cost of manufacturing any revisions.

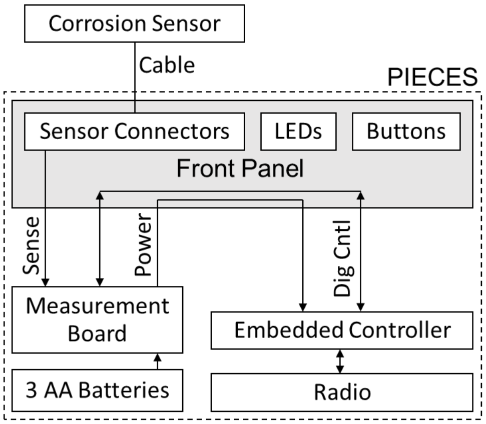

Figure 4: Modular architecture of PIECES.

Front Panel

The Front Panel of PIECES is shown in Figure 5. It measures 4”x8”. This panel will be mounted on an enclosure that will contain the Measurement Board, the Embedded Controller, the Radio, and the batteries. The Front Panel provides 14 banana plug receptacles for all of the sensor electrode Configurations shown in Figure 1. Banana plugs were recommended since they are standard for electrochemistry measurement equipment. While four-point resistance connectors are provided on the Front Panel, two-point resistance measurements can be performed by shorting the RV* plugs to the RI* plugs. Two buttons (B*) and three LEDs (L*) in the top-left are firmware-Configurable and will allow the user to set modes and view status. The firmware and settings will be developed in the next phase of the project. The top-left corner of the Front Panel is designed to break off to expose the USB and ethernet connections of a Raspberry Pi when that is used as the Embedded Controller.

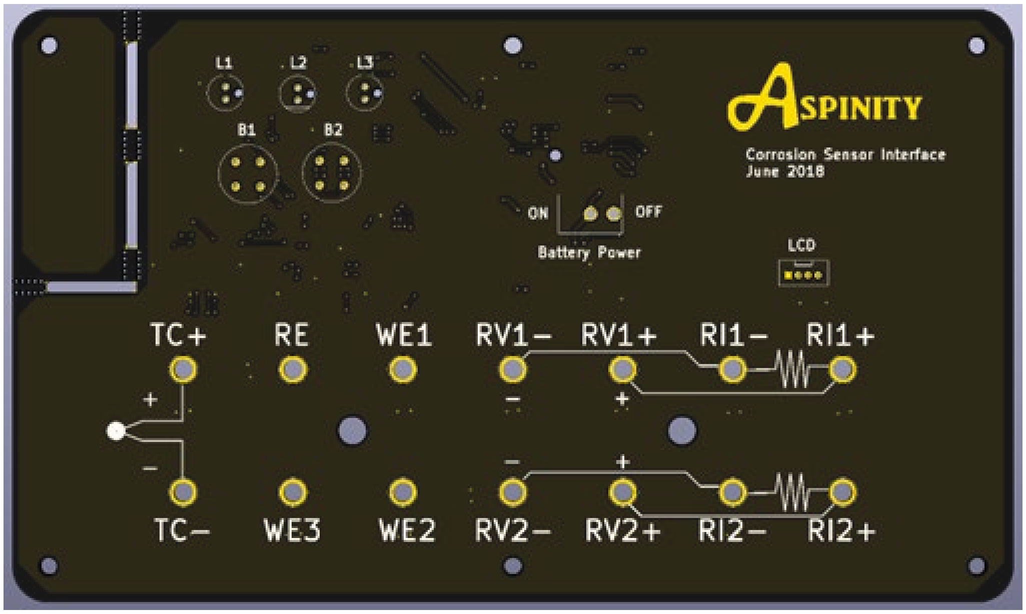

Figure 5: Front Panel of PIECES

Embedded Controller

The underside of the Front Panel provides connectors for multiple types of readily available commercial embedded controllers. This provides options to begin with an easy-to-use, but inefficient, controller to quickly prepare the firmware and iterate on changes as needed, and then to swap to a more efficient controller once the requirements are better known. The three types of embedded controllers that may be used are described below.

Raspberry Pi ($35): The Raspberry Pi is a popular computer platform that runs a full Linux distribution. This allows software—such as for controlling the measurement board and logging and visualizing data—to be developed rapidly with high-level software such as Python and GNU Octave. The use of high-capacity micro-SD cards allow long-term local data logging, and USB connections make it easy to transfer data from PIECES or to load user configureuration files. Ethernet and Wi-Fi allow PIECES to easily work with cloud-based data systems.

Telos (~$100): The Telos “mote” is a legacy wireless sensor networking platform that supports long battery life for low-data-rate applications, such as corrosion monitoring. It uses an 802.15.4 radio, as is common in industrial sensor networks. It has been used extensively for wireless sensor network research at WVU, so a well-developed networking codebase built upon TinyOS is available that will accelerate development.

Panstamp ($20): The Panstamp module uses similar hardware and the same radio as the Telos. It supports lower power consumption and is more readily available. It has been used in Aspinity’s other projects, but the wireless networking codebase is not as well developed as the Telos code base, so it will be incorporated later.

Measurement Board

The measurement board provides a Configurable interface for voltage, current, and resistance measurements on different combinations of electrode connections. These measurements and Configurations are controlled by the Embedded Controller using standard chip-to-chip serial interfaces (SPI for the measurements and I2C for the electrode Configurations).

The measurement board has been designed around a precision voltage-measurement core, which can also measure current and resistance by adding additional components. Electronically controlled switches are used to connect the electrodes in the desired combinations and to switch in resistors and current sources to achieve current- and resistance-measurements with a single voltage-measurement core. The motivation for basing all measurements around a single core is that precision measurement devices with low drift and low temperature dependence will be the most expensive part of the Measurement Board. Electronically controlled switches with sub-ohm on-resistance and sub-nanoamp leakage currents are readily available at lower costs than the measurement component, so the cost can be minimized by using switches to reconfigure a single core that meets the specifications, rather than replicating precision measurement channels.

The principle of performing the required measurements with a single voltage-measurement core is shown in Figure 6 and described below.

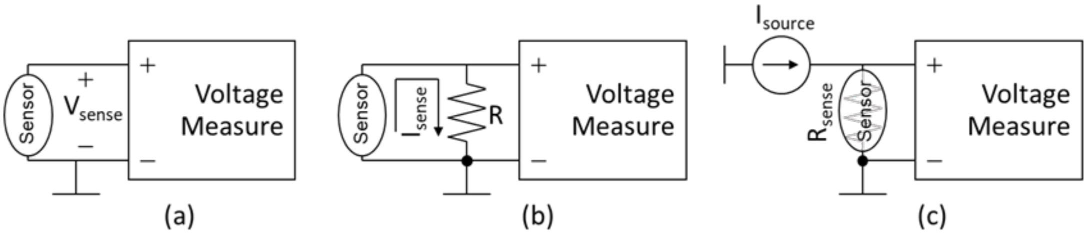

Figure 6: Different measurements using a common voltage-measurement core. (a) Voltage. (b) Current. (c) Resistance

(a) The Voltage Measure device measures the open-circuit potential of the sensor electrodes.

(b) The Sensor current is converted to a voltage by the shunt resistor, *R*, which is switched in across the measurement terminals only when measuring current. This is the same current-measurement principle used in a multimeter. ECN current measurements typically use transimpedance amplifiers—often called zero-resistance ammeters (ZRA) in the electrochemistry field—to minimize the voltage drop across the sensor terminals. That approach has not been used in PIECES due to a desire to accurately measure the true current between a pair of electrodes, whereas a transimpedance amplifier would only measure the current out of a single electrode. A precision Voltage Measure device allows a small shunt resistor to be used while still providing precise current measurement. This small resistor approximates the low-input impedance of a transimpedance amplifier so that the effect on the electrode voltages is small.

(c) To measure the Sensor's resistance, an on-board current source, I_{source}, stimulates the Sensor, while the resistance-induced voltage is measured by Voltage Measure. An adjustable current source allows measurement of different ranges of sensor resistance. Since the cable resistance will affect the result, separate connections from the Sensor to I_{source} and Voltage Measure are provided to cancel out the cable resistance.

For the Voltage Measure core, we have selected the ADS1292 analog front-end chip, depicted in the center of Figure 7. The ADS1292 is marketed for high-precision electrocardiogram measurements, but it also has an excellent combination of specifications for the needs of this project. It integrates two measurement channels, each with a low-offset, low-noise instrumentation amplifier (IA) and a 24-bit analog-to-digital converter (ADC). It also includes a low-noise voltage reference and a spare operational amplifier (OPA). We are using the first measurement channel for the Voltage Measure core, and the other measurement channel is being used in combination with the spare op-amp in a feedback loop as the current source I_{source}.

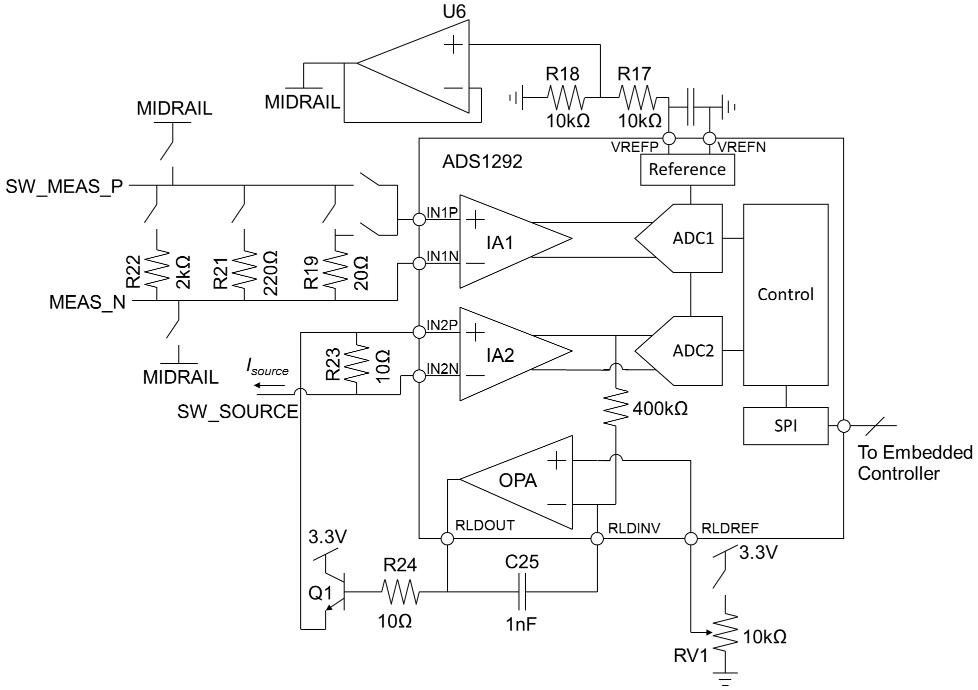

Figure 7: Configurable measurements around the ADS1292 voltage-measurement core.

The circuitry that surrounds the ADS1292 for performing sensor measurements is shown in Figure 7. The integrated precision reference is used for the data converters (ADC1/ADC2) and is also divided by R17/R18 to generate the MIDRAIL reference for the board—this results in 1.2V for MIDRAIL, which is half of the measurement range, but not half of the supply voltage (3.3V). A switching network (not shown in the Figure) connects different pairs of electrode terminals to the positive (SW_MEAS_P) and negative (MEAS_N) measurement inputs, which connect to the ADS1292's first measurement channel. Switches on SW_MEAS_P and MEAS_N allow either terminal to be referenced to MIDRAIL, and also allow different shunt resistors (R19, R21, R22) to be added for different current measurement ranges. The reason that two switches are used to connect to IN1P is so that the smaller resistor (R19) can effectively be Kelvin-connected to cancel the resistance of its switch, which would otherwise contribute an additional 0.5Ω that would be difficult to accurately account for. Precision wire-wound resistors are used for R19, R21, and R22 because they are critical for accurate current measurement. An anti-aliasing filter (not shown) is placed after IA1, with its corner frequency set by an external capacitor. Additionally, unpopulated RC footprints have been included at the input to IN1P/IN1N to provide the option for additional anti-alias filtering.

The bottom half of the schematic is used to generate the current I_{source} for resistance measurement. This current is generated by a feedback loop in which Q1 drives I_{source} onto R23 to translate that current into a voltage that is amplified by IA2. The internal Configurations of the ADS1292 allow either the positive or negative output of IA2 to connect to the inverting terminal of OPA via a 400kΩ resistor. C25 is connected in negative feedback around OPA to integrate the difference between IA2's output and the voltage set by potentiometer RV1. The output of this integration drives the base of Q1 to complete the loop. Q1 is used to buffer the output of OPA from I_{source}, which is too high (10mA) for this integrated op-amp. The loop will hold I_{source} steady, and the resulting current is determined by the setting on RV1 and by the gain of IA2, which is programmable via SPI. That way, the current can be trimmed manually with RV1, and then the gain of IA2 can be adjusted automatically to measure different resistance ranges. A precision wire-wound resistor is used for R23.

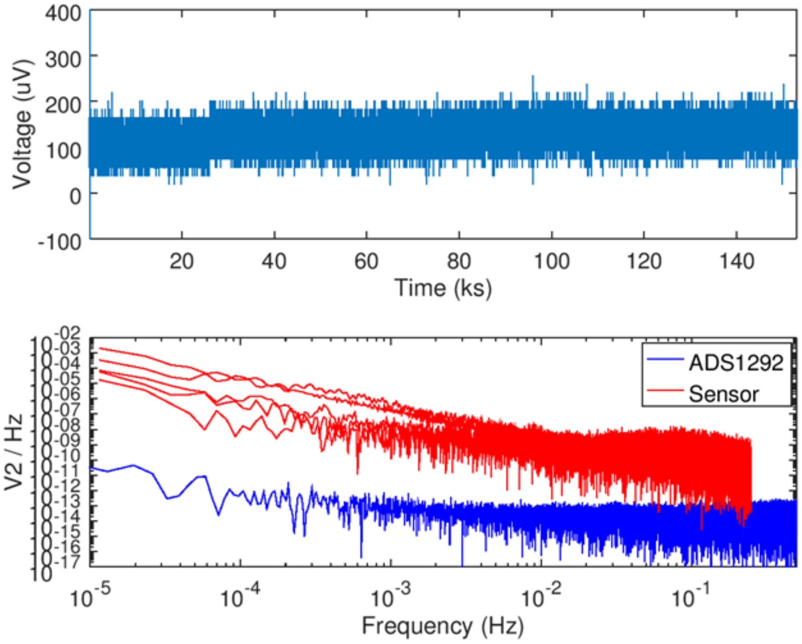

Figure 8: Ultra-low frequency characteristics of the ADS1292 compared to the sensor signal. The Sensor traces are the same five voltage traces from Figure 9(b). The ADS1292 noise is much lower than the sensor signal, so the measurement path will not affect ECN quality.

The ADS1292 was chosen for its low offset and low noise, but the datasheet does not provide specifications for operation at the ultra-low frequencies used in this project. To ensure that the part will work, its voltage-measurement noise was obtained in a similar setup as will be used for this project. To measure the noise, the input terminals were shorted, and the voltage was sampled once per second for approximately 1.5 days. The time-series data and spectral data are shown in Figure 8. In the bottom plot, the low-frequency noise of the ADS1292 is low enough to not affect the sensor readings, in fact it is ten times lower than the required resolution value in Table 2.

The sensor terminals and assorted resistors are configured for different measurements using a set of 24 digitally controlled switches. We have chosen the 8-switch MAX14662 chip, which have an on-resistance less than 0.5ohm and a sub-nanoamp leakage current. Figure 9 shows a schematic of the electrode switch array. The set of 14 electrodes at the top can be connected to the four bottom nets in different combinations to support the desired measurements. The four bottom nets consist of SW_MEAS_P and MEAS_N, which are the differential inputs to the measurement block (Figure 8), as well as SW_SOURCE and SW_BOTTOM, which are the current source for resistance measurement. The resistor from SW_BOTTOM to ground serves to shift the terminal voltages up to the middle of the common-mode range during resistance measurement—a resistor can be used because the current is known (10mA) and is used instead of a direct connection to MIDRAIL to reduce the output-impedance requirements of the MIDRAIL buffer.

Measurement Specifications

The design described above meets the measurement requirements outlined in Table 1.

TC: The ADS1292 provides a measurement range up to ±1.2V and an offset of 100µV. The integrated noise is 37µVrms.

ER: The nominal source current for resistance measurement will be 10mA (although this can be changed programmatically by adjusting the gain of IA2). At 10mA, the voltage range for a resistance range of 0.1Ω to 5Ω will be 1mV to 50mV, which is reliably measured by the ADS1292. Furthermore, the resolution requirement of 0.01Ω results in 100µV, which can be resolved reliably.

ECN: (voltage) The ADS1292 provides a measurement range up to ±1.2V and the ultra-low frequency noise is 300-times less than the sensor signal (see Figure 8). (current) The switchable shunt resistors provide a current measurement offset as low as 50nA and a range up to 60mA. The largest resistor has been chosen to match the spot noise requirement.

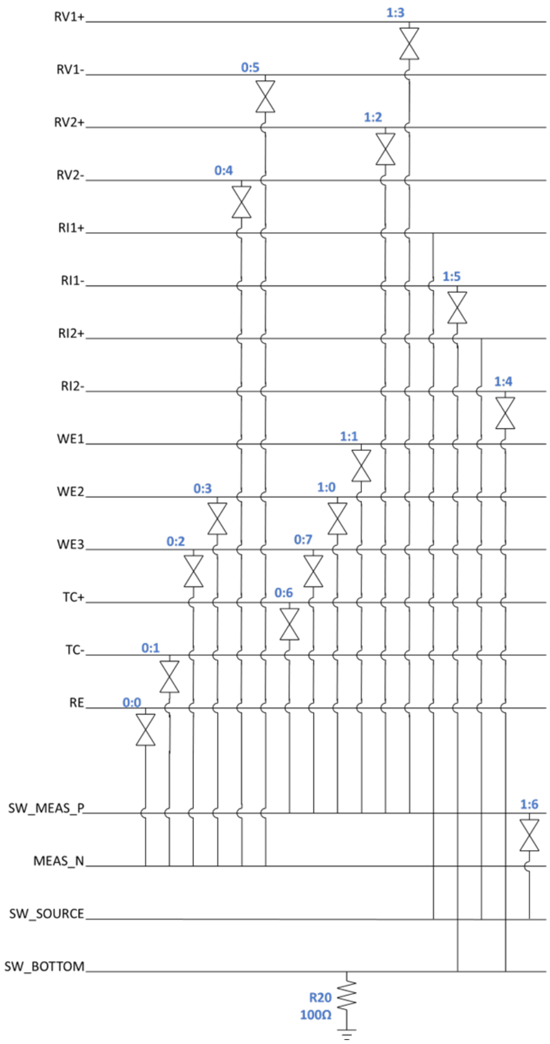

Figure 9: Electrode switch array. Each switch has two numbers—the left number is the chip that contains that switch and the right number is which switch in the switch chip.

Operating Temperature Range

PIECES will operate outside of the boiler where the temperature is much lower. PIECES is built from components to reliably operate at a temperature up to 85°C.

1. Embedded Controllers: The Telos controller is specified to operate up to 85°C and the Panstamp's components are also specified to operate up to 85°C. The Raspberry Pi is specified for 85°C when the ethernet interface is not used.
2. Measurement Board: All of the parts on the Measurement Board are specified for 85°C or higher, but the impact of the temperature dependence should be also considered.
    a. Voltage Measurement: The reference in the ADS1292 has a temperature coefficient of -45ppm/°C. From room temperature to 85°C the full-scale range will change by approximately 0.2%.

b. Current Measurement: In addition to the reference's temperature coefficient, current measurement will be susceptible to the temperature coefficient of the shunt resistors. The shunt resistors are wire-wound and have a low temperature coefficient of ±20ppm/°C. Additionally, the electronically controlled switches have a leakage current that rises to 2nA at 85°C. The most sensitive path is the positive measurement input, but its maximum leakage at 85°C is just 20nA, which is still within the current measurement offset range of 50nA.
c. Resistance Measurement: Being built from the same components as the voltage and current measurements, resistance measurement will have a similar temperature coefficient.

All combined, PIECES will conservatively operate up to 85°C with less than 100ppm/°C temperature dependence.

Analysis of Power Consumption

A short analysis of PIECES' power consumption is provided to estimate the battery life. It is assumed that there are four operating modes with different power levels: sleep, TC or ECN measurement, ER measurement (which consumes more power because of the stimulating current source), and wireless communication. The estimated supply current in each of these modes is shown in Table 3. The digital supply current (DVDD) includes the quiescent current of the TPS78330 regulator and the supply current of the Telos mote with radio, and the digital supply of the ADS1202. The analog supply current (AVDD) includes another regulator, the analog supply of the ADS1292, the MCP6001 op-amp, I_{source}, potentiometer, and Vref divider. For the sake of this analysis, assume that PIECES spends 2ms on each measurement and 1ms to transmit all of the measurements. PIECES will take 9 measurements (6 ECN, 2 ER, and 1 TC), so it will spend 14ms in TC/ECN mode, 4ms in ER mode, 1ms in Comm mode, and 991ms in Sleep mode. The average supply current will be 105uA, which will last for approximately 19 months on AA batteries. This battery life can be increased by using the Panstamp controller instead of the Telos, which has 20x lower sleep current, by reducing I_{source}, by taking less frequent readings of some or all sensors (as opposed to reading every sensor every second), etc. Additionally, the sub-milliamp average supply current allows energy harvesting to be used to enable battery-less operation.

Table 3: Estimated supply current of PIECES in different operating modes.

	Sleep	**TC/ECN**	**ER**	**Comm**
DVDD	0.026mA	0.575mA	0.575mA	20mA
AVDD	0	0.427mA	10.727mA	0
Total	0.026mA	1.003mA	11.3mA	20mA

Measurement Testing

Several tests were performed to verify the measurement performance of the PIECES device. These include a long noise measurement to determine the low frequency noise, as well as sweeps of voltage, current, and resistance to verify accuracy over the specified measurement range.

(1) Noise measurement

Since the measurement interface is responsible for reading the Electrochemical Noise (ECN) measurement, it is critical that the measurement interface provides a low input noise so that it does not impact the ECN measurement. To determine the noise floor of the device, the WE1 and WE2 terminals were shorted and the voltage was sampled 10 times per second for 60 hours. The results are shown in Figure 10. The top pane shows the raw time-based data. The device automatically performs offset correction at power up and then once per hour during operation, which results in a very low offset during the measurement. It can be seen that the maximum deviation is ~15µV from 10-12 hours. The square-wave deviations where the offset oscillates up and down for the first 20 hours are the result of automatic offset nulling and correspond to the time when a laptop was sitting next to the device. Overall, the entire duration, the noise is $3.2\mu V_{rms}$. The frequency distribution of the noise is shown in the bottom pane. In the Phase 1 report it was determined that if the noise is below 10^{-12} V^2/Hz at 0.1Hz then the impact on the sensor readings will be less than 0.1%. It can be seen from the bottom pane that the noise of the measurement interface is sufficiently below the target. It appears that the once-per-hour offset-nulling may have caused small spectral speaks at harmonics of 0.278mHz. These are still below the noise floor that is required for ECN, but could be further minimized with dithering.

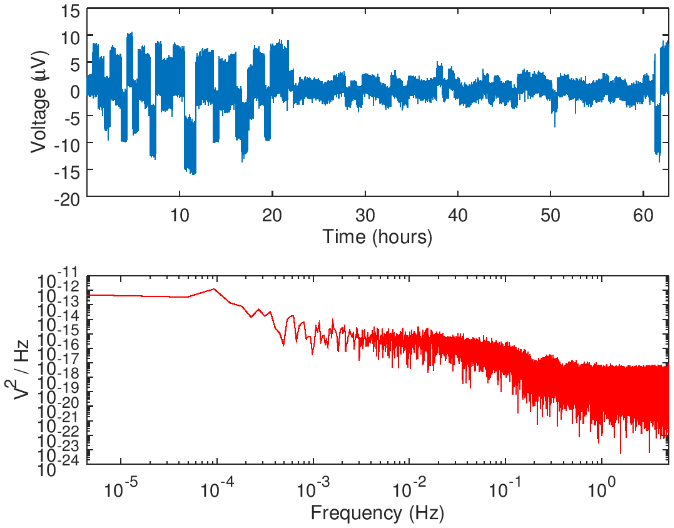

Figure 10: Voltage noise measurement

(2) Voltage sweep

The accuracy of voltage measurement was determined by sweeping the input voltage and measuring the resulting error with respect to the true reading from a Siglent SDM3055 multimeter. The results are shown in Figure 11, where the difference between the PIECES measurement and the multimeter measurement are plotted on the y-axis. This experiment was done with two different PIECES modules to verify consistency. The input range is approximately -1.2V to 1.8V, which is limited by the 3V supply used for the Measurement Board. This range safely covers the range of voltages previously seen for the ECN sensor, which stayed within the range of -0.3V to 0.3V. It can be observed from the Figure that the error is a function of the input voltage and creates 0.176mV error per 1V increase for the first PIECES module and 2mV error per 1V increase for the second PIECES module. Or in other words, the gain error of the measurement is a maximum of 0.2%. Any gain error on the Measurement Board is likely caused by the reference voltage that is used by the analog-to-digital converter, and which will vary from module to module and is specified for up to 0.5% variation.

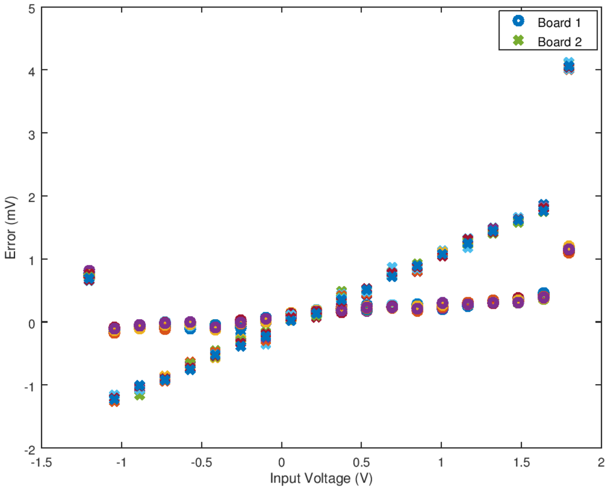

Figure 11: Voltage measurement error

(3) Current sweep

Current measurement was tested by measuring over a range of current values. The results are shown in Figure 12. Positive and negative current measurements are shown for two different PIECES modules to verify consistency. The true current was measured using the Siglent SDM3055 multimeter. The current measurement tracks the true value from 30nA to 1mA. Current variations below 30nA can still be resolved, but a constant offset will be observed.

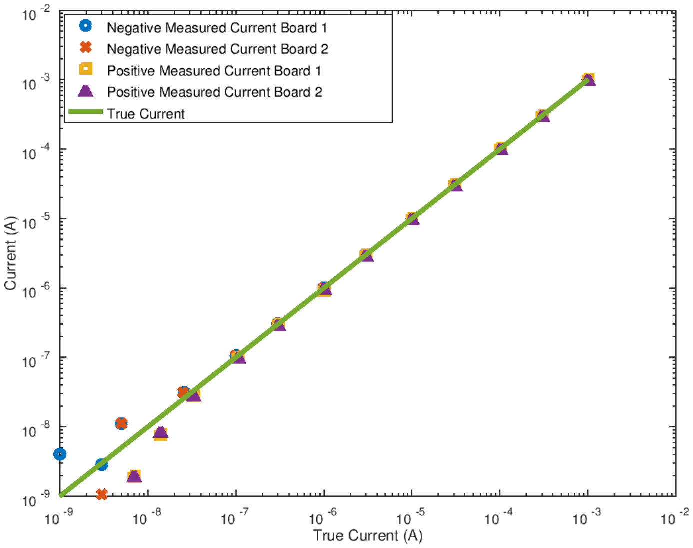

Figure 12: Current measurement sweep

(4) Resistance sweep

Resistance measurement was tested by measuring over a range of resistors. The results are shown in Figure 13. The true resistance was measured using the Siglent SDM3055 multimeter. Small diameter wire-wrap wire was used to create smaller resistances and carbon composite resistors were used for the larger values. The resistance deviates at low values due to a measurement offset of a few 10s of milliohms. However, this is still within the range needed for the ER measurements.

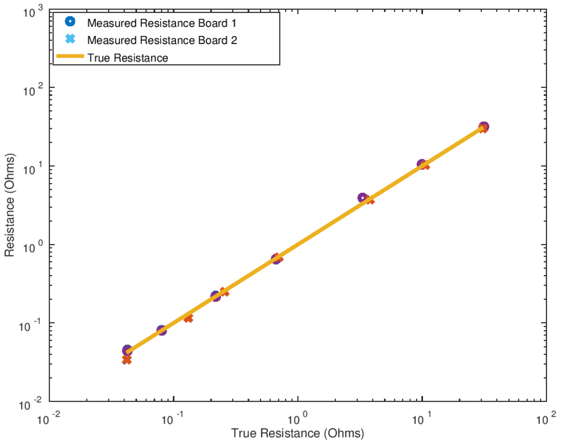

Figure 13: Resistance measurement sweep

(5) Thermocouple sweep

The thermocouple measurement mode was tested by placing two thermocouples on a hot plate and simultaneously reading one thermocouple with PIECES and the other thermocouple with a

Siglent SDM3055 multimeter. The results are shown in Figure 14. The measurements from PIECES track the slope of the true readings, but with up to a 10°C offset, which is caused by the cold-junction compensation process. The process for a thermocouple measurement is to read the voltage across the thermocouple junction, which indicates the temperature differential from the voltage-measurement location (i.e., cold junction) to the sensor location. To derive an absolute temperature value, this voltage measurement must be summed with a voltage that corresponds to the temperature at the cold junction. To achieve this "cold-junction compensation," PIECES is equipped with an MCP9808 temperature sensor. Unfortunately, this temperature sensor was placed beside the Raspberry Pi board which has a higher temperature than the actual cold-junction location, and thereby causes thermocouple readings that are higher than the true values. To mitigate this, we are using the temperature sensor in the ADS1292 which is further away from the Raspberry Pi. This sensor is giving readings that are closer to what the temperature should be at the location of the cold junction, but it is still a little warmer. Ideally, the temperature sensor should be placed directly at the cold junction. The readings shown in Figure 14 use the temperature sensor in the ADS1292. The temperature is calculated using Mosaic Industries' Type K thermocouple calibration equation [1]. The cold junction compensation was calculated using Mosaic Industries' cold junction compensation equation [2]. This method uses a rational polynomial function approximation using a least squares curve fit of the National Institute of Standards and Technology (NIST) type K thermocouple data.

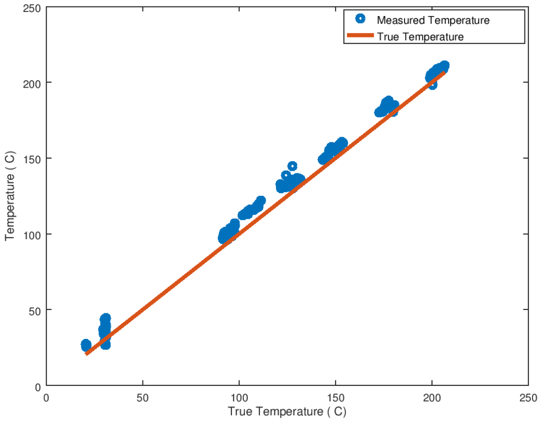

Figure 14: Thermocouple Measurement Sweep

(6) Power supply interference

Power supply interference was tested using two scenarios to verify that reliable readings can be obtained even when an unreliable power supply is used. In both scenarios, a 1Hz signal with 1V amplitude was placed on the measurement line. The sampling rate was 100Hz.

During the first scenario shown in Figure 15, a 0.24Hz signal with 0.4V amplitude and 5V offset was placed on the power line. While the 1Hz signal can clearly be seen, no interference can be observed at 0.24Hz.

During the second scenario shown in Figure 16, a 60Hz signal with 0.4V amplitude and 5V offset was placed on the power line. This test represents the typical expected scenario where power supply noise—either caused by AC mains or by radio activity in the device—is expected to be higher than the sampling frequency and would therefore show up in aliased form. Again, the 1Hz signal can clearly be seen while no interference can be observed at higher frequencies—note that the 60Hz interferer would have aliased down to 40Hz if it were large enough to observe.

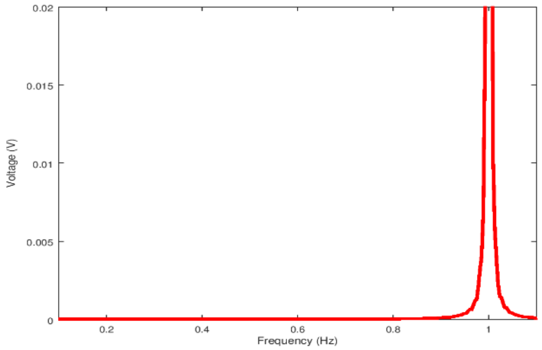

Figure 15: Power Supply 0.24Hz Interference with 1Hz signal

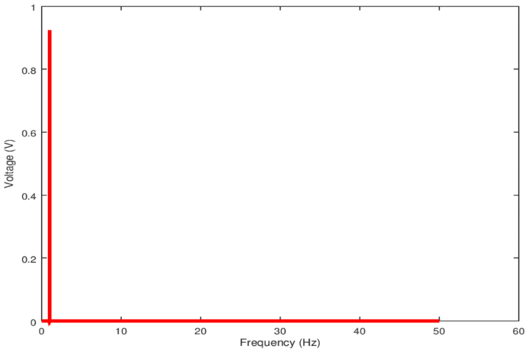

Figure 16: Power Supply 60Hz Interference with 1Hz Signal

(7) Channel to channel interference

Channel to channel interference was tested to verify that signals on different sensor lines do not interfere with each other. A 0.24Hz signal with 1V amplitude was applied to the RE line as interference.

In Figure 17, a 6Hz signal with 1V amplitude was applied to WE1 and was measured. This signal can be clearly observed, while no interference is seen at 0.24Hz.

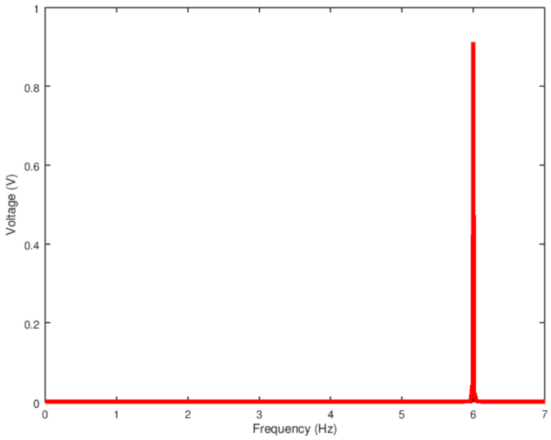

Figure 1: Channel to Channel 0.24Hz Interference with 6Hz Signal

(8) Intermodulation distortion

To verify the linearity of the PIECES measurement system, an intermodulation distortion test was performed by applying a summed 0.24Hz and 0.25Hz signal each at 0.5V amplitude for a combined 1V amplitude. PIECES was collecting at 100Hz sampling rate. The resulting spectra is shown in Figure 18. The only peaks are at 0.24Hz and 0.25Hz—no discernable distortion was observed in the form of additional peaks.

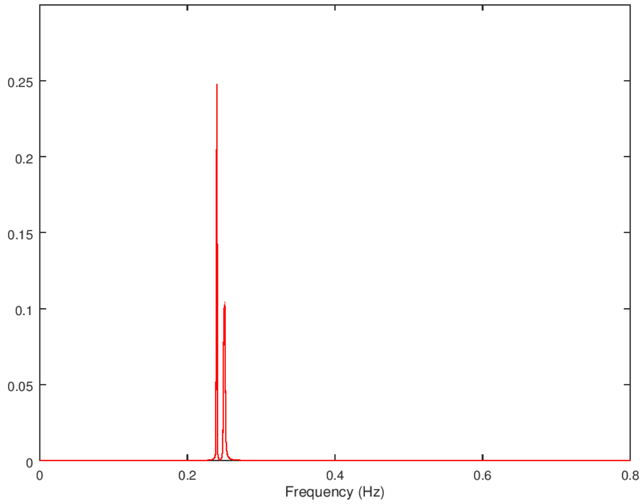

Figure 2: Intermodulation Distortion (0.24Hz and 0.25Hz each at 0.5V amplitude)

(9) Out of band interference/aliasing

To determine the susceptibility to out-of-band noise—such as noise that may couple onto the sensor cable—a test was performed measuring a summed 0.25Hz and 60Hz signal each at 0.5V amplitude for a combined 1V amplitude. PIECES was collecting at 100Hz rate. An aliased spike can be seen that wrapped from 60Hz to 40Hz—its amplitude is reduced by approximately half.

Aliasing can be further reduced by lowering the cutoff frequency of the on-board anti-aliasing filters or by adjusting the scheduling of measurement readings in the firmware. However, it is unknown at this stage what magnitude and frequency of cable noise to expect in the power plant environment. Reducing aliasing noise will be a topic for the next Phase of the after on-site measurements provide guidance on noise levels.

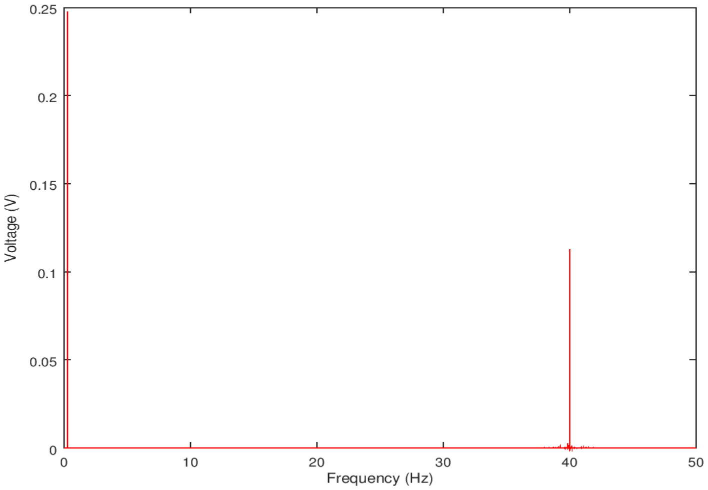

Figure 19: Out of Band Interference/Aliasing (0.25Hz and 60Hz each at 0.5V amplitude)

Task 3 Developing signal processing and communication instruments

(1) Introduction

To realize the wireless control of the data acquisition system, networking capabilities have been added to PIECES to enable remote data collection. Many options exist for networking sensors—both between sensor and gateway and between sensor/gateway and the wider internet. Figure 20 shows the envisioned architecture that we are building, and which represents a typical industrial IoT system. The **Sensor** converts the corrosion characteristics into electrical quantities (i.e., voltage, current, resistance) that are measured by the **Measurement Board**. Measurements are configured and scheduled by the **Measurement Controller** (via common inter-integrated circuit protocols SPI and I2C), which also temporarily stores the data. The **Gateway** aggregates data from multiple sensor nodes over time. We envision a Bluetooth Low Energy (BLE) interface between the controllers and gateway due to its increasing use in industrial systems. The **Gateway** sends the data to the internet via a cellular IoT **Network** (LTE Cat-M1) where the data is routed as HTTPS packets to a server for **Storage & Visualization**. We used our own server for the last stage but envision porting to a cloud provider for enhanced reliability.

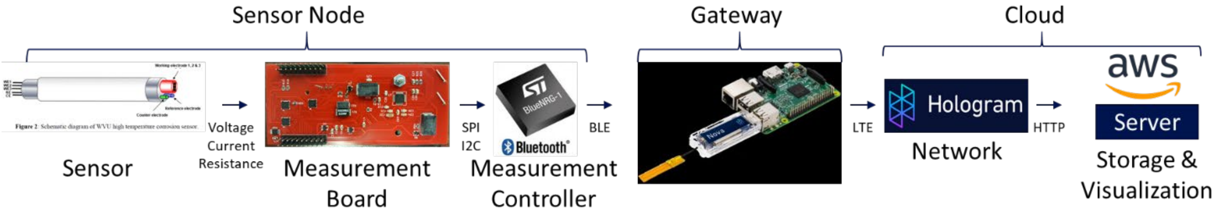

Figure 20: Envisioned data pipeline for the corrosion sensor

The pieces of Figure 20 are being built up over the various Phases of this project. The Sensor Node portion was built in Phases 1-3 using a Raspberry Pi as the Measurement Controller. The Gateway and Cloud portions have been built in Phase 4, with more focus on the Gateway and Network pieces. In the remaining phases, the Measurement Controller can be ported from a Raspberry Pi to a BLE System-on-Chip (SoC) to enable a battery-operated Sensor Node and the Storage & Visualization can be expanded upon. This progression is illustrated in Figure 21.

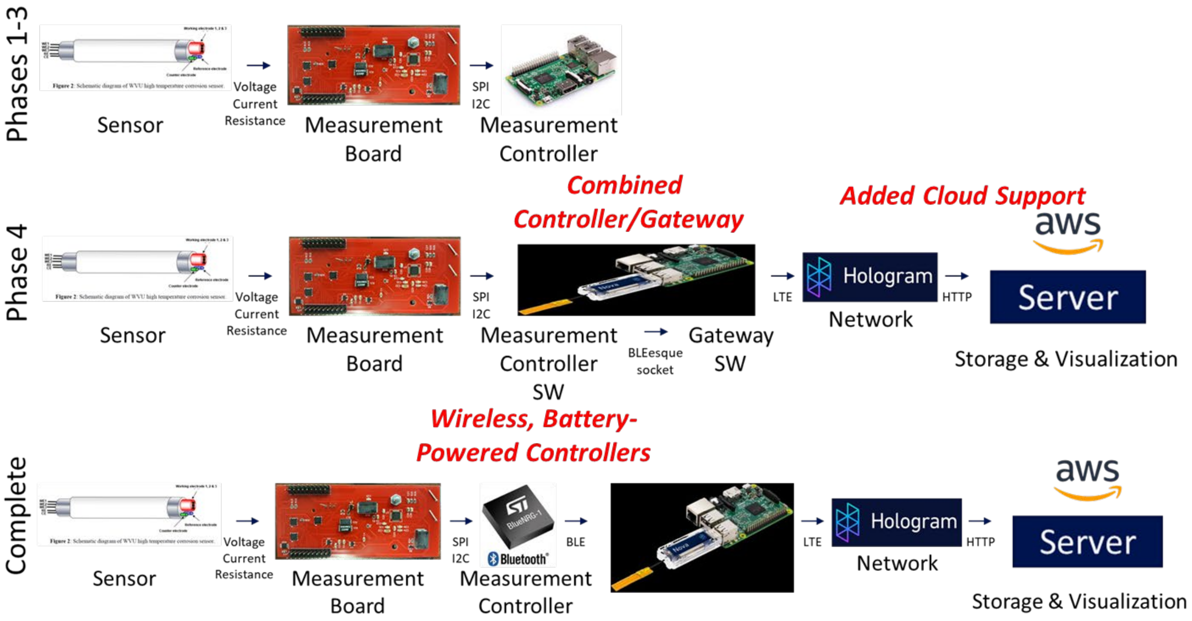

Figure 21: Progression from the Sensor Node built in Phases 1-3 to the complete data-collection stack envisioned for this project. In Phase 4, we have built a fully working stack. The shortcomings are that the Measurement Controller and Gateway are combined on one Raspberry Pi—so it does not allow battery operation nor multiple sensors networked via a single Gateway—and the Storage and Visualization capabilities are minimal. These can be expanded in the next Phases.

(2) Implementation

The cellular IoT implementation for the Phase centered around the communication architecture. The constraints and decisions for the architecture are illustrated in Figure 22. Even though the Measurement Controller software and Gateway software are both running on the same device in this implementation, we were careful to split their interfaces in preparation for an architecture where multiple sensors are networked to the gateway. This set the requirement that the interface between Measurement Controller and Gateway be architected to support an eventual BLE implementation. In this implementation a TCP socket on the Raspberry Pi models the BLE interface. To connect to the internet, IoT sensors typically use lightweight protocols because of limited resources on the devices and low data requirements. Our requirements for the Gateway-to-Cloud interface were driven by the choice of cellular network provider (i.e., Hologram.io, more in Section 3.2), but our use of JSON formatting will work well with other services.

The communication architecture allows data packets to be continuously sent from the PIECES device to the cloud. Additionally, it allows communication from the cloud to the PIECES device so that measurement settings can be adjusted, settings can be queried, and the device can also be rebooted remotely if necessary. Furthermore, alarm thresholds can be set so that the PIECES devices send a notification email when readings are out of range and may need to be checked on.

The remainder of this Section describes the implementation details of each component, including the Measurement Controller, Gateway, and Watchdog software on the PIECES hardware, the Hologram cellular IoT network, and the server.

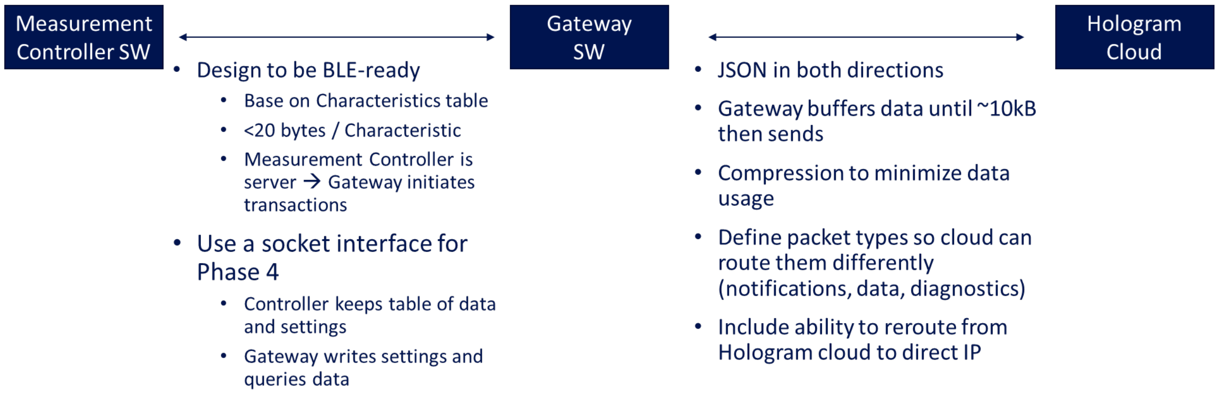

- Design to be BLE-ready
  - Base on Characteristics table
  - <20 bytes / Characteristic
  - Measurement Controller is server → Gateway initiates transactions
- Use a socket interface for Phase 4
  - Controller keeps table of data and settings
  - Gateway writes settings and queries data

- JSON in both directions
- Gateway buffers data until ~10kB then sends
- Compression to minimize data usage
- Define packet types so cloud can route them differently (notifications, data, diagnostics)
- Include ability to reroute from Hologram cloud to direct IP

Figure 22: Constraints for the interfaces of the cellular IoT communication architecture.

PIECES Device

① Measurement controller software

The Measurement Controller software is the interface between the measurement hardware and the rest of the stack. For this implementation it runs on the Raspberry Pi and is written in

C++. It includes the low-level firmware that interacts with the switch/ADC/etc. registers on the Measurement Board. It also includes a TCP socket interface so the Gateway software can communicate with it for everything needed to control and receive information from PIECES.

Measurement data is sent from the Measurement Controller over the socket in packets when a parameterized data limit is reached. PIECES measurement control variables can also be set and queried via the socket. Every time that a command is sent from the Gateway to the Measurement Controller, it will echo the command along with the response. This “command/response with regular measurement data packets” setup is similar to how a Bluetooth client/server system would work and should therefore be easy to move towards a wireless solution.

All commands sent from the Gateway to the Measurement Controller start with either *set* for setting a variable or *get* for querying a variable. After *set* or *get*, is the variable name. If the client is setting a variable, there should be a number after the variable name which will be the new value for that variable.

Example: *set cCnt_En 1*

Each variable name is made up of 2 parts separated by underscores. The 2 parts are referred to as prefix and suffix. The variable names can be split into 3 categories:

1. Variables that affect the general controller operation: *cCnt* (described in Table 2),
2. Variables that affect the ADC: *cAdc* (described in Table 3),
3. Variables that affect the individual measurement types (measurement prefixes described in Table 4 and variable suffixes described in Table 5).

Table 4: General Controller Variables

Variable	**Function**	**Accepted Input**
cCnt_En	Enable PIECES to take measurements.	0 | 1
cCnt_Trg	Trigger a one-shot measurement of all enabled measurement modes and immediately transmit.	0 | 1
cCnt_PktSz	Number of bytes in data packets. (Smaller values mean more frequent updates)	Positive integers
cCnt_DbgEn	Enable debugging messages.	0 | 1

Table 5: ADC Variables

Variable	**Function**	**Accepted Input**
cAdc_Dr	Data rate of ADS1292 ADC.	125 | 250 | 500 | 1000 | 2000 | 4000 | 8000

cAdc_C1Gain	Gain for measure channel 1.	1 | 2 | 3 | 4 | 6 | 8 | 12
cAdc_C2Gain	Gain for measure channel 2.	1 | 2 | 3 | 4 | 6 | 8 | 12
cAdc_Off_En	Enable automatic offset correction.	0 | 1
cAdc_Off_Int	Interval (in seconds) for recalibrating offset correction.	Positive integers
cAdc_Off_Raw1	Offset correction for measure channel 1.	Real numbers
cAdc_Off_Raw1En	Enable data transmit of channel 1 offset corrections.	0 | 1
cAdc_Off_Raw2	Offset correction for measure channel 2.	Real numbers
cAdc_Off_Raw2En	Enable data transmit of channel 2 offset corrections.	0 | 1

Table 6: Measurement Type Prefixes

Prefix	Function
cTc	Thermocouple (°C)
cR1	Resistor 1 (Ω)
cR2	Resistor 2 (Ω)
cV1RE	Voltage (WE1 to RE) (V)
cV2RE	Voltage (WE2 to RE) (V)
cV3RE	Voltage (WE3 to RE) (V)
cV12	Voltage (WE1 to WE2) (V)
cI12	Current (WE1 to WE2) (A)
cV23	Voltage (WE2 to WE3) (A)
cI23	Current (WE2 to WE3) (A)
cV13	Voltage (WE1 to WE3) (A)
cI13	Current (WE1 to WE3) (A)
cT1	MCP9808 Temperature Sensor (°C)
cT2	ADS1292 Temperature Sensor (°C)

Table 7: Measurement Type Suffixes

Suffix	Function	Accepted Input
En	Enable this measurement type.	0 | 1
SwLUT	Switch conFigureuration for this measurement type.	24 bits
Freq	Sampling frequency for this measurement type.	Positive real numbers
AvgNum	Number of readings to average into a measurement.	Positive integers
AvgFreq	Frequency to take each reading.	Positive real numbers
tEn	Include time in data packets (time in seconds).	0 | 1
Raw1En	Include channel 1 raw voltage in packets (voltage).	0 | 1
Raw2En	Include channel 2 raw voltage in packets (voltage).	0 | 1
MeasEn	Include final measurement in packets (measure type).	0 | 1
ResEn	Include current-measurement resistance in packtes (Ω).	0 | 1

When the Measurement Controller collects enough data to reach the packet limit (i.e. *cCnt_PktSz* in Table 4), it sends the data to the Gateway over the socket. Each variable in the packet is formatted in groups of 5 bytes:

[id84, data0, data1, data2, data3, id129, data0, data1, data2, data3, …]

The first byte is an identifier for the variable that follows in the next 4 bytes. There are currently 224 identifiers used in this architecture including all of the variables in the tables above. These identifiers are listed in the file *varList.csv* in the source code directory. The Measurement Controller and Gateway both need to have the same copy of this list of identifiers so the measurement packets can be deciphered. The 4 bytes following the identifier are either an unsigned integer representation of the time (in milliseconds) or a floating-point representation of the measurement values. Floating-point provides enough precision because the ADS1292 is a 24-bit ADC and floating-point provides 24 significant bits.

The Gateway software is the interface between the local sensor network of PIECES devices and the cloud or the user. It runs on the Raspberry Pi and is written in Python. The Gateway receives data packets from the Measurement Controller over a TCP socket, filters the data required for the packet, encodes it, and sends it to the cloud at regular intervals based on defined settings. It also accepts packets from the cloud containing new settings or queries and arbitrates communication with the Measurement Controller. In addition to the cloud interface, the Gateway software also accepts commands from standard input—so it can be controlled directly by a user with a keyboard connected to the Raspberry Pi.

At startup, the Gateway accepts a **.csv* file with the names of all the variables that are measured or configureurable and a port number to connect with the Measurement Controller as its input. It connects with the Measurement Controller via a TCP socket and with the cloud via Hologram's Python API for the Nova cellular modem.

The gateway begins by reading an initial configureuration JSON file present in a local directory ("configure.json") that describes the measurement settings and other operation characteristics. It loads the parameters from that file into its own parameters as well as loads them to the Measurement Controller by sending them via the socket. Parameters starting with 'g' are only for the Gateway and parameters starting with 'c' are for the Measurement Controller. These initial loaded settings are also sent to the cloud at bootup with a "settings" tag so that the user can see the current settings with which the device is running.

Once the initial configureurations are set, the gateway starts to accept the measured data from the Measurement Controller, appends them to a dictionary data structure—using the variable list **.csv* file to obtain the keys for the dictionary—and unpacks the data to get the measurement values for those keys. When a certain packet size (i.e. gateway parameter *gPktSize*) is reached, the gateway concatenates all data into a JSON string based on the variable name (only those variables that are enabled for transmission; i.e have *"variablename_TX":1* in the configureuration settings), encodes it, compresses it, and transmits to the cloud via Hologram. The full packet structure is shown below.

{"measdata":{"cI12_Meas":"MTE…","cI12_t":"MS4…",…},"metadata":…,"pktId":891}

The measdata field contains a field for each measurement variable (e.g. cI12_Meas) with the array of measurements encoded as described below. The metadata field is a placeholder for adding other information, and the pktId field provides a unique number for the packet to ensure they are sorted in order.

The encoding for transmitting the measurement data consists of these steps:

1. **Normalize and round to integers:** Each measurement value is divided by the *g*_scaleMeas* variable and then rounded to an integer. The scaling is chosen to avoid loss of precision. This normalizes the data—since the time, voltage, current, resistance, and temperature all have different units—to prepare for encoding. The scale factor is added as the first variable in the array that will be encoded.
2. **Delta encoding:** The differences between subsequent measurements are taken to reduce the range of values that must be encoded. The starting value is appended to the array that will be encoded, followed by each of the deltas.
3. **Base64 encoding:** The resulting array is converted to a string and then Base64 encoding is applied to compress the string. Base64 meets the requirements that the data must be encodable as an HTTP packet for the cloud communication.

In addition to transmitting data to the cloud, the Gateway also actively listens to data received from the cloud and from standard keyboard input simultaneously while sending the data to perform certain specific operations.

Commands from the server:

- reboot - This reboots the pi and restarts the entire setup.
- Data in json format - eg: {“cCnt_En”:0,”cCnt_Trg”:1}
  - Once the gateway receives data messages in this format, it automatically updates the ‘configure. Son’ file to these values and sends these Configurations to the controller to set the variables.
- Queries - eg: {“cCnt_En”:”?”}
  - This is used to query the controller for the value of a specific variable. Once the gateway receives the response to the query from the controller, it sends the results to the cloud using a “query” tag where the value for the variable can be seen.
- Saving Configurations - eg: {“gConfSave”:1}
  - Every time the present variable (gateway or controller variables) Configurations are to be saved, the cloud must send the command above (either in isolation or

with other commands). This will save the current Configurations in 'curr_configure.json' (essentially merging the original 'curr_configure.json' which was the last saved configureuration with the new configureurations sent as a message to the gateway, currently reflected in 'configure.json'). When the program restarts or reboots, the gateway runs with these new settings that are present in 'curr_configure.json'.

Commands from standard input:

- get cCnt_En - From the keyboard, if we send 'get' with a variable name, it acts as a query and the controller sends back the value of the variable to the gateway.
- set cCnt_En 1 - Writing this on the gateway would set the particular variable with the given value in the controller.
- exit - This is used to quit the program. The gateway and the measurement side exit on receiving this command.

In addition to the communications described above, the Gateway also sends notifications based on different events. When the device starts and the Gateway runs, it sends a 'Powering on' email to indicate everytime the program starts (or reboots). An email is also sent when the measurement values fall outside of a set range. The message indicates the variable, the value it is at currently, as well as the required range for that value.

If the modem connection goes away while the program is running, the data packets are buffered up locally and are sent once the connection returns.

In order to recover from brownouts, PIECES starts automatically using the last configureuration that it was given. This is done using the UNIX profile file. In the case of a software crash that does not cause the unit to reboot, a software watchdog will close both the Measurement Controller process and the Gateway process and restart them both using a new port number. Whenever the Gateway process starts, an email notification will be sent to let the user know that PIECES is starting. This way, the user may know if the unit had to restart. In the case that this occurs, all the data currently being recorded will be saved to a directory called *DUMPED FILES*. This directory can be retrieved by following the USB Data Transfer instructions. It cannot be retrieved through the cloud interface.

Hologram Cellular IoT Network

Given the deployment constraints for this device and guidance from the WVU team, it was determined that communication should happen over a cellular network. A developer faces a number of choices when connecting a sensor device to a cellular network. 2G/3G are common for IoT setups, but they are sunsetting, so we preferred LTE. The remaining choices are the modem hardware, the network provider, the cloud platform (which handles the interface between the internet and the cellular network), and the cloud backend. We settled on Hologram.io as they provide the modem hardware, the network, and the cloud platform combined. Additionally, they have a simple pricing model with world-wide cellular coverage agreements. They also have good documentation.

Figure 23: Hologram Nova cellular modem plugged into a Raspberry Pi.

We considered a variety of modems (Table 8) that are geared toward small projects before settling on the Hologram Nova modem (Figure 23). The modems are all based around similar chipsets, but the Nova modem had the advantage that it can connect directly via USB to the Raspberry Pi that is already part of PIECES, so no hardware rework was required. Additionally, it already has an API that runs on the Raspberry Pi.

Table 8: Summary of Cellular IoT Modem Modules

Module	Mfg	Modem	Price	Interface	Processor	SIM Card
MKR 1400	Arduino	U-Blox SARA	$69	Arduino IDE	SAMD21	Not included
FONA	Adafruit	SIM5320A	$79.95	UART	n/a	Ting
Electron	Particle	U-Blox SARA	$69	Particle Dev	STM32F2	Particle
Nova	Hologram	U-Blox SARA	$64	USB	n/a	Hologram

SIM cards and data plans for IoT devices are widely available, including from most electronics suppliers (e.g. Digikey, Adafruit, etc.). We chose Hologram for the reasons described above. The following link can be referenced to activate SIM cards from Hologram:

https://support.hologram.io/hc/en-us/articles/360035697873-How-do-I-activate-SIMs-

To achieve reliable operation, we had to update the modem’s firmware, the link below is referenced:

https://support.hologram.io/hc/en-us/articles/360035212594-Updating-the-Cat-M1-R410-Nova-s-Firmware[1]

To install the Hologram API on the Raspberry Pi, the first two commands from the following link are used:

https://hologram.io/docs/reference/cloud/python-sdk/

In order to use the Hologram API with Python3, line 336 in CustomCloud.py must be changed from *recv += result* to *recv += result.decode()*. This may require changing the file's access permission.

Hologram's platform provides several ways to communicate with a device:

- To device
    - Hologram cloud (acting as the interface between internet and cellular network)
        - Web dashboard: Interactive dashboard where one can enter JSON strings and send them to the device.
        - RESTful HTTP: Send HTTP commands from any program. The example below uses the UNIX curl command to say hello to the device. We have created several Matlab functions to automate communication with the device for sending new measurement settings and for accessing one-shot measurements.

```
curl POST --header "Content-Type: application/json" \

    --header "Authorization: Basic XXXXXXX"

    --data '{"deviceid": XXXXX, "body": "Hello device!"}’ \

     'https://dashboard.hologram.io/api/1/sms/incoming'
```

        - SMS: The device can receive SMS messages from the Hologram cloud without having a registered phone number.
    - Spacebridge tunnel: Direct SSH tunnel. Uses more data and requires additional software setup.
    - SMS: With a registered phone number, the device can receive message via SMS. We have not enabled this.

---

[1] `pip` is replaced by `pip3` in subpoint 3 in subpoint 3; and `python` is replaced by `python3` in subpoint 4 in order to be compatible with the installed versions.

- From device
    - Hologram cloud
        - Receive packets with device key, tags, and JSON-formatted data. A router in the web dashboard allows packets to be reformatted and sent to various services based on their content. We are using this to send notifications to emails and to send everything else to our server via a custom webhook (Figure 24).
    - Direct IP socket.
    - Carrier SMS (requires additional data plan).

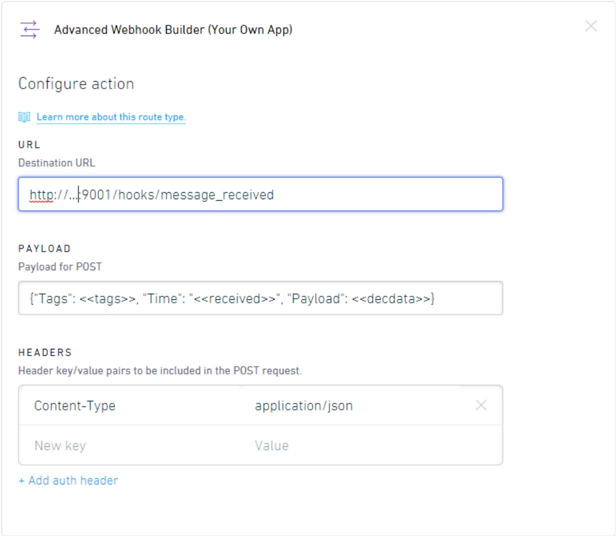
Advanced Webhook Builder (Your Own App)

Configure action

URL
Destination URL
http://...:9001/hooks/message_received

PAYLOAD
Payload for POST
{"Tags": <<tags>>, "Time": "<<received>>", "Payload": <<decdata>>}

HEADERS
Header key/value pairs to be included in the POST request.

Content-Type	application/json
New key	Value

Figure 24: Packet router settings for webhook to our server.

Server

When data packets are sent from the PIECES device, they are routed from the Hologram Cloud to our server via a webhook. The server is running Ubuntu with a webhook server installed from:

https://github.com/adnanh/webhook

Each time the webhook is triggered, it forwards the received packet to a script which does the following:

- Append the entire packet into a “raw” file.
- Extract the header info and append it into a “log” file.
- Parse the measured data into *.csv files.

The server also periodically reads in the stored data and generates plots. Access to the data on the server is described in Section 5.

We have verified the full communication stack by functionally testing one-shot measurements for each of the 14 measurement types (Voltage: W1-RE, W2-RE, W3-RE, W1-W2, W2-W3, W1-W3; Current: W1-W2, W2-W3, W1-W3; Resistance: R1, R2; Temperature: Thermocouple, ADS1292 temp-sensor, MCP9808 temp-sensor). We also let the unit sit and collect data for an extended time to verify reliability and verify the noise measurements.

Organization of the data on the server

The directory structure and file-naming conventions for the stored data on the server are as follows:

- Data
    - incoming
        - 2020_01
            - 01.log: log file for the first day of the month. Only contains header info. Used for reference.
            - 01.raw: full raw data file for the first day of the month. Contains all the packets in the form they arrived. Used for backups.
            - 01_id472440_cl12_Meas.csv: CSV file for the first day of the month from device 472440 containing the measured data for W1-W2 currents.
            - …
        - 2020_02
        - … (${YEAR}_${MONTH})
    - plots
        - 472440: PNG files of automatically generated plots for each measurement for device 472440.
        - …

To provide remote access, these files are stored in a directory that uses the Tonido syncing service as described in the next section.

Accessing the data via the Tonido syncing service

To access data from the server, we are using the Tonido syncing service, which is similar to Dropbox and other syncing services. This provides three options to access the data:

1. Web interface at cicada.tonidoid.com. (We will provide the login details separately.) After logging in, you can navigate through the file structure and download the data files. The interface is shown in Figure 25.

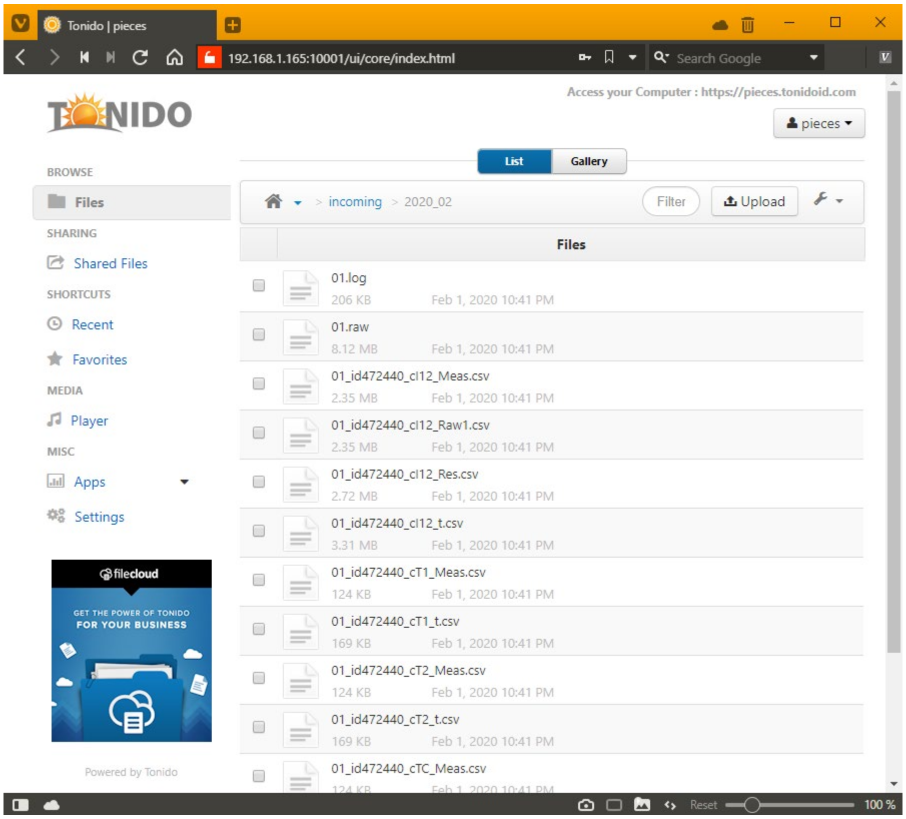

Files		
01.log	206 KB	Feb 1, 2020 10:41 PM
01.raw	8.12 MB	Feb 1, 2020 10:41 PM
01_id472440_cl12_Meas.csv	2.35 MB	Feb 1, 2020 10:41 PM
01_id472440_cl12_Raw1.csv	2.35 MB	Feb 1, 2020 10:41 PM
01_id472440_cl12_Res.csv	2.72 MB	Feb 1, 2020 10:41 PM
01_id472440_cl12_t.csv	3.31 MB	Feb 1, 2020 10:41 PM
01_id472440_cT1_Meas.csv	124 KB	Feb 1, 2020 10:41 PM
01_id472440_cT1_t.csv	169 KB	Feb 1, 2020 10:41 PM
01_id472440_cT2_Meas.csv	124 KB	Feb 1, 2020 10:41 PM
01_id472440_cT2_t.csv	169 KB	Feb 1, 2020 10:41 PM
01_id472440_cTC_Meas.csv	124 KB	Feb 1, 2020 10:41 PM

Figure 25: Web interface for accessing the data at cicada.tonidoid.com.

2. Install the Tonido sync client for Windows: http://patch.codelathe.com/tonido/live/installer/x86-win32/TonidoSync2Setup.exe. Versions are also available for Linux and Mac. We have found it is best to use the manual syncing option. Once it is installed, you will have a Tonido client running in your apps tray as shown in Figure 26. You can click on this to trigger manual syncing and to access the sync folder.
3. Tonido also provides mobile apps. These can be useful for quickly viewing the automatically generated plots.

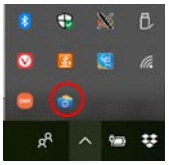

Figure 26: Tonido sync client running in the apps tray.

USB data transfer from the PIECES device

Data transfer using a USB Flash drive works similarly to how it was performed previously. The only difference now is that the Flash drive cannot be used to upload a new configureuration file to the unit. The only way to program PIECES is now through the cellular interface. When you transfer the data over USB, you will receive all of the data that the device has stored (up to a week) as well as any data the device saved after a crash.

To transfer data using a USB Flash drive, insert the Flash drive into one of the three empty ports. Do **not** unplug the modem to perform this process. Wait at least 5 seconds for the drive to connect. Some Flash drives will have an LED indicator that will change patterns to let you know that it is connected to the device. It is recommended to use one of these Flash drives so you have an indicator of when it is connected. Once the device has detected the Flash drive and has connected, press the black button once. It is not necessary to hold it down. Make sure to **not** hold it down for more than 10 seconds. If you do, the device will transfer its local date and time to the RTC. (This is useful for setting up new RTC devices.) After pressing the black button, the yellow light will flash and then stay on while the data is transferring. The transfer process may take up to a minute for each day's worth of data on the device. When the yellow light turns off, it is safe to unplug the Flash drive.

Task 4 Corrosion sensor testing @ Longview Power Plant

Task 4.1 Sensor placement and installation

Figure 27 depicts the installation of electrochemical sensor system through the observation port near the superheater located on the 11th floor of the boiler in Longview Power Plant. The exposure temperature was designed to be 550 ^{o}C, consistent with the actual exposed temperature of superheater in this power plant. The temperature is automatically adjusted by the temperature controller system through the feed of compressed air. The actual temperature is kept at 550 +/- 5 ^{o}C during the measurement. The signals including potential noise, current noise, actual temperature, resistance, are collected by the developed data acquisition system with a frequency of 1 Hz.

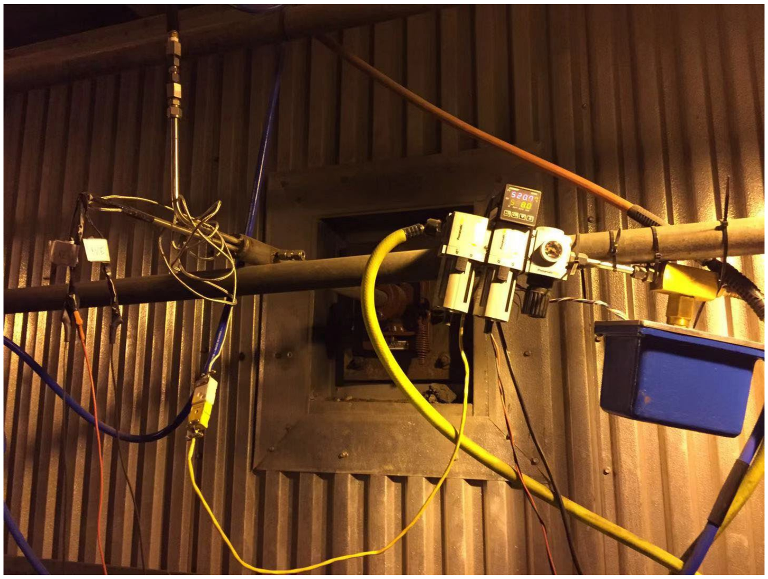

Figure. 27 the installation of electrochemical sensor system through the observation port near superheater (11 floor of the boiler)

Task 4.2 Sensor testing

Once the electrochemical sensor has been installed for one day, the initial potentiodynamic polarization curve was measured, as shown in Figure 28. The successful conduction of PDP suggests the formation of intact molten salt layer on the working electrodes acted as the electrolyte conducting ions. Tafel fitting was carried out to obtain the related parameters listed in Table 9.

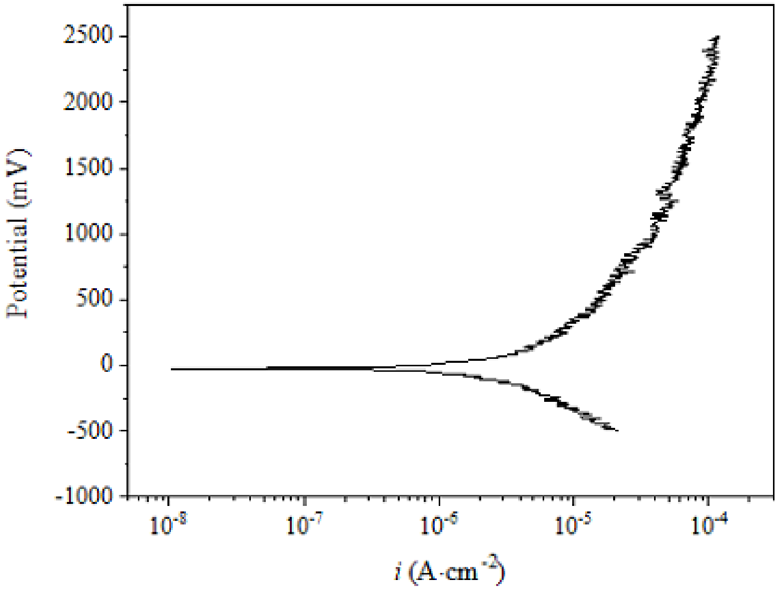

Figure 28: the potentiodynamic polarization (PDP) curve of 347H stainless steel measured at superheater place (550 °C)

Table 9: related parameter obtained from the PDP curve

Materials and location	Anodic Tafel slope, α (mV/decade)	Cathodic Tafel slope, β (mV/decade)	Stern-Geary coefficient, B (mV)
347 SS, Superheater	810.08±159.98	200.49±17.72	69.78

After the PDP test, the electrochemical noise and potential are recorded by the data acquisition system. We run several times in-field testing in the Longview Power Plant and encountered several big issues such as the installation of sensor, the location of the sensor, the effectiveness of the temperature controlling system and the reliability of the sensor and data acquisition system. After addressing several significant issues during the in-field testing, the latest electrochemical sensor was made and installed in the power plant on Aug 30th, 2019. It showed extraordinary reliability in the power plant which lasted for seven months without any operational problems. Figure 29 depicts the raw electrochemical potential and current noise from Aug 30th, 2019, to Apr 3rd, 2020. It did not work for some reason and we could not enter the power plant to check and fix it due to the pandemic. However, this sensor worked for such as a long duration and all the EN data were successfully collected unless the boiler was down for regular maintenance.

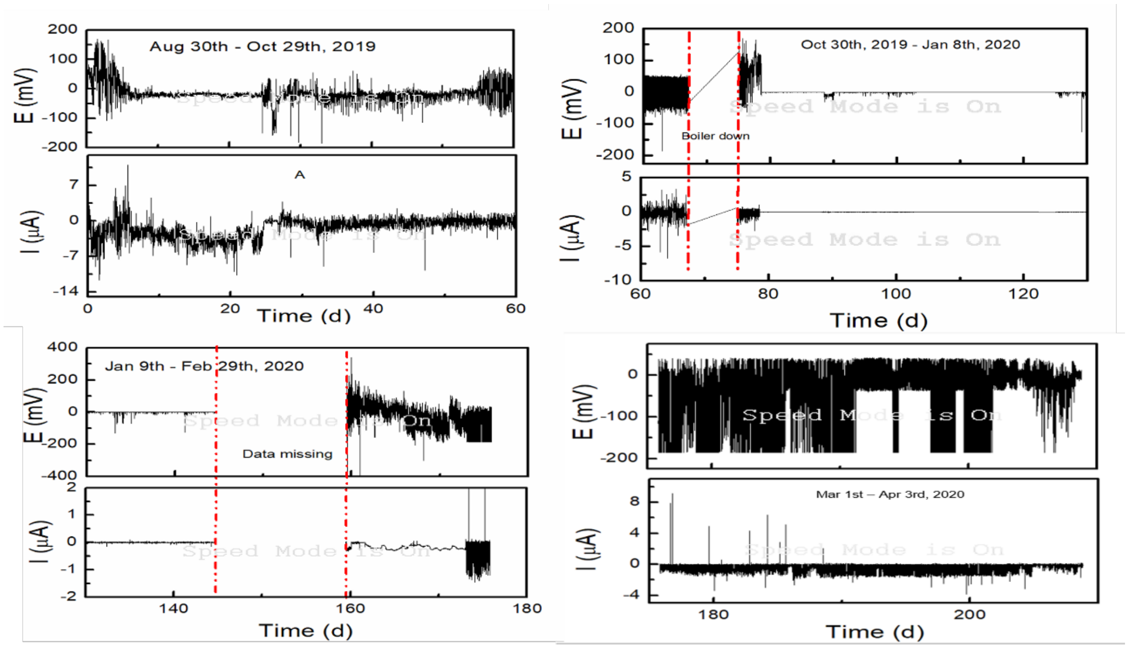

Figure 29: Electrochemical noise measured at the superheater since Aug 30th, 2019

Task 4.3 Post-mortem analysis

All the electrochemical data was collected and accessed through the self-developed remote data acquisition system. The data was real-time collected and transferred daily remotely. Once the electrochemical data is obtained. The following process depicted in Figure. 29 was adopted to calculate the corrosion depth by assuming all the iron atoms are oxidized to Fe^{3+}.

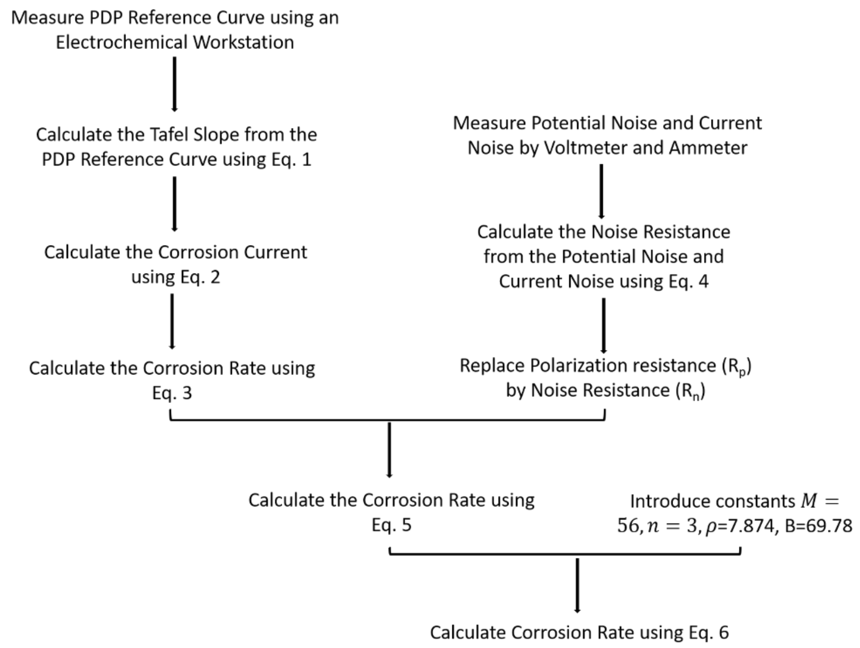

$$B = \frac{\alpha\beta}{\alpha+\beta} \quad (1)$$

$$J_{corr} = \frac{B}{R_p} \quad (2)$$

$$V_{corr} = \frac{3.27 \times B \times M}{n \times \rho \times R_p} \quad (3)$$

$$R_n = \frac{\sigma_v}{\sigma_i} \quad (4)$$

$$V_{corr} = \frac{3.27 \times B \times M}{n \times \rho \times R_n} \quad (5)$$

$$V_{corr} = \frac{540.9}{R_n} \quad (6)$$

Figure 30: Process to calculate the corrosion depth by electrochemical noise data

The corrosion depth calculated through the process depicted in Figure. 30 is shown in Figure. 31. When the boiler was down, no electrochemical signals were collected. Also, due to the equipment issue, some data is missed. Overall, the electrochemical sensor shows extraordinary stability for seven month.

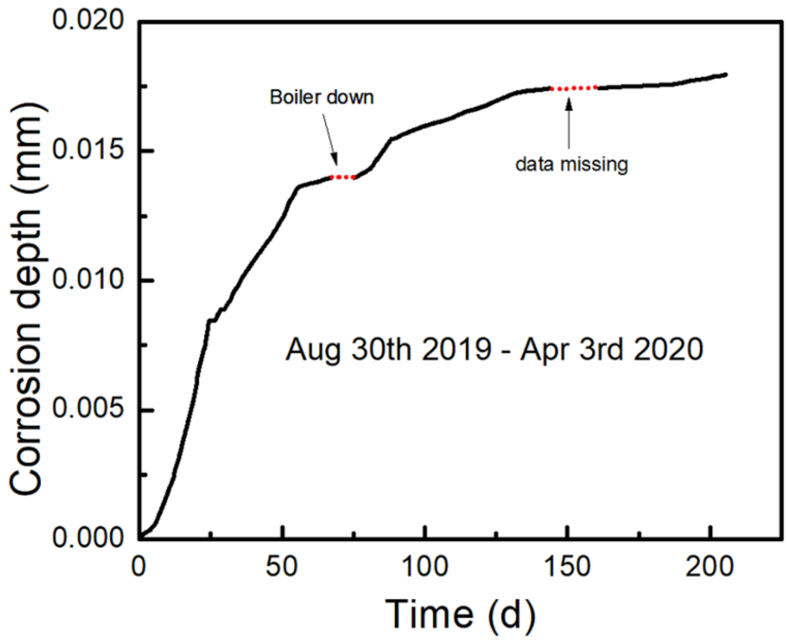

Figure 31: Time dependence of the accumulated corrosion depth calculated from the electrochemical noises measured at the superheater place.

Task 5 Corrosion monitoring software & database development

Besides the in-field testing of electrochemical sensor, lab-scale experimental were also conducted to develop corrosion database. To make the laboratory work close to the actual operation condition, firstly, we have to identify the composition of coal ash, a key factor influencing the corrosion process.

Two baskets of coal ash were obtained from Longview Power Plant. To determine the composition of coal ash, XRD and EDX were carried out to check the crystal structure and main elements in these coal ashes. As shown in Figure. 32 and Figure. 33, the coal ash in the basket labeled as 120 is amorphous while the one labeled as 122 is crystalline, suggesting the compositions of these two baskets of coal ash are different. EDX results show the main elements in the coal ash named as 120 are O, Si, Al, Ca, Fe and K while the other one mainly includes O, Si, Al and Ca. To obtain the detailed composition (mass ratio), two samples will be sent out to the composition analysis.

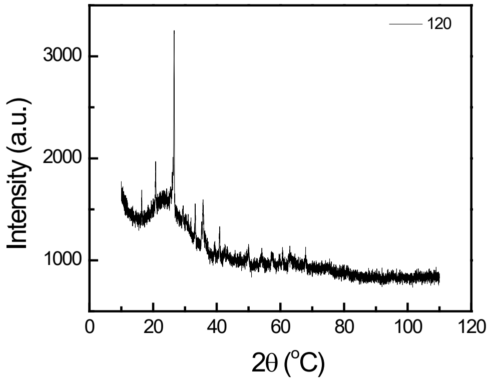

Figure. 32 XRD pattern of coal from Longview Power Plant (Labeled as 120)

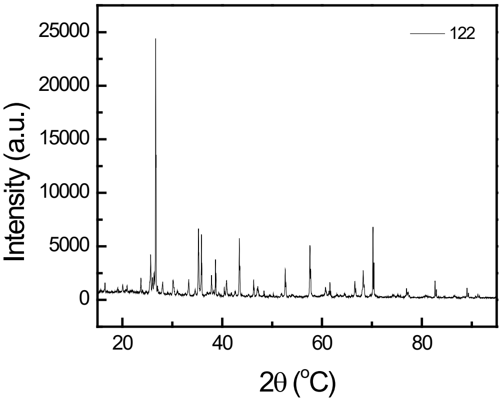

Figure.33 XRD pattern of coal from Longview Power Plant (Labeled as 122)

Besides XRD, chemical analysis has been conducted as shown in Table 10. It clearly shows the different compositions of the two batch of coal ash. To guarantee the repeatability of experimental results in lab, synthetic coal ash has been adopted.

Table 10 Various oxides in two kinds of coal ash from Longview Power Plant

	Al_2O_3	CaO	Fe_2O_3	MgO	MnO	P_2O_5	K_2O	SiO_2	Na_2O	SO_3	TiO_2
120	20.88	5.18	11.82	1.15	0.05	0.23	2.26	49.17	0.64	0.92	0.99
122	61.46	2.33	0.62	0.08	0.01	0.20	0.10	27.81	0.21	0.08	1.38

Task 5.1 Lab-scale sensor optimization

5.1 Reference electrode development

5.1.1 Experimental section

5.1.1.1 Preparation of Cu/Cu^{2+} reference electrode

The quartz sealed Cu/Cu^{2+} reference electrode was prepared by adding $CuCl_2$ (99.9%, Sigma-Aldrich, melting point, 498 °C) and NaCl (99.9%, Sigma-Aldrich, melting point, 801 °C) with a molar ratio of 1:9 into a quartz tube with one closed end (Advalue Technology Inc) by following the preparation process of the Ag/AgCl reference electrode [16]. The starting melting point of this mixture of $CuCl_2$ and NaCl measured by DTA is around 386.1 °C, lower than the lowest experimental temperature, i.e., 500 °C (Figure. 34). A copper wire with a diameter of 1 mm (99.99%, Surepure Chemetals Inc, melting point, 1085 °C) was immersed into the salt. The exposed Cu wire was spot-welded to a tungsten wire with a diameter of 0.4 mm (99.99%, Surepure Chemetals Inc). The outer diameter and thickness of this quartz tube was 8 mm and 1 mm, respectively. The residual air in the quartz tube was exhausted with the assistance of a vacuum pump while the open end was sealed with the aid of oxygen-methane flame. The schematic of the reference electrode is depicted in Figure. 34. To minimize the electric resistance of this reference electrode, the quartz tube was thinned manually by grinding using SiC abrasive paper. The final thickness of the quartz tube is about 0.4 mm. The potential difference between the quartz sealed Cu/Cu^{2+} reference electrode and the quartz tube sealed Ag/Ag_2SO_4 (molar ratio between Ag_2SO_4 and NaCl is 1:9) has been experimentally verified to be around 0.45 V at 600 °C, 650 °C and 700 °C shown in Figure. 34, demonstrating the half reaction in $Cu/CuCl_2$ reference electrode is $Cu + 2e \leftrightarrow Cu^{2+}$ (the standard potential of Ag/Ag+, Cu/Cu2+, Cu/Cu+ is 0.8 V, 0.36 V and 0.18 V, respectively).

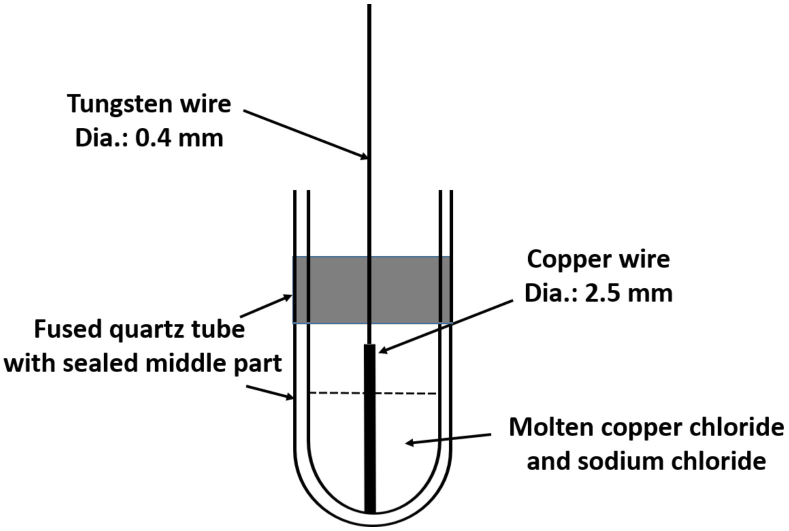

Figure. 34 The schematic of the quartz sealed Cu/Cu^{2+} reference electrode

5.1.1.2 Performance of Cu/Cu^{2+} reference electrode

The electrochemical measurements were conducted in an alumina crucible which was filled with synthetic coal ash with a composition of 40% SiO_2 (99.9%, Sigma-Aldrich), 40% Al_2O_3 (99.9%, Sigma-Aldrich), 9% Fe_2O_3 (99.9%, Sigma-Aldrich), 5% Na_2SO_4 (99.9%, Sigma-Aldrich), 5% K_2SO_4 (99.9%, Sigma-Aldrich) and 1% NaCl (99.9%, Sigma-Aldrich). Except otherwise specified, synthetic coal ash was used as the electrolyte in the following tests. Electrodes were connected to a Gamry 1010E interface. Synthesized flu gas with a composition of 1 vol. % SO_2, 4 vol. % O_2, 15 vol. % CO_2 and 80 vol. % N_2 was fed at a flow rate of 100 ml min^{-1} to simulate the working condition in a coal-fired power plant. The coal ash started to melt from 535 ^oC to form a molten salt layer with the feed of flu gas, as depicted in Figure. 34. All the electrodes were spotted welded to a tungsten wire with a diameter of 0.4 mm which was shielded in a ceramic tube to avoid oxidation. The experimental temperature varied from 500 ^oC to 900 ^oC.

With the quartz sealed Cu/Cu^{2+} reference electrode as the counter electrode, a piece of platinum with the dimension of 20 X 20 mm^2 or another quartz sealed Cu/Cu^{2+} reference electrode as the working electrode which was placed with a spacing of 1 cm. A small voltage, i.e., 20 mV, was applied to measure the response of current between two electrodes for a few milliseconds. By assuming that the equivalent circuit of this system is a resistor and a capacitor connected in series, the value of this resistor can be calculated by the voltage and instantaneous current using the Ohm's law. The resistance of this reference electrode is the difference between two values obtained with the platinum and the reference electrode used as the working electrode, respectively. Each reported value is the average of five measurements. In this experiment, the coal ash was replaced by molten salt composed of Na_2SO_4 and K_2SO_4 with a weight ratio of 1:1 to minimize the resistance of electrolyte.

The reproducibility of this reference electrode was checked by measuring the potential difference between two similar reference electrodes made at separate times. Every reference electrode was immersed into synthetic coal ash with the same depth, i.e., 1 cm, to ensure the same contact area.

The stability of the reference electrode was probed by measuring the potential difference between two similar reference electrodes as a function of time.

A micropolarization test was conducted to check the reversibility of this reference electrode by adopting the reference electrode as the working electrode and a piece of platinum as the counter electrode with a scan rate of 0.5 mV s^{-1} in a potential range between -5 mV and 5 mV versus OCP. The potential was designed to sweep from 0 mV to 5 mv, then from 5 mV to -5 mV, finally back to 0 mV vs. OCP.

Galvanostatic chronopotentiometry was adopted to reveal the cathodic and anodic polarization of this reference electrode. The open circuit potential between two similar reference electrodes was measured after a small current (1, 2 and 3 mA) passed through it with a duration of 300 s.

5.1.1.3 Application of Cu/Cu^{2+} reference electrode in electrochemical tests

All electrochemical tests including OCP, EN and PDP were conducted at 700 ^oC using our developed high temperature electrochemical sensor [20], which consisted of two identical working electrodes, i.e., a piece of TP347H stainless steel with a dimension of 10 × 10 × 3 mm^3, one counter electrode, i.e., a piece of platinum with a dimension of 20 × 20 × 0.5 mm^3 and one reference electrode, i.e., the quartz sealed Cu/Cu^{2+} reference electrode. Both working electrodes were sealed with the aid of ceramic paste leaving a surface of 10×10 mm^2 which were covered by 1 mm coal ash. All these electrodes were welded with tungsten wires which were placed into the alumina tube to avoid oxidation at elevated temperatures. The OCP of one TP347H electrode with respect to Cu/Cu^{2+} reference electrode was measured in the first hour using the platinum as the counter electrode. Then the EN test was executed with a prolonged time of 72 h with a frequency of 1 Hz by measuring the current noise of two TP347H electrodes in ZRA mode and the potential noise of one TP347H electrode with respect to Cu/Cu^{2+} reference electrode. The PDP test was performed at the end of the EN test with a scan rate of 0.5 mV s^{-1} from -2 V to 2 V versus OCP.

5.1.1.4 Weight loss measurement and characterization

The weight and surface area of four TP347H samples with a dimension of 10 × 10 × 5 mm^3 were recorded. Then all four samples were buried in the coal ash in an alumina crucible which was placed in the tube furnace with the feed of the same flu gas. After 72 h, the corrosion products on three samples were removed in boiling water for 20 min followed by ultrasonic cleaning in acetone, then rinsing with distilled water and drying in cold air. The final weights of three samples were measured with the aid of a microbalance with an accuracy of 1 × 10^{-6} g. The cross-section morphology of the corrosion product and corresponding elemental distribution mapping were characterized by SEM equipped with EDX.

5.1.2 Result and discussion

5.1.2.1 Electric resistance of ionic conduction of sodium through quartz tube

The ohmic resistance of the Cu/Cu^{2+} reference electrode in molten sodium sulfate is summarized in Table 11. We expect the uncertainties of the resistance values not to exceed +/- 50% due to the different conFigureuration between Cu/Cu^{2+} reference electrode and platinum and the delayed response of current. The data clearly reveal that the ohmic resistance decreases with increasing temperature. Figure. 35 reveals the good linear correlation between $\log_{10}$ (T/R) (denoted as log(T/R)) and 1000/T, with an R^2 of 0.9865.

Table 11 The electric resistance of Cu/Cu^{2+} reference electrode in molten sulfate salt at different temperatures

Temperature (°C)	500	550	600	650	700	750	800	850	900
Resistance (Ω)	6.7k	4.8k	4.0k	2.8k	2.2k	1.4k	1086	920	830

The ohmic resistance of this reference electrode is mainly ascribed to the diffusion of sodium ions through the quartz tube [9, 16]. The straight line in Figure.35 suggests the conduction of sodium ions through quartz tube is a thermally activated process, defined by Eq. (1).

$$\frac{T}{R} = \alpha \cdot exp\left(\frac{E_1}{kT}\right) \qquad (1)$$

Wherein, α is the pre-exponential factor; T is the experimental temperature, K; R is the ohmic resistance of the reference electrode, Ω; E_1 is the activation energy, J, and k is the Boltzmann constant (1.381 × 10^{-23} J/K). The slope of the fitting line in Figure. 2 is -2.061, yielding an activation energy of 0.52 eV (1 eV = 1.602 × 10^{-19} J). This value is much smaller than in the one reported in Gao et. al's work, i.e., 1.36 eV, due to the thinner wall of the quartz tube.

As shown in Table 11, it clearly reveals that the ohmic resistance of the reference electrode even at 500 °C, i.e., 6.7 kΩ is far lower than 10^{12} Ω, i.e., the resistance of the input impedance of the Gamry 1010E, demonstrating its applicability in a wide temperature range from 500 °C to 900 °C.

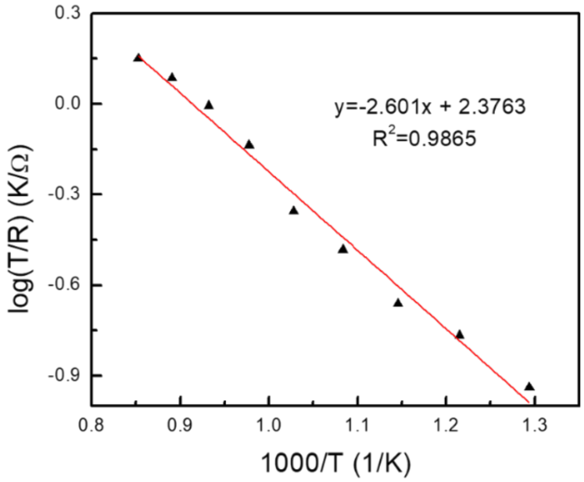

Figure. 35 the linear relationship between log (T/R) and 100/T of the reference electrode from the data in Table 11.

5.1.2.2 Reproducibility, stability, durability and reusability

The cell diagram of two similar quartz sealed Cu/Cu^{2+} reference electrodes immersed in the coal ash is denoted as

Cu(s)|$CuCl_2$(l)+ NaCl (l) ‖ quartz tube ‖ Na_2SO_4(l) + K_2SO_4(l) ‖ quartz tube ‖$CuCl_2$(l)+ NaCl (l)|Cu(s)

SiO_2 is stable in basic molten sulfate salt and the dissolution of SiO_2 in acidic fused sulfate salt is a chemical dissolution process without any charge transfer; the chemical dissolution does not affect the potential difference between two similar Cu/Cu^{2+} reference electrodes [24]. Designating the left reference electrode as the anode, the electrochemical reactions for these two reference electrodes are shown in the following equations.

Left side (anode): $Cu - 2e^- \rightarrow Cu^{2+}$ (2)

Electrolyte: $2Na^+$ (left) → $2Na^+$ (molten sulfate salt) → $2Na^+$ (right) (3)

Right side (cathode): $Cu^{2+} + 2e^- \rightarrow Cu$ (4)

Assuming that the sodium junction potentials resulting from the diffusion of Na^+ through the semi-permeable quartz tube and the molten sulfate salt having equal magnitude and opposite signs, the potential difference between two similar quartz sealed Cu/Cu^{2+} reference electrodes is zero theoretically. Ten similar Cu/Cu^{2+} reference electrodes made at separate times were placed in synthetic coal ash with the same immersed depth and the OCPs between any two similar Cu/Cu^{2+} reference electrodes were measured over the temperature range from 500 ^oC to 900 ^oC. The potential differences between these reference electrodes were less than 5 mV at most time and never greater than 8 mV regardless of the exposure temperature, demonstrating the desirable reproducibility of this reference electrode. The slight potential difference might be ascribed to the asymmetric construction of these two reference electrodes or the acceptable experimental error. This reproducibility is comparable to Ag-AgCl and Ag-$AgSO_4$ reference electrodes reported in the literature [9, 12, 16].

The potential difference between two similar Cu/Cu^{2+} reference electrodes at 600 °C and 800 °C monitored for 200 h is shown in Figure. 36. The potential difference is between – 5 mV and 5 mV at 600 °C and from – 8 mV and 8 mV at 800 °C in the duration of 200 h, demonstrating good stability of this type of reference electrode over eight days.

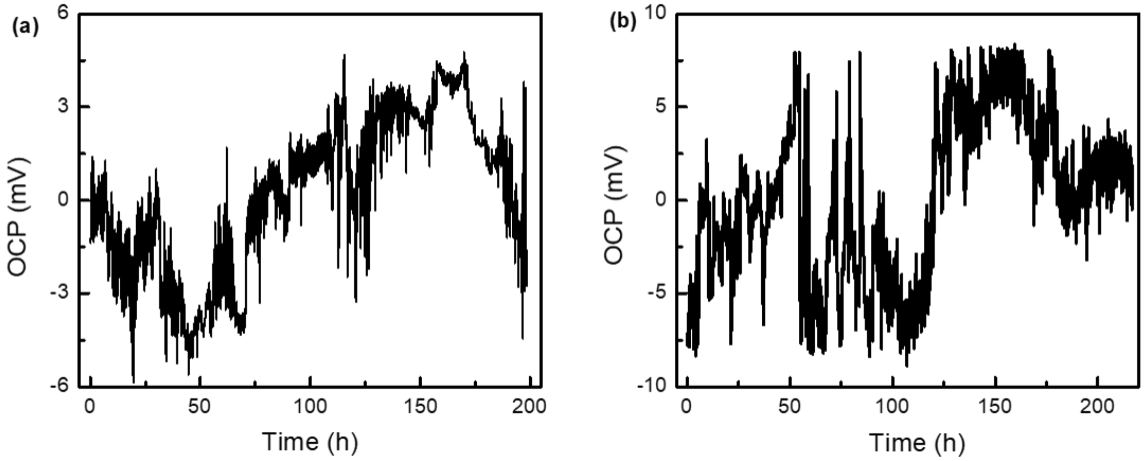

Figure. 36 Potential difference between two similar quartz sealed Cu/Cu^{2+} reference electrodes in synthetic coal ash as a function of time at (a) 500 °C and (b) 800 °C

It is important to note that these reference electrodes were immersed in the coal ash all the time during the measurement of potential difference between two similar reference electrodes at both 600 °C and 800 °C for 200 h shown in Figure. 36. The reference electrode has been successfully used in this corrosive environment for a continuous period of 400 h, about 16 days, demonstrating its outstanding durability in molten sulfate salts. Moreover, this reference electrode can be washed by water and stored once it is taken out from the coal ash for the following multiple-time usage without impairing its capability. However, after several usages, the surface of the quartz tube, especially the quartz tube/ molten salt/ flu gas triple phase boundary is eroded. The erosion site is brittle and prone to break. A similar result has been found in a previous report which is ascribed to the formation sodium silicates [16].

5.1.2.3 Polarization of reference electrode

Figure. 37 shows the potential difference between two similar Cu/Cu^{2+} reference electrodes in synthetic coal ash after the flow of a small current (1 mA and 2 mA at 500 °C, 1 mA, 2 mA and 3 mA at 600 °C, 700 °C, 800 °C and 900 °C) for 300 s. The chronopotentiometry measurement with a current of 3 mA at 500 °C cannot be performed due to the limited voltage range (-5 V to 5 V) of the electrochemical workstation. The initial value of potential difference (2 mV) is re-established within 120 s and 200 s after the flow of a small current of -/+ 1 mA and -/+ 2 mA, respectively at 500 °C (Figure. 5a). No visible difference was observed between cathodic and anodic polarization. The time required to resume the initial value is shortened to less than 40 s with the increase of temperature (Figure. 5b-e). These times reflect the recovery of the concentrations of Cu^{2+} concentration at the surface of the Cu wire after polarization. Overall, the Cu/Cu^{2+} reference electrode exhibits similar recovery behavior to Ag/AgCl reference electrode [10].

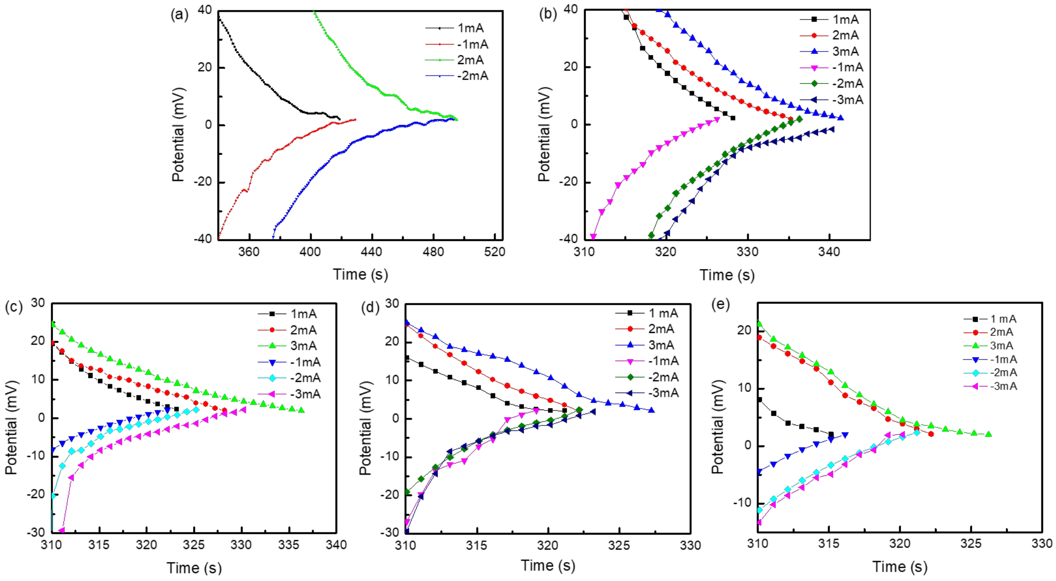

Figure.37 Chronopotentiometry of two similar Cu/Cu^{2+} reference electrodes at different temperatures (a) 500 °C, (b) 600 °C, (c) 700 °C, (d) 800 °C and (e) 900 °C after the flow of a small current for 300 s

5.1.2.4 Reversibility

Cyclic voltammetry curves with the Cu/Cu^{2+} electrode as the working electrode and platinum as the counter electrode at different temperatures are shown in Figure. 38. The OCP grows with the increase of temperature which might be attributed to response of the potential of the Cu/Cu^{2+} reference electrode to temperature. It clearly reveals a linear behavior in the potential range -/+ 5 mV versus OCP from 500 °C to 900 °C. The linear relationship between the current density and potential indicates the good reversibility of the Cu/Cu^{2+} reference electrode in coal ash from 500 °C to 900 °C.

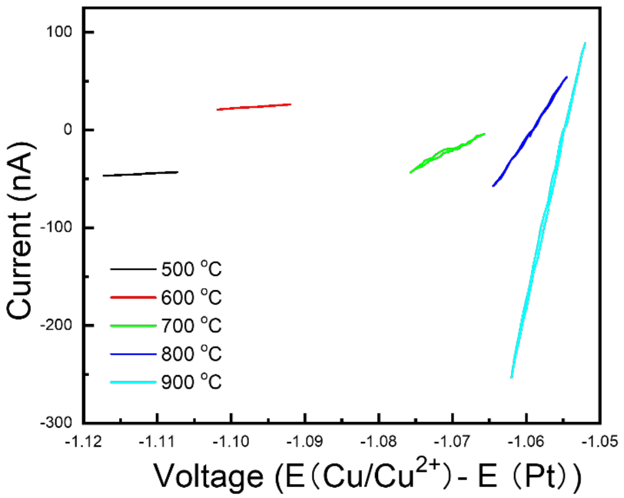

Figure. 38 The Micropolarization test of Cu/Cu^{2+} reference electrode at 500 °C, 600 °C, 700 °C, 800 °C and 900 °C

5.2.1.5 Application of this reference electrode to investigate the coal ash hot corrosion behavior of TP347H

Figure. 39 depicts the OCP as a function of time in the first hour. The OCP grows from 385 mV to 500 mV versus Cu/Cu^{2+} in the first hour. This might be ascribed to the formation of a protective scale composed of oxides of nickel, chromium and their spinels on the surface of TP347H, which is similar to the layer formed on the nickel-based alloy when exposed to the oxidizing atmosphere at elevated temperatures.

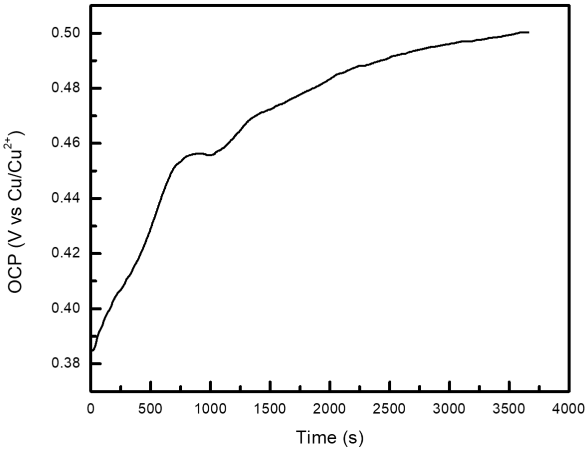

Figure.39 OCP as a function of time in the first hour at 700 °C

Figure. 39 depicts the (a) potential and (b) current of for two TP347H electrodes held at the same potential as a function of time for 72 h. In the initial corrosion stage, the potential grows from 500 mV to 1.02 V versus Cu/Cu^{2+} and the (absolute) current density decreases gradually from 14 µA to 500 nA. The decrease of potential is attributed to the growth of oxide scale during the corrosion process [29, 30]. The existence of a negative direct current drift suggests the preferential oxidation of one working electrode in the initial stage which might be ascribed to the accepted asymmetry between two electrodes. After several hours, the negative direct current drift was shifted to be positive, indicating the faster corrosion rate of the other working electrode due to the growth of the oxide scale on the previous working electrode during the initial corrosion process [6, 30]. The trend in the data was calculated using 8th-order polynomials with an R^2 of 0.998 for potential and 0.864 for current noise and subtracted to isolate the potential and current noise. The potential and current noise after detrending is depicted in Figure. 40 (c) and (d). The bidirectional transient of current noise indicates the corrosion of both working electrodes in the entire process. Finally, both the potential and current fluctuate randomly in a narrow range, around 1.02 V versus Cu/Cu^{2+} and 500 nA, respectively, which is the characteristic of the sulfidation process, as described in the literature [29, 30]. This experimental result verifies the feasibility of the application of electrochemical noise to monitor the corrosion process of TP347H in coal ash with the aid of this reference electrode. The cross-section morphology of TP347H after hot corrosion for 72 h and the corresponding element distribution (Figure. 41) further confirm the formation of oxides and sulfides which is consistent with the corrosion process characterized by the potential and current noise pattern in Figure. 40.

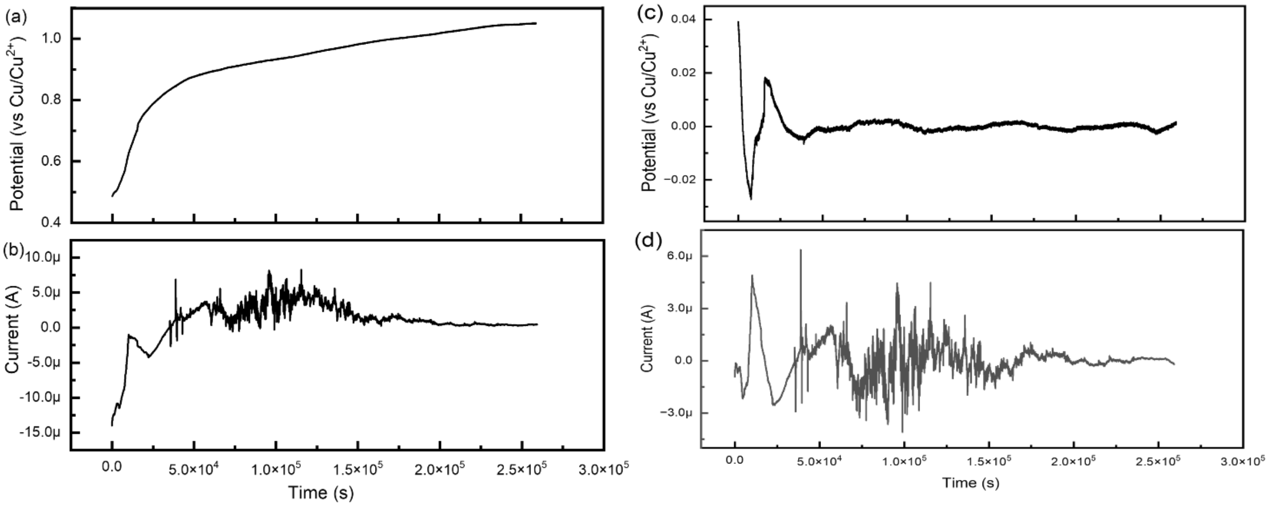

Figure.40 (a, c) Potential and current (a, b) before and (c, d) after detrending of TP347H as a function of time at 650 °C for 3d with 2 mm coal ash

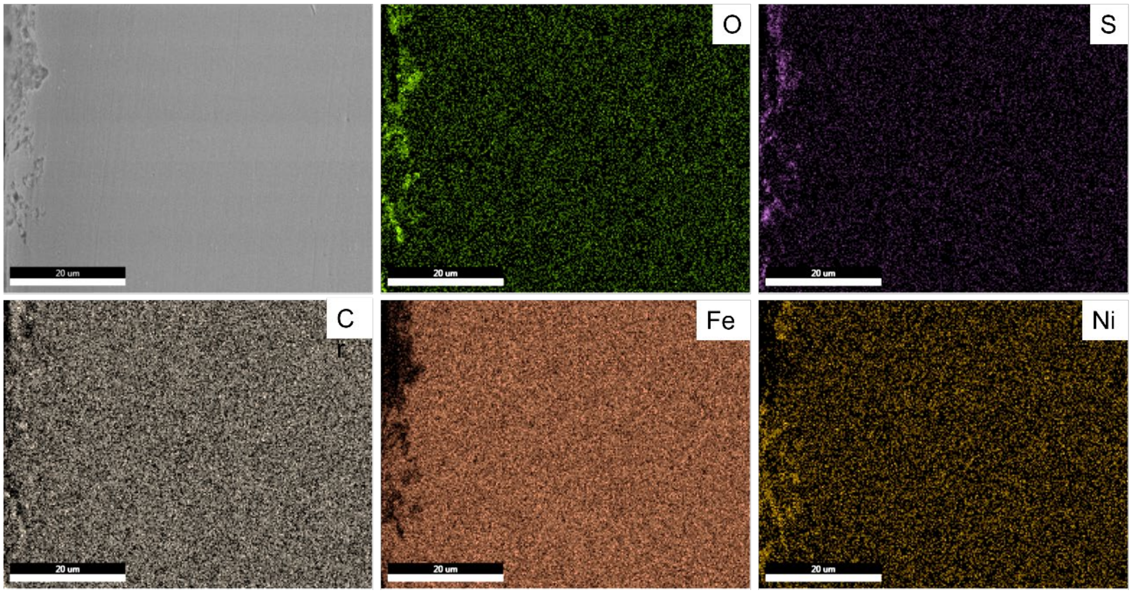

Figure.41 Cross-section morphology and corresponding element distribution mapping of TP347H after coal ash hot corrosion at 700 °C for 72 h

After detrending, the potential and current noise is transferred to frequency domain through Fast Fourier transformation (FFT). Noise resistance, the ratio of the standard deviation of the potential noise to the current noise, in the time domain (R_n) and frequency domain (R_{sn}) has been proved to be an effective indicator of the corrosion rate. The comparison of R_n and R_{sn} value is shown in Figure. 42a. It clearly reveals that R_n and R_{sn} show the same trend. Both R_n and R_{sn} show the highest value in the third day which might be attributed to the formation of oxidation scale during the initial corrosion process, hindering the ingress of oxidization species. The PDP curve ranging from -2 V to 2 V versus OCP after EN test has been successfully obtained with the aid of the Cu/Cu^{2+} reference electrode (Figure. 42b). The OCP is 1.0 V versus Cu/Cu^{2+} which is consistent with the potential noise in Figure. 40b. No signal fluctuation has been observed during the measurement.

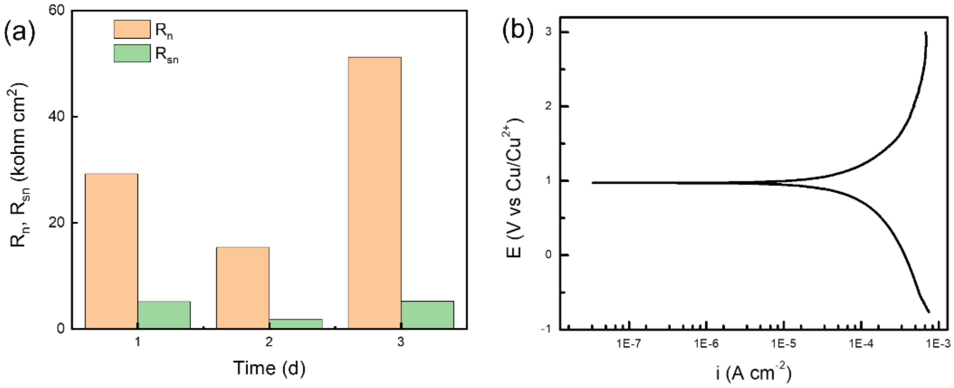

Figure. 42 (a) R_n and R_{sn} as a function of time and (b) PDP after hot corrosion at 700 °C

Compared with other electrochemical measurement such as PDP and EIS, electrochemical noise can be a powerful tool to measure the real-time corrosion rate without any instrumental disturbances. According to the Faraday's law, the corrosion rate (CR, g cm^{-2}) can be calculated through eq (5) [32].

$$CR = (M \times i)/\rho FnS \qquad (5)$$

Wherein i is the current density, A; F is a Faraday's constant, i.e., 96485 C mol^{-1}; ρ is the density of TP347H, i.e., around 7.84 g cm^{-3}; S is the exposed area of the working electrode, 1 cm^2; M represents the atomic mass of iron, i.e., 56 g mol^{-1}; n is for the number of electrons transferred per atom of iron, i.e., 3 by supposing all the iron atoms are oxidized to Fe^{3+}.

The accumulated corrosion rate calculated through eq (5) is 0.378 mg cm^{-2}, which is lower than that ^{2}calculated by weight loss measurement, i.e., 0.459 mg cm^{-2}. The difference might be attributed to the unavoidable oxidation during the ramp-up and down of tube furnace. With the aid of this robust reference electrode, electrochemical measurements have been successfully conducted to tentatively investigate the hot corrosion behavior of TP347H. Future work will focus on the coal ash hot corrosion mechanism through various electrochemical measurements.

5.1.3 Conclusion

A robust Cu/Cu^{2+} reference electrode with good stability, reproducibility, durability, reversibility and non-polarizability in the temperature range from 500 °C and 900 °C has been developed in this work. The ionic resistance associated with the diffusion of Na^+ ions through the quartz tube, which is a thermally activated process, decreases with the increase of time. Moreover, the ohmic resistance of this reference electrode is just 6.7 KΩ at 500 °C which is far lower than that of the input impedance in the Gamry 1010E Interface. With the aid of this reference electrode, electrochemistry tests including OCP, PDP and EN have been conducted to investigate the coal ash hot corrosion behavior of various alloys in commercial conditions.

5.2 Corrosion database development- effect of temperature

5.2.1 Experimental details

TP347H stainless steel, same material as the superheater in service in Longview Power Plant, was supplied by Longview Power, LLC, a coal-fired power plant located in State of West Virginia, USA. The element composition of TP347H stainless steel (Table. 12) meets the ASME standards. The corresponding metallographic microstructure after etching (etchant composition: 10 mL HCl + 10 mL H_2O + 2 g $CuSO_4$) is shown in Figure. 43. It clearly reveals that there are no visible inclusion phases in the austenite phase. The TP347H samples used in the following experiments were grinded subsequently by SiC abrasion paper up to 2000 grit, cleaned in acetone, rinsed with ethanol and dried in cold air. The dimension of these samples was fixed as 10 × 10 × 3 mm^3.

The coal ash was synthesized in lab with a composition (weight percentage) of 29.25% SiO_2, 29.25% Al_2O_3, 29.25% Fe_2O_3, 5.625% Na_2SO_4, 5.625% K_2SO_4 and 1% NaCl based on the analysis result of the coal ash obtained from Longview power plant, which is similar to other reports [29, 32, 33]. The salts were dissolved in distilled water followed by ultrasonication for 6 h and then drying at 450 ^oC. A layer of synthesized coal ash with a thickness of 1 mm was deposited on TP347H samples in all tests. The synthesized gas containing 1 vol. % SO_2, 4 vol. % O_2, 15 vol. % CO_2 and 80 vol. % N_2 was fed at a flow rate of 100 ml min^{-1} to simulate the corrosive atmosphere near the superheater in the power plant.

Table 12 Element compositions of TP347H steel

Element	C	Mn	P	S	Si	Cr	Ni	Mo	Nb	Fe
Weight ratio (%)	0.041	1.75	0.02	0.003	0.32	17.52	9.22	0.26	0.71	Bal.

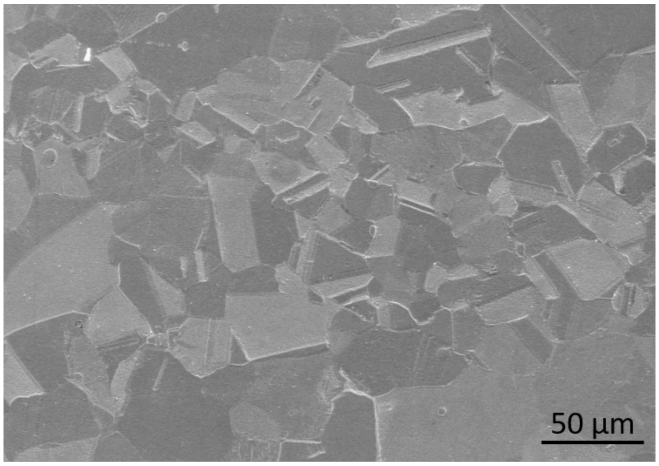

Figure.43 Metallographic microstructure of TP347H

Electrochemical tests including open circuit potential (OCP), potentiodynamic polarization (PDP) and electrochemical noise (EN) were carried out by utilizing a Gamry 5000E at 650 ^oC, 700 ^oC and 750 ^oC, respectively. All electrochemistry measurements were conducted by using the same set-up as our developed high temperature corrosion sensor [31] which is consisted of two identical working electrodes (WE1 and WE2), one reference electrode (RE) and one counter electrode (CE) [34]. Two identical TP347H SS specimens were acted as WE1 and WE2 which were sealed with ceramic paste (505N, Aremco Inc) leaving a working area of 1 × 1 cm^2. RE was the quartz sealed Cu/Cu^{2+} reference electrode which has been described in our previous work. The counter electrode was a platinum rod with a diameter of 2.5 mm (99% in purity, Surepure Chemetals Inc). Tungsten wire with a diameter of 0.4 mm (99% in purity, Midwest Tungsten Inc) was welded to these electrodes which was shielded inside a ceramic tube (AdValue Technology Inc) and sealed with ceramic paste to avoid exposure in the corrosive atmosphere. The initial OCP was measured for 1 h after reaching the target temperature. EN test consisted of measuring the potential of one of the working electrodes with respect to the Cu/Cu^{2+} reference electrode and was executed with a prolonged time of 168 h with a frequency of 1 Hz. Current noise was measured between the two working electrodes. The PDP test was performed at the end of the EN test with a scan rate of 0.5 mV s^{-1}.

The weight and exposure area of all TP347H specimens were recorded. At each working condition, four samples are placed in synthesized coal ash with the same flu gas for 7 d. After exposure, the corrosion products were removed in boiling water for 20 min followed by ultrasonic cleaning in acetone, then rinsing with distilled water and drying in cold air. The final weight was measured with the aid of a microbalance with an accuracy of 1×10^{-6} g.

The corrosion product on the top surface of samples was characterized by X-ray diffraction (XRD, PANalytical X'pert PRO, Cu Kα radiation). The surface and cross-section morphology of corrosion product and the corresponding element distribution mapping were characterized by a scanning electron microscope (SEM, Hitachi S-4700) equipped with an energy dispersive X-ray (EDX) analysis system.

5.2.2 Results

(1) Open circuit potential analysis

The initial potential of TP347H stainless steel as a function of time in the first hour at different temperatures is depicted in Figure. 44. As shown in Figure. 44, the OCP increases with time at 650 °C (from 150 mV to 290 mV (vs Cu/Cu^{2+})) and 700 °C (from 190 mV to 458 mV (vs Cu/Cu^{2+})) in the first hour while it shows an opposite trend at 750 °C, decreasing from 603 mV to 520 mV (vs Cu/Cu^{2+})) gradually. Since the predominant process, i.e., sulfidation, in coal ash hot corrosion always occurs in relatively positive potentials, the positive OCPs at 650 °C, 700 °C and 750 °C suggest the favorable occurrence of a sulfidation process [30, 35, 36]. Moreover, the OCP is higher at a higher temperature at all times in the hour.

When exposed in the oxidizing atmosphere at elevated temperatures, a protective oxide layer composed of oxides of nickel, chromium and their spinels is formed on the surface of TP347H stainless steel, which is similar to the layer on a nickel-based alloy [37, 38].

$$Ni\text{–}SO_3 + SO_4^{2-} \rightarrow NiO + 2SO_3 + 2e^- \qquad (1)$$

$$2Cr\text{–}SO_3 + 3SO_4^{2-} \rightarrow Cr_2O_3 + 5SO_3 + 6e^- \qquad (2)$$

$Ni\text{–}SO_3$ and $Cr\text{–}SO_3$ stand for the dissolution of Ni and Cr catalyzed by the adsorption of SO_3, respectively. This protective scale can effectively prevent the inward diffusion of oxidizing species in the molten salt and outward diffusion of alloy elements, thus mitigating corrosive attack and elevating the potential. Moreover, the growth rate of oxides is faster at a higher temperature. The reason leading to the decrease of OCP by time at 750 °C will be discussed in detail in the following sections.

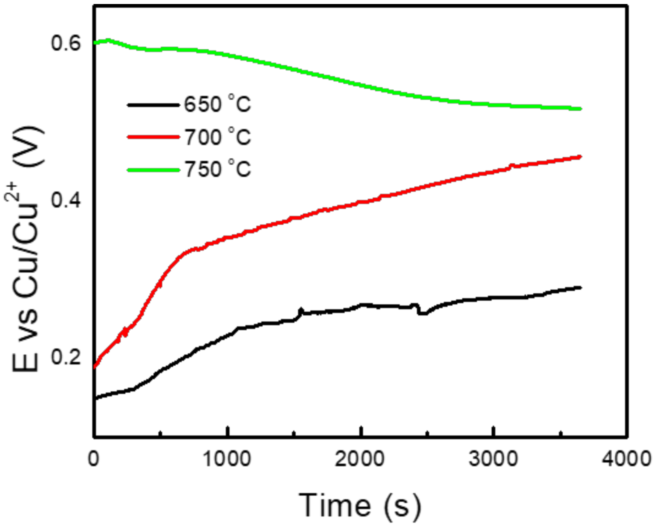

Figure.44 OCP as a function of time in the first hour at different temperatures

(2) Electrochemical noise analysis

The potential noise as a function of time in the first seven days at different temperatures (650 °C, 700 °C and 750 °C) is shown in Figure. 45, respectively. At 650 °C, the potential increases at the beginning, then decreases for a few hours followed by continuously rising to a constant value of 1.07 V (vs Cu/Cu^{2+}). When the temperature is 700 °C, the initial potential shows a similar trend as that at 650 °C. However, after 112 h, the potential suddenly drops from 1.07 V (vs Cu/Cu^{2+}) to 0.85 V (vs Cu/Cu^{2+}) followed by fluctuating between 0.8 V and 0.9 V (vs Cu/Cu^{2+}). The sudden drop of potential from 1.07 to 0.85 (vs Cu/Cu^{2+}) with no recovery suggests the accelerated sulfidation or oxidation process which will be discussed in the following section. In comparison, the potential at 750 °C grows to 1.07 V (vs Cu/Cu^{2+}) gradually, then fluctuates in a narrow range with an average value of 1.07 V (vs Cu/Cu^{2+}) followed by a sudden drop to 0.50 V (vs Cu/Cu^{2+}) after 65 h. However, after several hours, the potential recoveries to 1.07 V (vs Cu/Cu^{2+}).

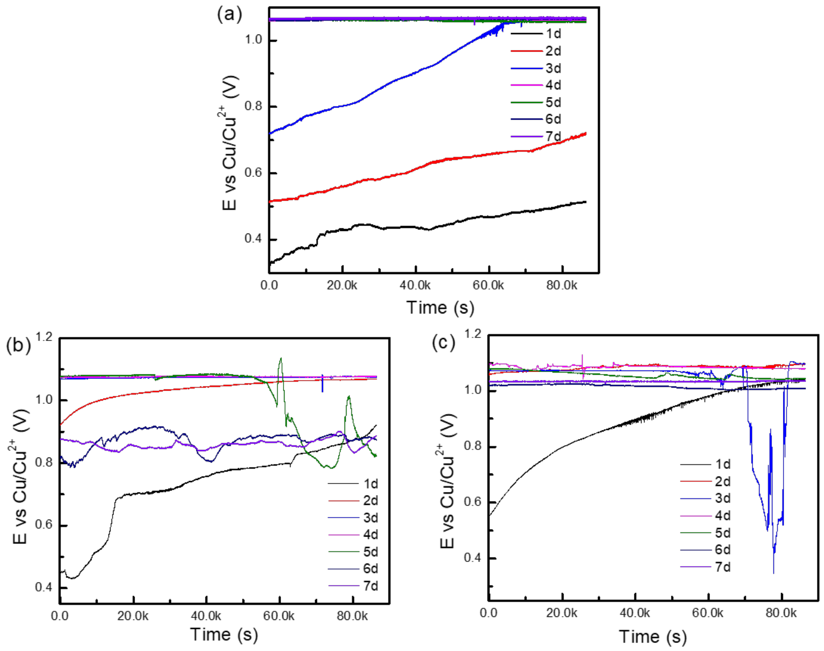

Figure.45 Time sequence of the electrochemical potential noise at (a) 650 °C, (b) 700 °C and (c) 750 °C

The corresponding current noise between the two working electrodes versus time is depicted in Figure. 46. The current becomes stable when the potential approaches 1.07 V (vs Cu/Cu^{2+}) regardless of the experimental temperature. The violent drifts of current in the first one or two days suggests the faster corrosion rate at the beginning, which might be ascribed to the lack of protection capability of corrosion products. Moreover, no visible variation of current is observed corresponding to the sudden drop or recovery of potential at 700 °C and 750 °C. It is important to note that there are numbers of spikes in current noise in the first few hours at 750 °C (Figure. 46c), suggesting the occurrence of pitting corrosion.

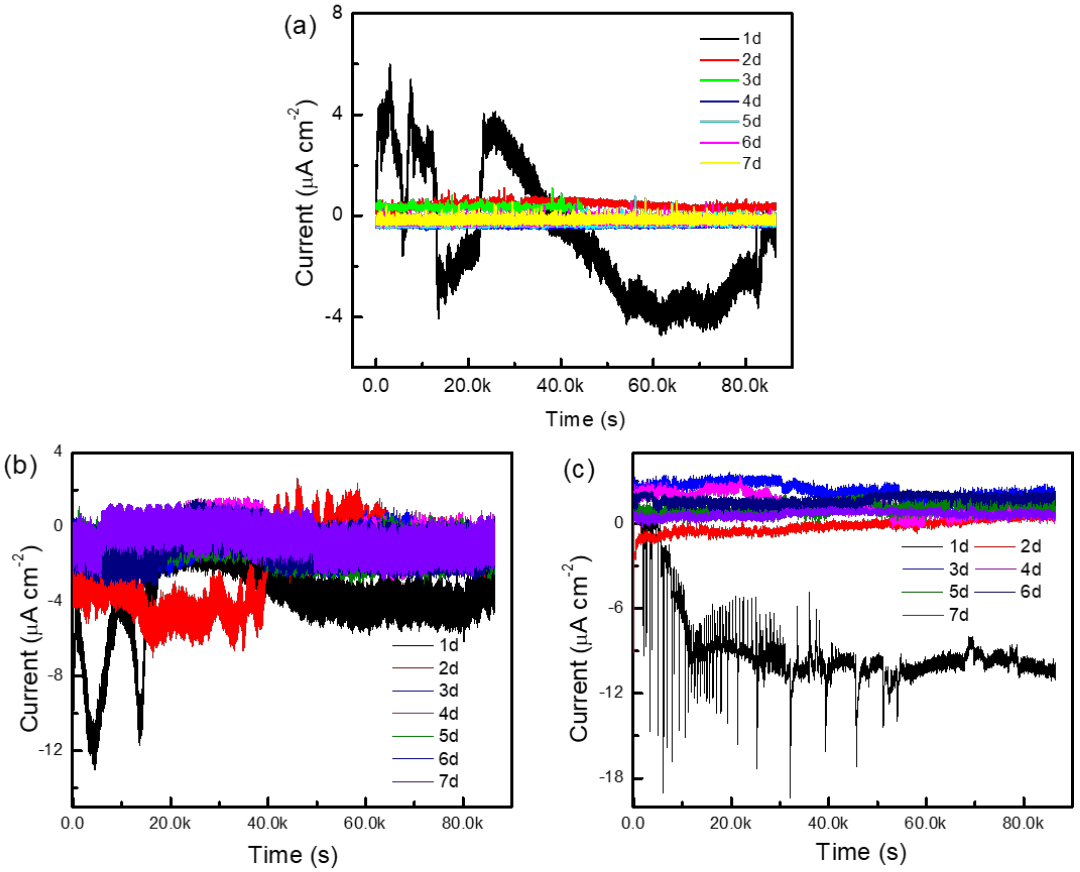

Figure.46 Time sequence of the electrochemical current noise at (a) 650°C, (b) 700°C and (c) 750°C.

Both the noise resistance in time domain (R_n) and the noise resistance in frequency domain (R_{sn}) can be acted as powerful tools to characterize the corrosion rate since they are inversely proportional to the corrosion rate. The minimum values of R_n and R_{sn} at 700 °C depicted in Figure. 47a suggest that the corrosion rate is fastest at this experimental temperature. The current density in frequency domain with the application of power spectral densities (PSDs) as a function of frequency is depicted in Figure. 48. It clearly shows that the current density in frequency domain at 700 °C is the highest, suggesting the fastest corrosion rate at 700 °C compared with that at 650 °C and 750 °C, which is consistent with the results shown in Figure. 6a.

Moreover, the localization index, the ratio between the standard deviation of the current noise and the root mean square of the current noise, shown in Figure. 47b indicates the occurrence of local corrosion of TP347H in these working conditions. But the trend of localization index at different temperature varies, suggesting various corrosion behaviors of TP347 at different temperatures.

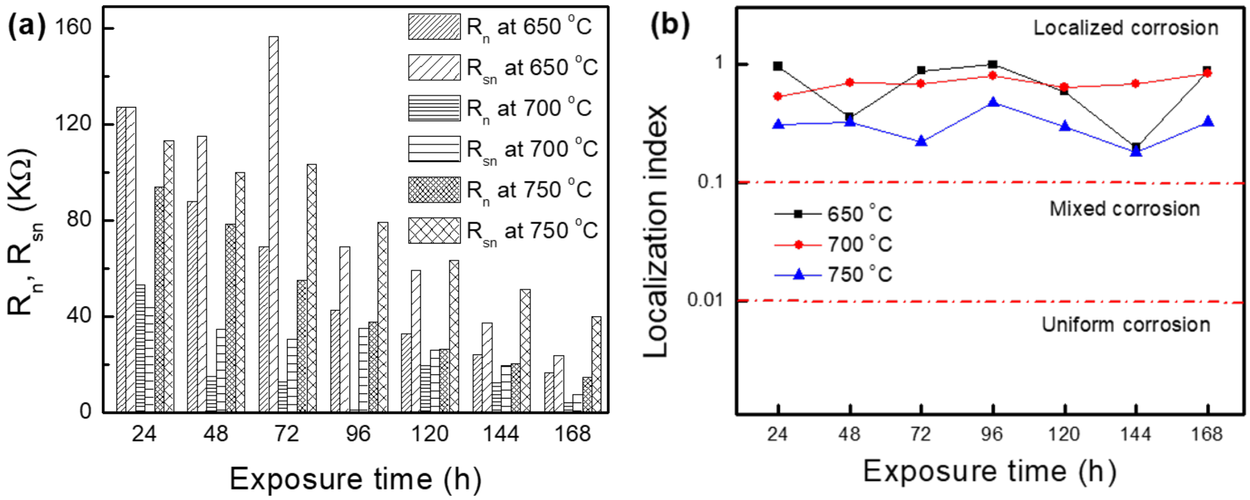

Figure.47 Comparison of (a) R_n and R_{sn} and (b) localization index at different temperatures

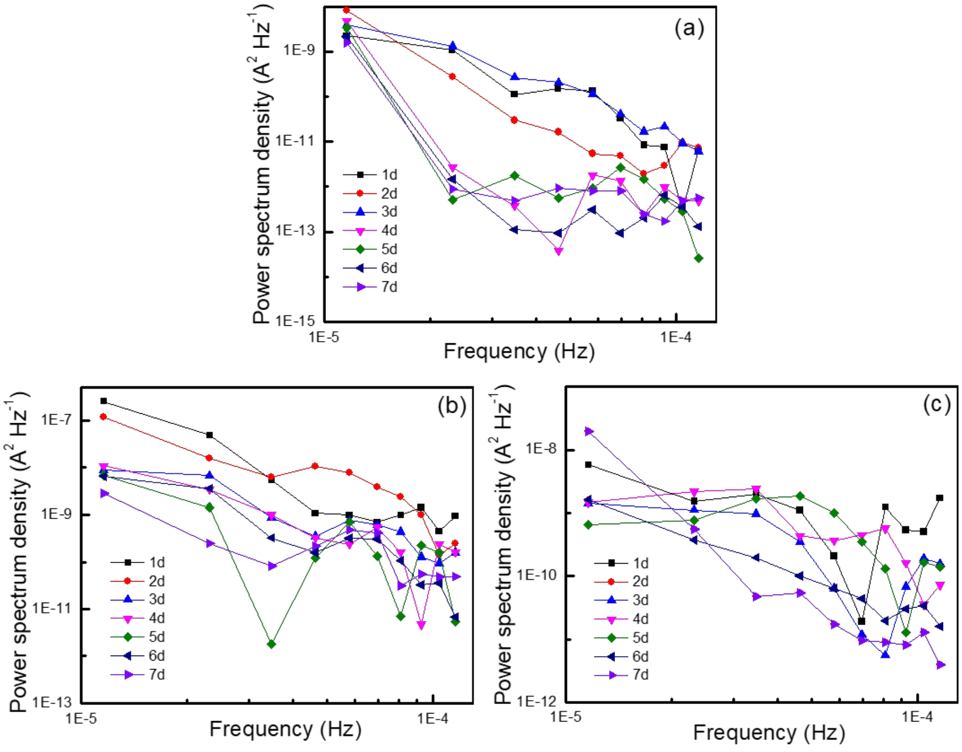

Figure.48 Frequency domain of the electrochemical current noise at (a) 650°C, (b) 700°C and (c) 750°C.

(3) Potentiodynamic polarization analysis

Figure. 49 depicts the potentiodynamic polarization curves and corresponding i vs E plots at different temperatures. The plots clearly reveal that the corrosion potential is lowest, and corrosion current density is highest at 700 °C, suggesting the poorest protection capability of the corrosion products at 700 °C. The corrosion rate might also be calculated with the application of PDP curve when the process is controlled by charge transfer step. However, due to the limited Tafel region of the PDP curve (Figure. 49a) and almost pure ohmic property of the electrolyte (Figure. 49b), it is impossible to quantitatively calculate the corrosion rate from the Tafel extrapolation method. Based on previous experiments, the linear current-potential behavior is not solely due to the uncompensated resistance in the three-electrode conFigureeuration [32]. This might be ascribed to the introduction of oxides (Al_2O_3, Fe_2O_3 and SiO_2) and metal oxides (Fe_2O_3 and Cr_2O_3) composed in the corrosion product which turns the molten sulfate salt (Na_2SO_4, K_2SO_4) into an electronic conductor [29, 30].

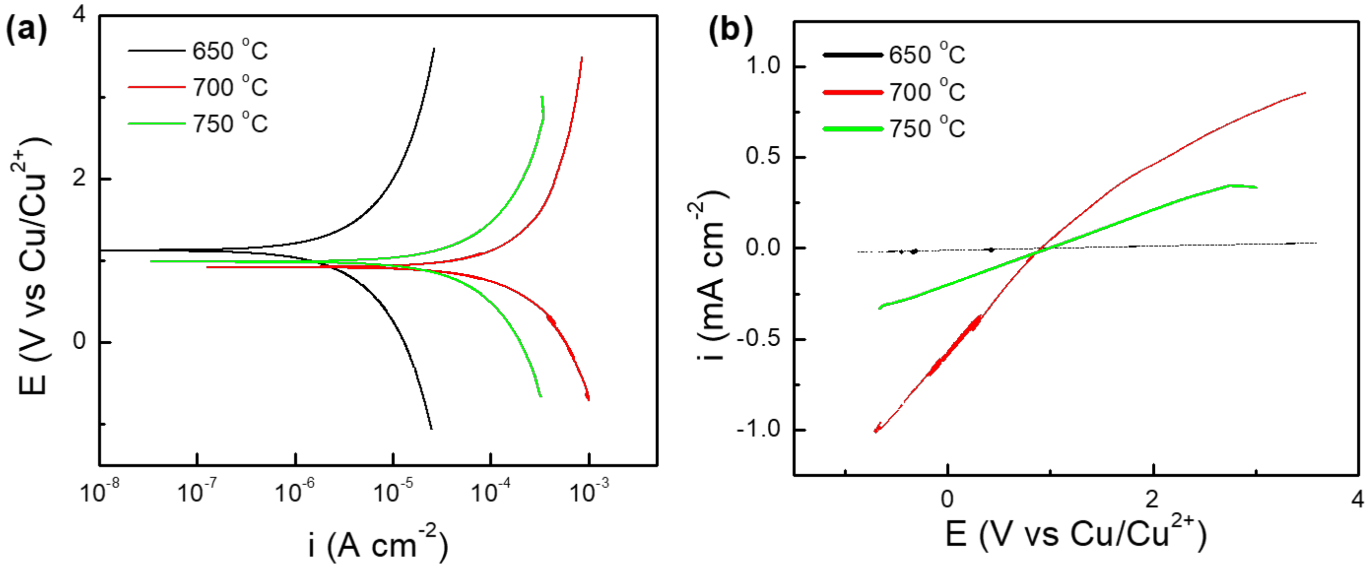

Figure.49 (a) Potentiodynamic polarization curve and (b) corresponding i vs E plots at different temperatures.

(4) Calculation of corrosion rate

Compared with other electrochemistry measurements such as EIS and PDP, EN can act as a powerful tool to provide real-time corrosion rate without any instrumental disturbances. According to the Faraday's law, when the potential difference between anode and cathode working electrodes is larger than 100 mV, the instantaneous localized corrosion rate at the anode can be calculated from the current density as discussed in our previous work [30]. In each 24 h, the maximum current value, i_{max}, is adopted to calculate the instantaneous localized corrosion rate, CR, g s^{-1} as shown in the following equation.

$$CR = (M \times i_{max})/Fn \qquad (3)$$

Wherein F is a Faraday's constant, i.e., 96485 C mol^{-1}; M represents the atomic mass of iron, i.e., 56 g/mol; n is for the number of electrons transferred per atom of iron, i.e., 3 by supposing all the iron atoms are oxidized to Fe^{3+}.

Assuming the corrosion rate is constant in one period, i.e., 24h, the total corrosion rate is calculated by eq. (4)

$$D = CR \times 86400 \qquad (4)$$

This method has been shown to provide good consistency with respect to weight loss measurements for the Inconel 740 superalloy [29, 30].

The corrosion rate calculated through eq (4) as a function of time at different temperature are given in Figure. 50. The corrosion rate is fastest at 700 °C, consistent with the results shown in Figure. 47a and Figure.48. However, the total corrosion rate in 7 days is far less than the experimental result obtained from weight loss measurements (3.34 mg cm^{-2} at 650 °C, 20.4 mg cm^{-2} at 700 °C and 14.7 mg cm^{-2} at 750 °C), suggesting this is a discrepancy between the calculated and experimental result in this system.

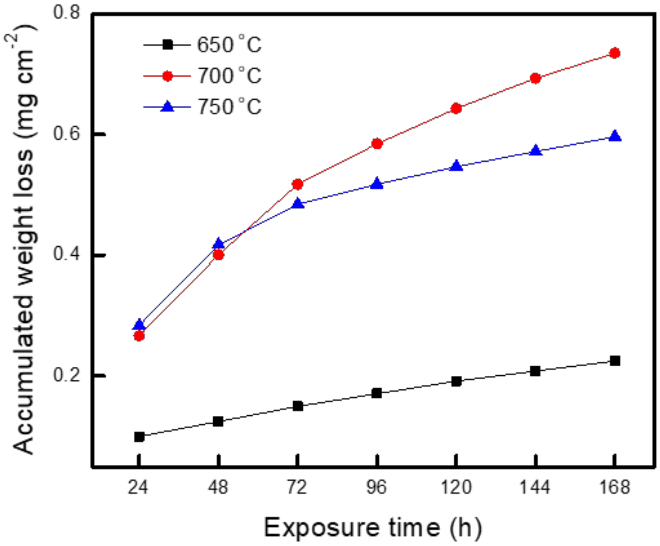

Figure.50 Accumulated corrosion rate calculated by EN data analysis at different temperatures.

(5) Corroded top and cross-sectional surface characterization

Figure. 51-53 show the cross-section morphology and element distribution of corroded TP347H after hot corrosion test at different experimental temperatures. The corrosion product consists of two layers, an outer layer mainly of chromium oxide and chromium sulfide, and an inner layer composed of iron oxide and iron sulfide regardless of the experimental temperature. The outer layer at 650 °C is much denser than that at 700 °C and 750 °C which is consistent with the surface morphology and corresponding EDX result shown in Figure. 54-56. The inner layer is porous at three different temperatures. The thickness of corrosion product shows a maximum value at 700 °C which is consistent with the calculated corrosion rate result shown in Figure. 50. Moreover, the EDX results on the superficial corrosion products shown in Figure. 54-56 confirm the existence of Cr, Fe, O and S. The XRD pattern depicted in Figure. 57 further confirms the existence of Cr_2O_3, Fe_2O_3, Cr_3S_4 and Fe_3S_4.

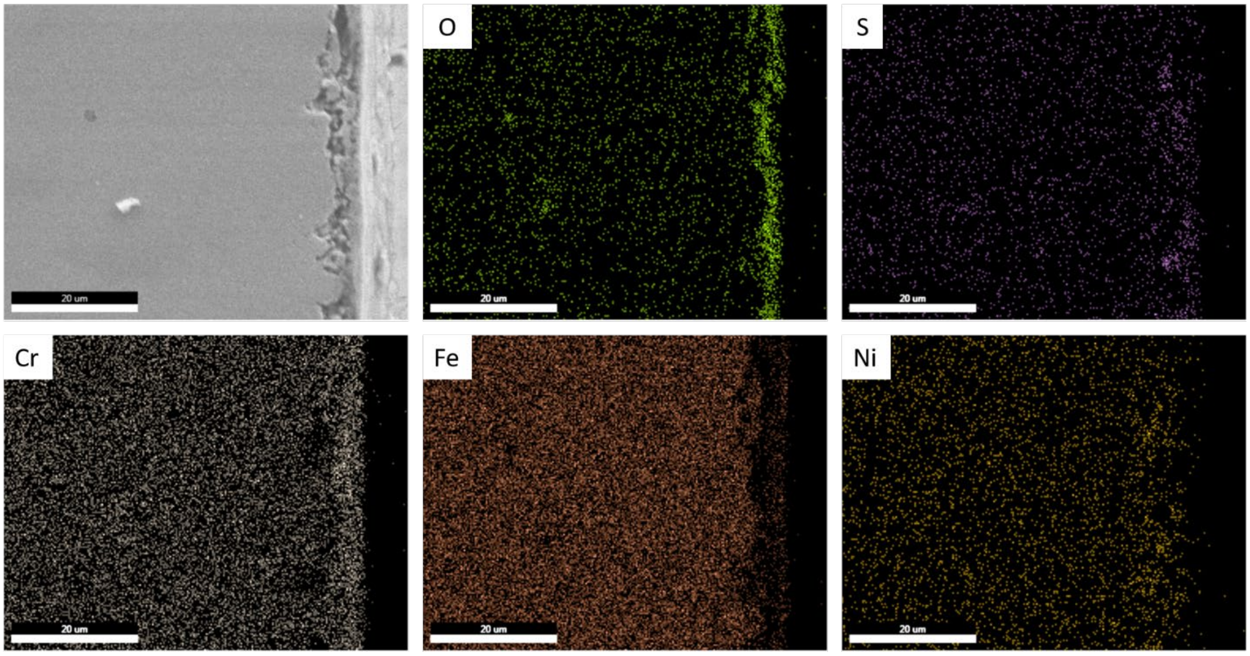

Figure.51 Cross section morphology and element distribution of TP347H after hot corrosion at 650 °C.

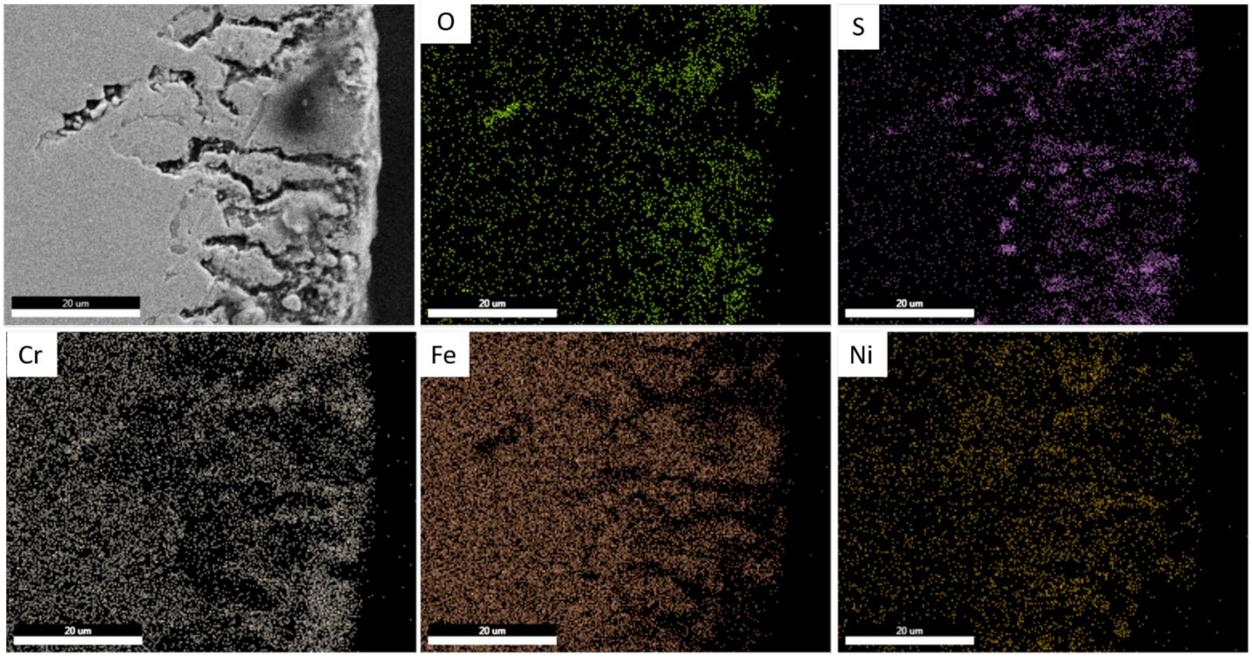

Figure.52 Cross section morphology and element distribution of TP347H after hot corrosion at 700°C.

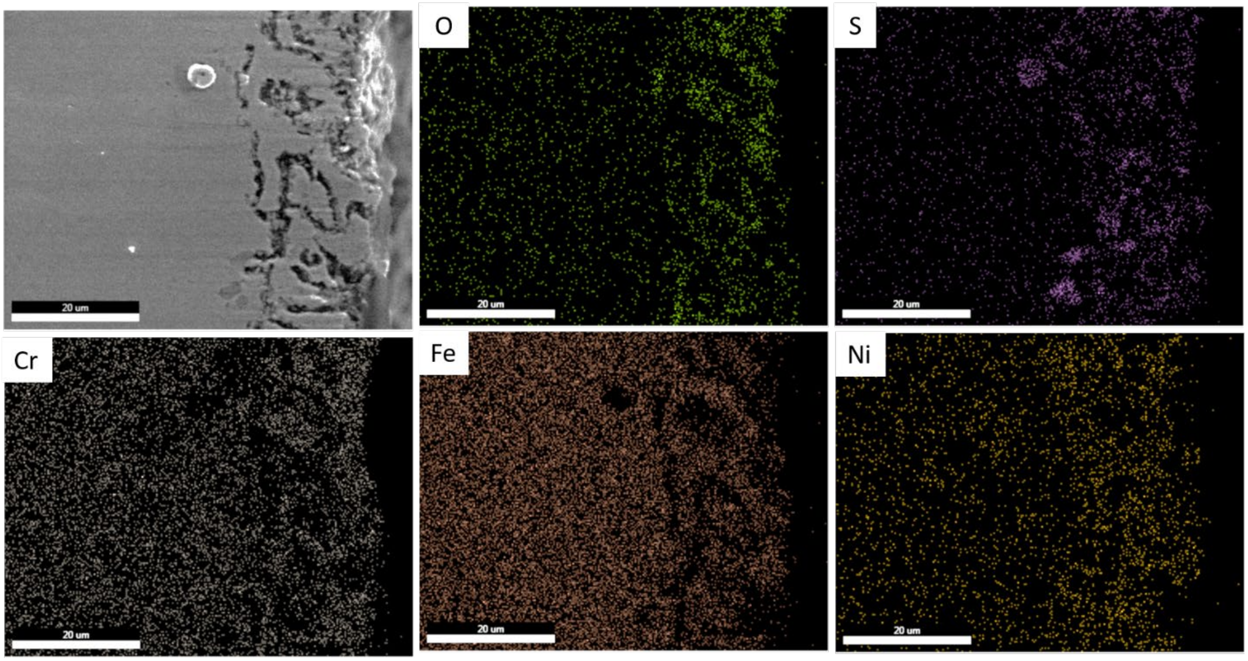

Figure.53 Cross section morphology and element distribution of TP347H after hot corrosion at 750 ^{o}C

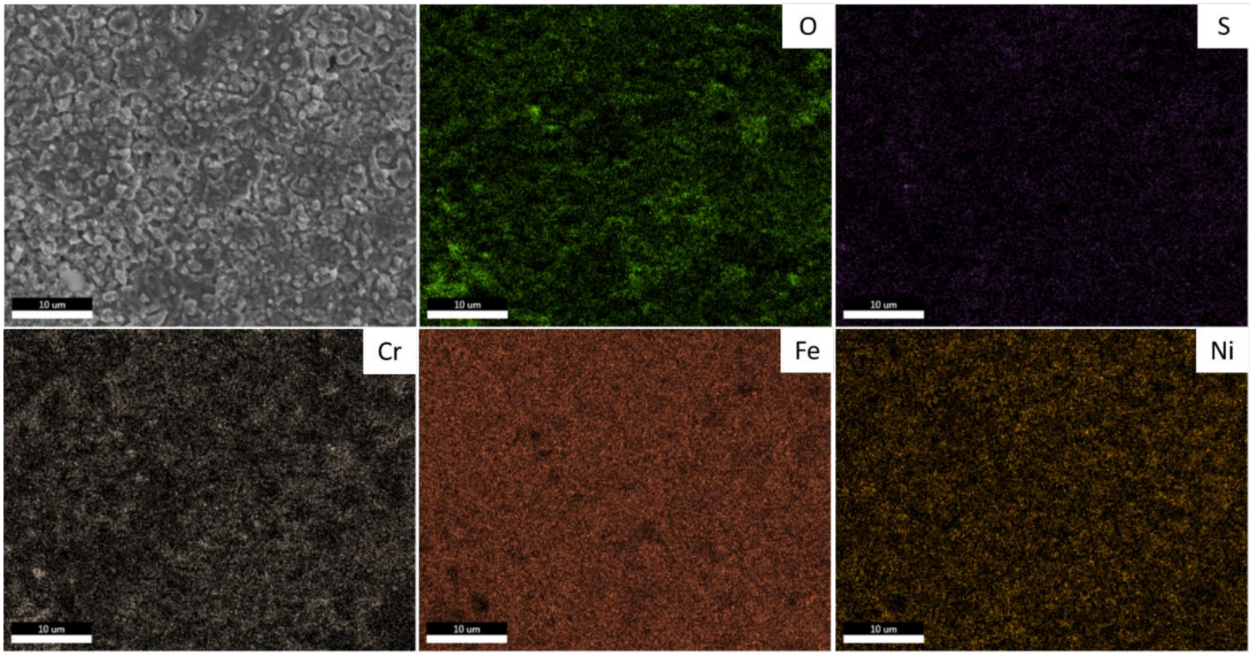

Figure.54 Surface morphology and element distribution of TP347H after hot corrosion at 650 ^{o}C.

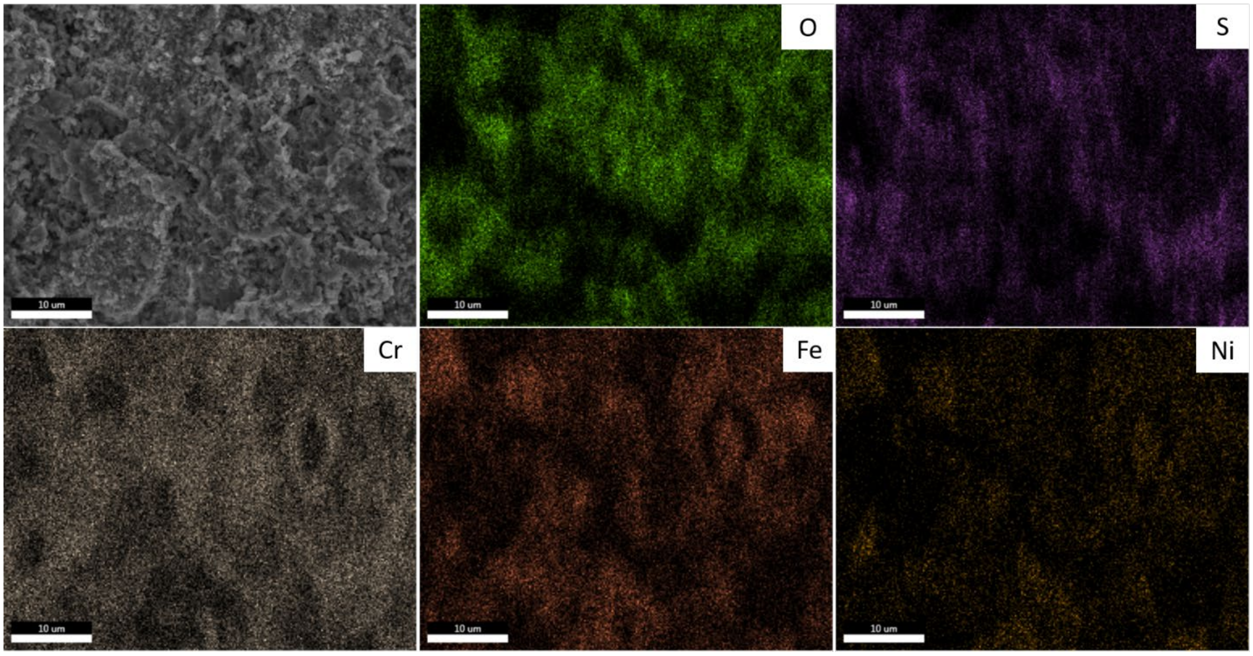

Figure.55 Surface morphology and element distribution of TP347H after hot corrosion at 700 ^oC.

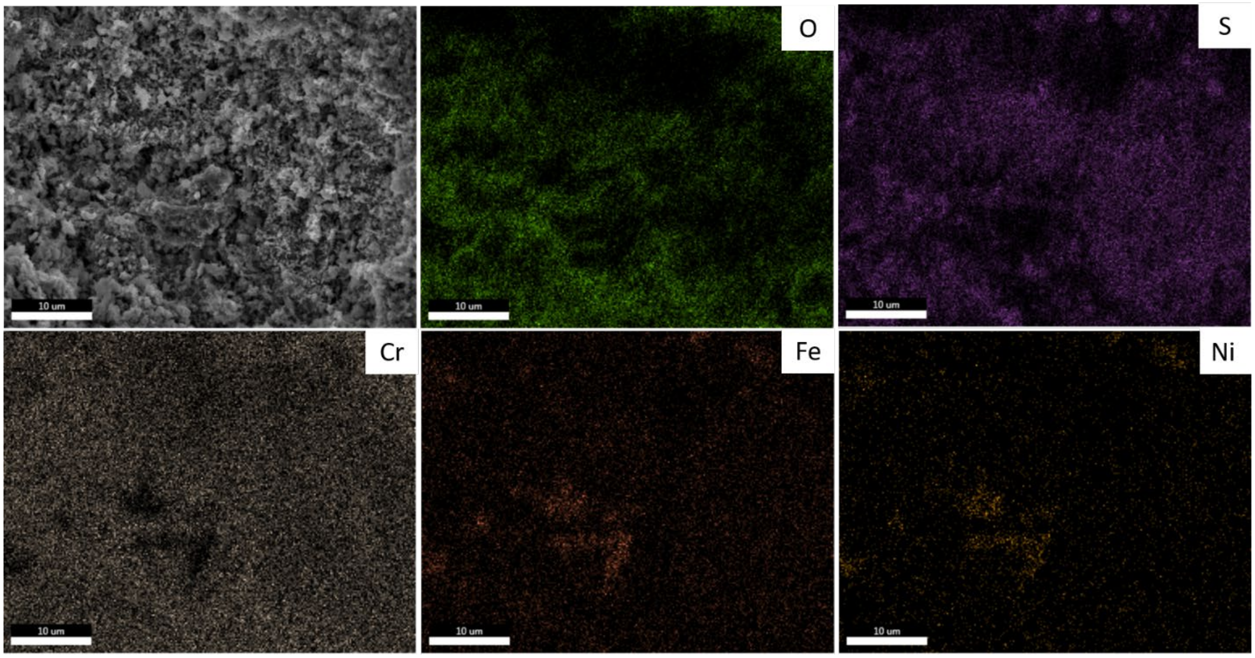

Figure.56 Surface morphology and element distribution of TP347H after hot corrosion at 750 ^oC

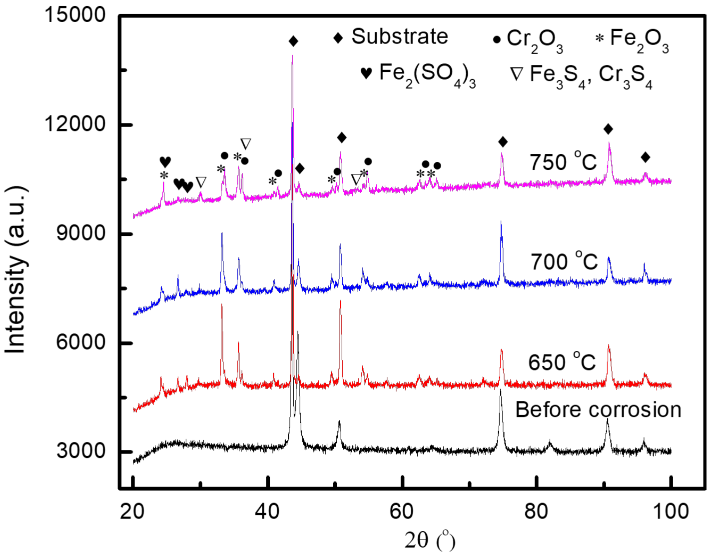

Figure.57 XRD pattern of blank and corroded TP347H at different temperatures.

5.2.4 Discussion

(1) Formation of molten salt

It has been recognized that the main chemical involved in hot corrosion is Na_2SO_4 due to its extraordinary stability in a wide range of oxygen potential and temperature [39, 40]. The melting point of Na_2SO_4 is 884 °C which is much higher than the experimental temperatures (i.e., 650 °C -750 °C). However, the inclusion of metal oxide, e.g., Fe_2O_3, in alkaline sulfate (i.e., Na_2SO_4 and K_2SO_4) facilitates the formation of eutectic salts, i.e., $Na_3Fe(SO_4)_3$ and $K_3Fe(SO_4)_3$, which significantly lowers the melting temperature of the sulfate salts [32].

Moreover, sulfur trioxide (SO_3), formed by O_2 and SO_2 through Eq. (5), easily partitions into the molten sulfate layer due to its conversion to pyrosulfate through Eq. (6).

$$2SO_2 + O_2 \rightarrow 2SO_3 \qquad (5)$$

$$SO_3 + SO_4^{2-} \rightarrow S_2O_7^{2-} \qquad (6)$$

The formation of $Na_2S_2O_7$ and $K_2S_2O_7$ further lowers the melting point of the sulfate/pyrosulfate salts. The melting points of $Na_2S_2O_7$, $K_2S_2O_7$, $Na_3Fe(SO_4)_3$ and $K_3Fe(SO_4)_3$ are 400.9 °C, 325 °C, 624 °C and 618 °C, respectively [32]. Furthermore, the melting point of eutectic salt is lower than that of a pure salt. Therefore, molten salt can be easily formed even at the lowest experimental temperature, i.e., 650 °C, which would result in hot corrosion of TP347H exposed in this experimental environment.

(2) Correlation between hot corrosion process and characteristic potential noise patterns

The hot corrosion in molten sulfate salt is a two-step process: initiation and propagation. However, due to the absence of electrochemistry measurements, there are few reports revealing the details about the hot corrosion process. To provide a deeper understanding of hot corrosion, the quantitative relationship between electrochemical noise and the progress of corrosion is identified in the following section based on the experimental results above.

The corrosion process can be divided into five steps according to the potential noise patterns shown in Figure. 58. The schematic of characteristic potential noise pattern and corresponding hot corrosion process of TP347H are depicted in Figure. 58 and 59, respectively.

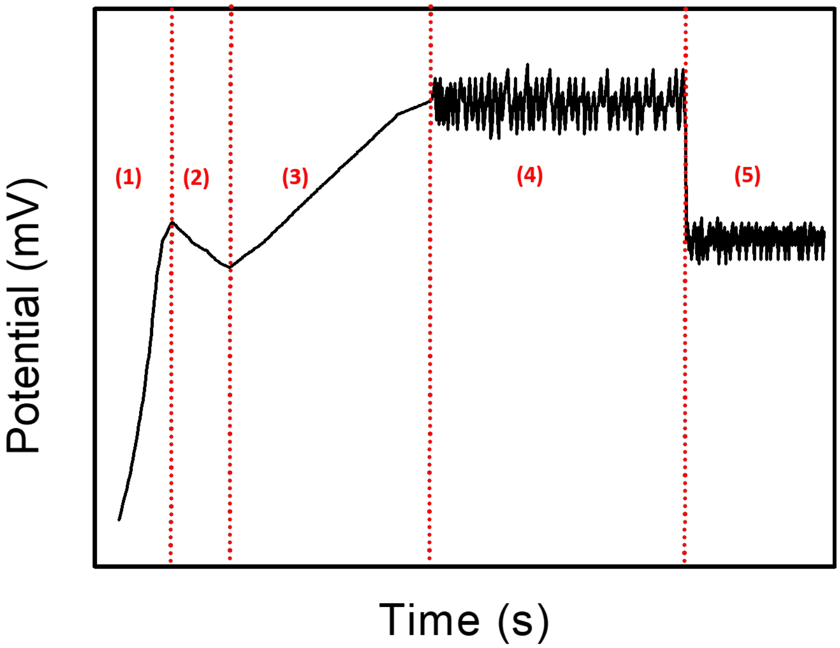

Figure.58 The schematic of potential noise of TP347H stainless steel in coal ash. See the text for a description of each step.

As TP347H is exposed in the oxidizing atmosphere, a thin passive film mainly composed of chromium oxide is formed on the top layer (Figure. 59a: initial state). With the increase of experimental temperature, the sulfate salt begins to melt. Before the formation of an intact molten salt or a relatively thick molten salt layer to fully separate TP347H from the oxidizing atmosphere, a thin layer of protective scale mainly composed of chromium oxide, nickel oxide and their spinels as shown in eq (1) and (2) is formed on the top surface along with the formation of iron oxide (Figure. 59b: direct oxidation), hindering the further ingress of oxidizing species and outward diffusion of alloy elements, thus leading to the increase of potential (step 1 in Figure. 58). Moreover, a higher temperature promotes the outward diffusion of alloy elements and the oxidization rate, thickening the protective layer, indicated by a higher potential at corresponding times as shown in Figure. 3 and 4. The successful measurement of potential during this process might be ascribed to the formation of a layer of reticulated molten salt which could also be acted as an ionic or electronic conductor.

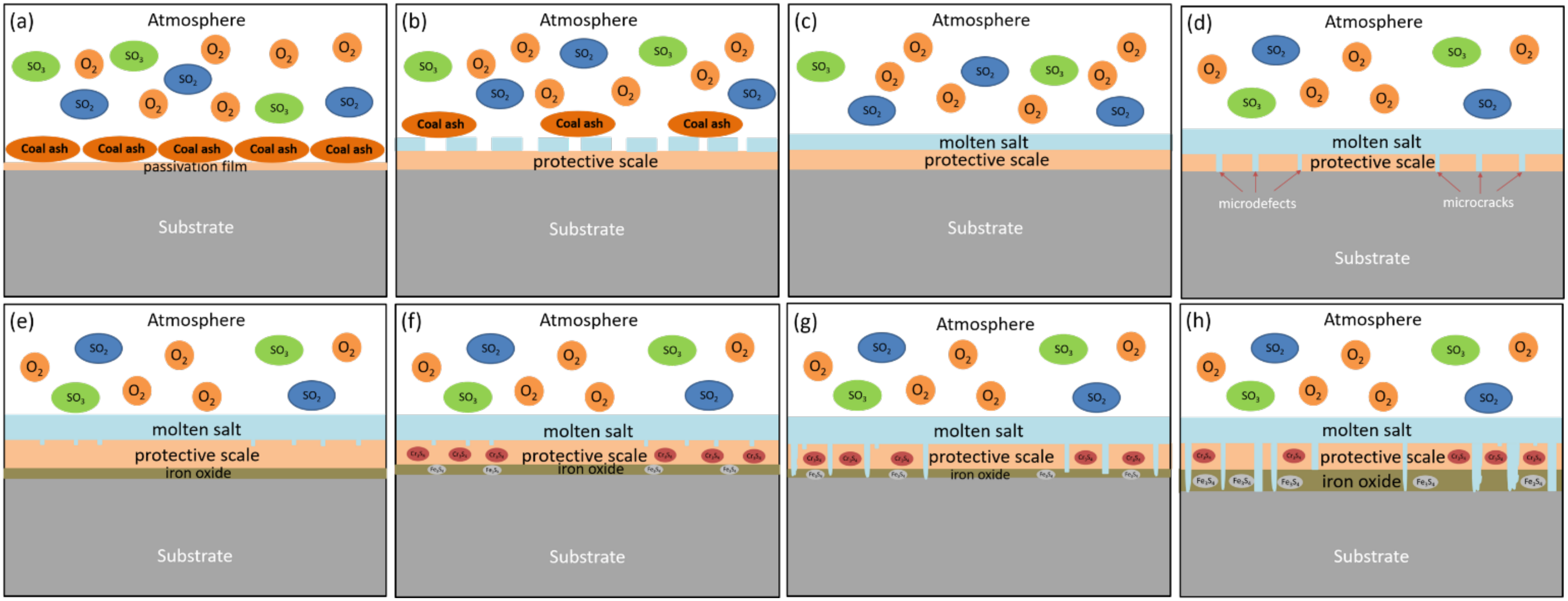

Figure.59 The schematic of hot corrosion process of TP347H in coal ash (a: initial state; b: direct oxidation before the formation of an intact molten layer; c: formation of continuous molten salt; d: dissolution of protective scale; e:oxidation; f: sulfidation; g: decomposition of protective scale; h: continuous sulfidation).

Generally, a minimum of 25% chromium is necessary to guarantee the formation of a dense and continuous chromium oxide layer to provide the satisfactory protection capability. However, the weight percentage of chromium in TP347H, 18%, is lower than the minimum value. Once the sulfate salt is fully melted (Figure. 59c: formation of continuous molten layer), the dissolution of protective scale and iron oxide occurs as shown in eq. (7) and (8) (Figure. 59d: dissolution of protective scale). The XRD data in Figure. 57 confirms the existence of $Fe_2(SO_4)_3$ in corrosion product, proving the acidic dissolution of iron oxide through eq. (8). The dissolution process lowers the density of protective oxide layer and weakens the protection capability, leading to the decrease of potential (step 2 in Figure.58).

$$Cr_2O_3 + 3Na_2SO_4 = Cr_2(SO_4)_3 + 3Na_2O \qquad (7)$$

$$Fe_2O_3 + 3Na_2SO_4 = Fe_2(SO_4)_3 + 3Na_2O \qquad (8)$$

The incubation time is also closely related to the experimental temperature. It is clearly shown in Figure. 3 and 4 that the period of initiation process is shorter at a higher temperature due to the accelerated electrochemical reaction rate in eq (7-8).

Once the molten salt penetrates through the microcracks or microdefects in the protective scale to the surface of the TP347H substrate (Figure. 59d), electrochemical reactions take place to achieve chemical equilibrium since the base metal can’t be stable when exposed to molten salt [41, 42].

The main anodic reactions are shown in eq (9-10).

$$Fe - 3e^- \rightarrow Fe^{3+} \qquad (9)$$

$$Cr - 3e^- \rightarrow Cr^{3+} \qquad (10)$$

The anodic reactions lead to the physical dissolution of the bare substrate . As $S_2O_7^{2-}$ formed through eq. (6) is a more active oxidant than O_2 and SO_4^{2-}, the main cathodic reaction is [9, 29, 40]

$$S_2O_7^{2-} + 2e^- \rightarrow SO_4^{2-} + SO_2 + O^{2-} \qquad (11)$$

The combination of eq (9-10) and eq. (11) leads to the formation of Cr_2O_3 and Fe_2O_3 (XRD data in Figure. 57) which might restore the porous protective scale or even promote the growth of protective scale, thus enhancing the resistance against hot corrosion indicated by the growth of potential (step 3 in Figure. 58 and Figure. 59e: oxidation).

Due to the limited dissolution of oxygen in molten salt and continuous consumption of oxygen as a consequence of the formation of metal oxides, i.e., Cr_2O_3 and Fe_2O_3, the partial pressure of oxygen at the salt/scale interface decreases with time [43]. According to the Na-S-O phase stability diagram [40, 44], $S_2O_7^{2-}$ is further reduced to form S^{2-} and O^{2-} through eq. (12) once the partial pressure of oxygen is below a certain value [9, 10, 44]. Moreover, some Fe^{2+} and Cr^{2+} are formed due to the partial oxidation of base metal as shown in Eq. (13-14).

Further reduction of $S_2O_7^{2-}$ in low partial pressure of oxygen,

$$S_2O_7^{2-} + 8e^- \rightarrow SO_4^{2-} + S^{2-} + 3O^{2-} \qquad (12)$$

Partial oxidation of base metal,

$$Fe - 2e^- \rightarrow Fe^{2+} \qquad (13)$$

$$Cr - 2e^- \rightarrow Cr^{2+} \qquad (14)$$

The combination of the cathodic reaction (eq.(12)) and anodic reactions (eq (9,10,13 and 14) leads to the formation of metal oxides (i.e., Cr_2O_3, Fe_2O_3) and metal sulfides (i.e., Fe_3S_4, Cr_3S_4) , which is in agreement with the XRD result shown in Figure. 57 (step 4 in Figure.7 and Figure. 59f: sulfidation). Figure. 60 shows the surface morphology and the EDX analysis of the corrosion products at 700 °C, further supporting the co-existence of chromium sulfide, chromium oxide, iron sulfide and iron oxide.

The sulfidation process in hot corrosion is always indicated by the fluctuation of potential in a small range, which has been demonstrated by the study of the coal ash hot corrosion of 740 nickel-based alloy in our previous work [29, 30].

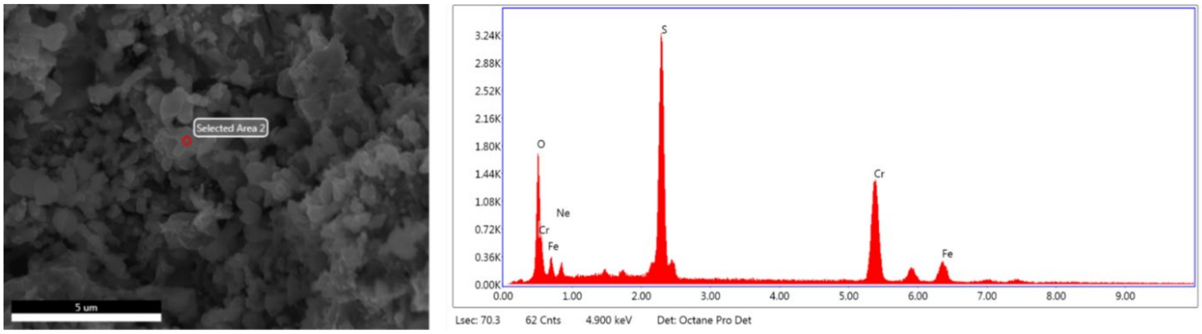

Figure.60 Surface morphology and element distribution of corrosion product after hot corrosion at 700 °C.

The sudden drop of potential in seconds after a certain time at 700 °C and 750 °C in Figure. 4 might be ascribed to the destruction of protective scale. As discussed before, the dissolution of protective scale is much faster at a higher temperature. At 650 °C, no rapid drop of potential is observed in the exposure period due to the relatively slow disintegration of protective scale. This observation is consistent with the cross-section morphology of corrosion product depicted in Figure. 10-12 in which the outer layer in corrosion product at 650 °C is much denser than that at 700 °C and 750 °C. In contrast, after the exposure of 112 h, the potential suddenly drops from 1.07 V (vs Cu/Cu^{2+}) to 0.85 V (vs Cu/Cu^{2+}) in seconds at 700 °C due to the accelerated dissolution process. A further increase of temperature to 750 °C shortens the time (56 h) taken to destroy the protective scale (Figure. 59g: decomposition of the protective scale). Therefore, the occurrence of the sudden drop of potential is earlier at 750 °C than at 700 °C. Moreover, this sudden drop is not recoverable at 700 °C. The recovery of potential in several hours at 750 °C will be discussed in detail in the following section.

In this following step 5 in Figure.58, the potential still fluctuates around a lower value due to the impairment of protective scale. The current noise shows a similar trend as step 4 without any visible differences. Moreover, sulfur is uniformly distributed on the TP347H substrate instead of locally accumulated along the grain boundaries, which is confirmed by EDX after polishing and etching. Step 5 is considered as a continuous sulfidation process in which the electrochemical reactions are same as that in step 4 (Figure. 59h: continuous sulfidation).

(3) The effect of temperature on hot corrosion of TP347H

The increase of temperature promotes both the diffusion of oxidants (i.e., oxygen and sulfur trioxide) and alloy elements and the reaction kinetics (i.e., the reduction of pyrosulfate ions and the oxidation of TP347H). This is the reason that it takes a shorter time for the potential approaching the stable value, i.e., 1.07 V (vs Cu/Cu^{2+}) at a higher temperature (Figure. 4). Moreover, the dissolution rate of protective scale is relatively slow at 650 °C. Therefore, the outer layer mainly composed of chromium oxide dispersed with some chromium sulfide is continuous (Figure. 61a) and no sudden drop of potential has been observed (Figure. 4(a)). In contrast, the dissolution rate is accelerated at a higher temperature, i.e., 700 °C and 750 °C, thus impairing the protection capability of protective scale which are porous (Figure. 61b and c) and lowering the potential (Figure. 4(b) and (c)). The sudden drop of potential at 700 °C is not recoverable. However, the potential was recovered in several hours at 750 °C which is ascribed to the instability of $Fe_2(SO_4)_3$. At 750 °C, $Fe_2(SO_4)_3$, i.e., the products of the dissolution of iron oxide shown in eq. (8), is decomposed to Fe_2O_3 which would restore the protective scales and suppress the further dissolution of Fe_2O_3 [45, 46], thus hindering the diffusion of SO_3 through the molten salt to the oxide/salt interface. This explanation can be confirmed by the lowest peak density of $Fe_2(SO_4)_3$ at 750 °C shown in Figure. 16. Therefore, TP347H shows a maximum corrosion rate at 700 °C. Similar results have also been found by Hendry and Lees in which all of three different austenitic steels (AISI 316, AISI 347 and Esshete 1250) have a maximum corrosion rate at 680 °C in a temperature range of 600 °C -750 °C in the simulated coal fired boiler environment (salt composition: 6 mol% $Fe_2(SO_4)_3$ + 74 mol% Na_2SO_4 + 20 mol% K_2SO_4; gas composition: 15% CO_2 + 1% O_2 + 0.3% SO_2 + 83.7% N_2) [47].

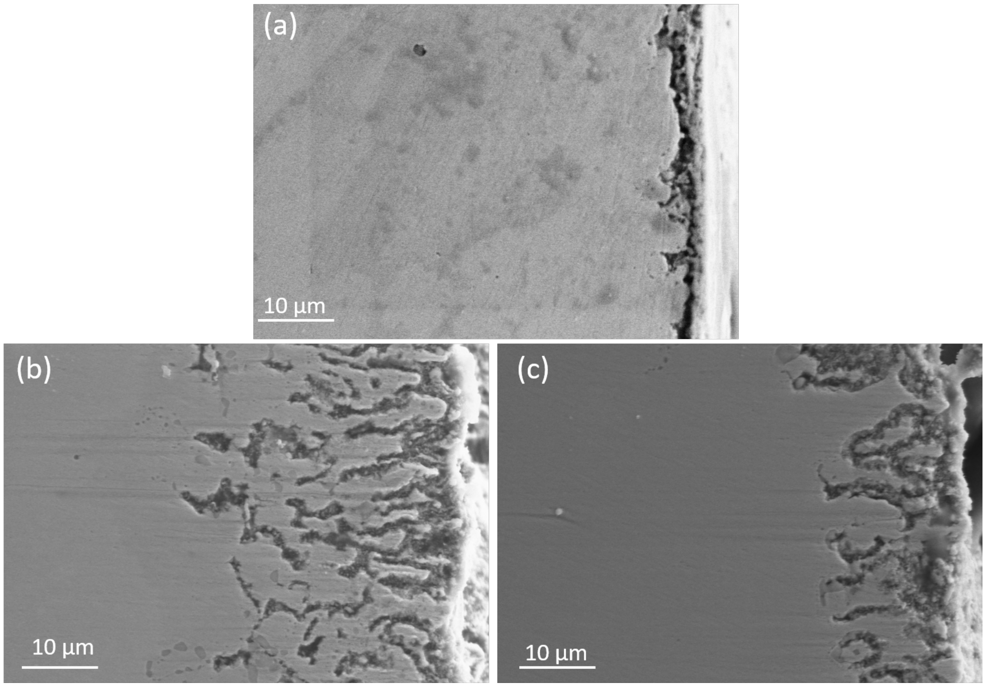

Figure.61 Cross section morphology TP347H after hot corrosion at different temperatures.

5.2.4 Conclusion

In this work, EN has been used to characterize the hot corrosion process of TP347H in coal ash in the temperature range of 650 °C -750 °C. According to the characteristic patterns of redox potential and current noise vs time, the process is divided into five steps: direct oxidation; dissolution of protective oxide; oxidation; sulfidation; and continuous sulfidation after the decomposition of the protective scale. The corrosion product is divided into two layers, an outer layer mainly composed of chromium oxide with some chromium sulfide and an inner layer mainly consisting of iron oxide and iron sulfide. The outer layer is much denser at 650 °C than that at 700 °C and 750 °C. A maximum corrosion rate is found at 700 °C. The decrease of corrosion rate at 750 °C is ascribed to the decomposition of $Fe_2(SO_4)_3$ to Fe_2O_3.

Task 6 Tech-transfer & commercialization

One of the vital boiler components that undergo damage is the waterwall. From 2012 to 2017, on an average, about 6.4% of annual potential production was lost due to forced outages caused by waterwall failure, making it the top cause of revenue loss. The primary reason for damage to tubes in the waterwall section is corrosion, which is accelerated due to load following. However, monitoring corrosion in real-time in the harsh environment is difficult. The corrosion sensor developed as part of this project can be a valuable instrument for that. However, placing corrosion sensors at all locations inside the waterwall section is not feasible. Thus, the optimal placement of sensors is crucial for real-time corrosion monitoring of the waterwall section. The proposed sensor network provides estimates of the corrosion depth along the entire length of the waterwall tubes. This would, in turn, enable estimation of the failure time of the waterwall tube due to corrosion. By planning maintenance activities accordingly, forced outages due to corrosion can be avoided, increasing plant availability. The improved plant availability can enable the plant to produce more electricity. But the actual electricity produced, and the plant's profit depend on the market demand and price. Due to similar improvements in the availability of other plants and rapid deployment of renewables, stochasticity in the market demand and price is large. Several factors, like population growth, industrial growth, technological improvements in renewable and non-renewable energy technologies, etc., affect the market dynamics and, in turn, the cost of electricity. To capture these aspects, economic analysis is conducted using energy market forecasting software, which can provide information about the change in electricity production because of the higher availability of the power plant.

The report is divided into two sections. The first section explains corrosion modeling, corrosion estimation, and optimal sensor network. The second section includes the scenario-based economic analysis, payback period analysis, and corresponding sensitivity studies' results.

Task 6.1 Corrosion estimation

(1) Corrosion model development

Hot corrosion is the mechanism of corrosion experienced on the fireside of the waterwall. For metal temperatures under 900°C, the corrosion is mostly parabolic in nature.(Vasantasree and Hocking 1976) Hence, to simplify the calculation, a general assumption is made here that the corrosion rate is parabolic in nature. Generally, the corrosion rate monotonically increases with metal temperature until it reaches a maximum value of approximately 700°C, after which drops drastically, giving rise to a bell-shaped curve. The spread and height of this bell-shaped curve is a function of alloy composition.(Pettit 2011) Fireside tube-metal surface temperature, and concentration of SO_2 and O_2 in combustion gases surrounding the metal surface are the key factors that influence hot corrosion. Using these as inputs, inhibition model based expression was developed for the parabolic rate constant. The parameters of the corrosion model are alloy specific. Iron base alloys, and nickel-based alloys with chromium are commonly used for the construction of superheater and waterwall. Zhang et al have summarized the studies on deposit induced hot corrosion of Fe-based alloys in oxidizing and sulfidizing environment.(Zhang and Wu 1993) Corrosion depth data of alloy Fe-20Cr from their work has been used to calculate the corrosion model parameters. The model results and literature data for Fe-20Cr alloy are presented in Figure 62, where the model results are closely following the literature data with little discrepancies.

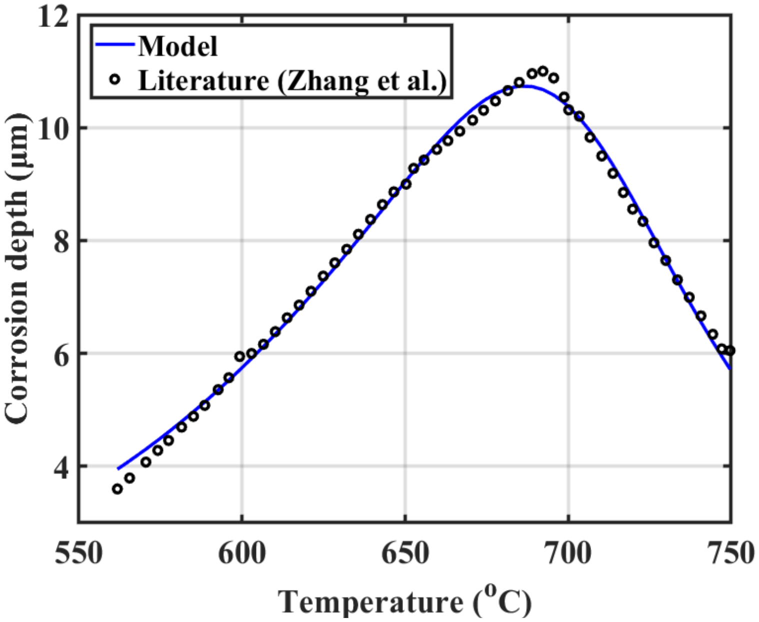

Figure 62: Comparison of literature values (Zhang et al) and corrosion model results of corrosion depth with temperature

(2) Corrosion model validation

Electrochemical sensors have been placed in the power plant of our industrial partner to monitor corrosion depth. One of the electrochemical probes is placed on the 11th floor to monitor corrosion depth on the superheater. The field measurements from this sensor were provided for 47 days and are used to validate the corrosion model. The superheater in this power plant is made of the alloy TP 347H which is an austenitic stainless steel. The temperature at the probe's location is 550°C. But the exact O_2 and SO_2 concentrations are not known. Hence, O_2 and SO_2 concentrations are considered from open literature. The percentage error between the corrosion model results and the industrial data are presented in Figure 63. The percentage error between them eventually approaches zero, thus validating the model.

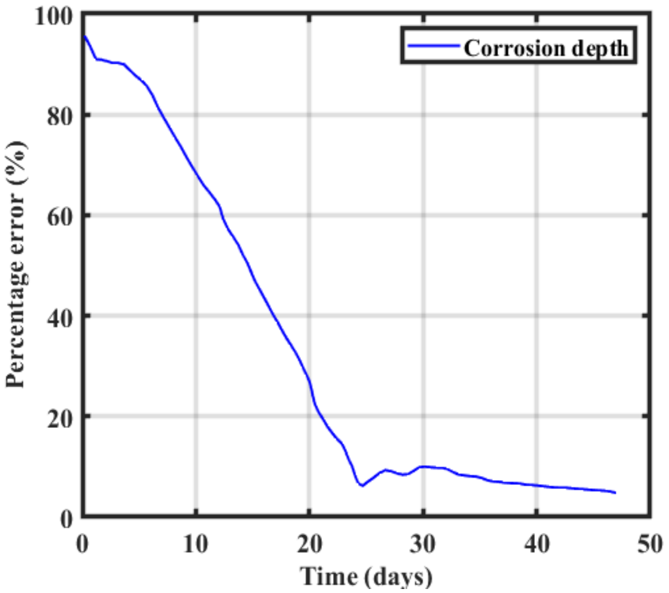

Figure 63: Plot of percentage error between plant data and corrosion depth from model, with time

(3) Corrosion estimation

State estimation is integral to optimal sensor network design. Kalman filter (KF) and its variants are the most widely used estimation techniques. The corrosion model used in this work is highly nonlinear. Some states of this system like metal temperature, and gas concentration can fluctuate significantly within a day due to load following. Whereas corrosion buildup is a slow process happening in the order of micrometers per year. Rupture of the tube surface occurs once its thickness drops below a threshold value. Hence, corrosion estimates need to have minuscule error. Based on these requirements of the system, Unscented Kalman filter (UKF) is used for estimation as it can handle the nonlinear multi timescale system and produce highly accurate estimates of corrosion depth.(Julier, Uhlmann, and Durrant-Whyte 1995)

Corrosion monitoring in this work is performed on waterwall section of a boiler system which is based on work by Seltzer at al.(Seltzer, Fan, and Robertson 2006) Dimension of waterwall section, burners' placement, O_2 concentration and gas velocity in the waterwall section are taken from Seltzer et al. The power plant uses an air-fired supercritical pulverized coal boiler. The waterwall section has 24 burners, 3 sets of 4 burners on a pair of opposing walls. In this work there are four state variables, inputs metal temperature, O_2 and SO_2 concentrations are considered as algebraic states variables, and corrosion depth is considered as differential state variable. For O_2 concentration and metal temperature, the model relating changed induced in the algebraic state to corresponding inputs is formulated using neural network (NN). Whereas for SO_2 concentration such model is formulated using first principles.

Three types of corrosion depth values are calculated, each using a distinct set of algebraic states. The algebraic states calculated from unaltered NN model are called model algebraic states. Corrosion depth calculated using these model algebraic states are referred to as model corrosion depth. The algebraic states calculated from a modified NN model with altered parameters to induce mismatch are called true algebraic states. The corrosion depth calculated using true algebraic states are referred to as true corrosion depth. The corrosion model with same parameters is used to create true and model corrosion depths. To the true algebraic states, zero mean Gaussian noise is added to create measurements of algebraic states. Likewise, a zero mean Gaussian noise with a different variance is added to the true corrosion depth values to create measurements of corrosion depth.

Corrosion formation is a complex process; hence, mismatch is expected between the model and actual corrosion depth. This reality is being mimicked by creating true and model values that have a mismatch. The assumption in this work is that model is overpredicting the truth, measurements are closer to the truth but possess noise. Parameters used to create model algebraic states are used in process model of UKF. Noisy measurements which are close to the truth are used as sensor measurements. The spatial and temporal variation of UKF estimate, measurement and true value of corrosion depth are presented separately in Figure 64 and Figure 65 respectively.

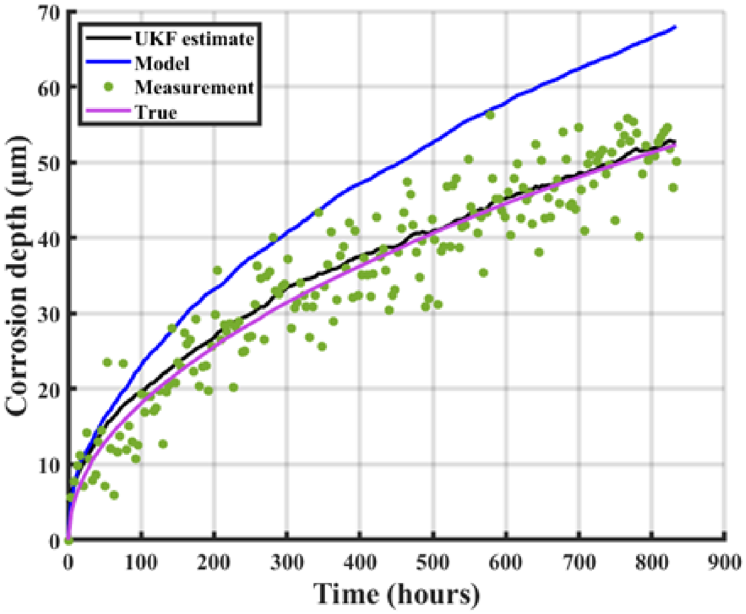

Figure 64: Spatial variation of UKF estimates, sensor measurements, model, and true values of corrosion depth (µm) along waterwall

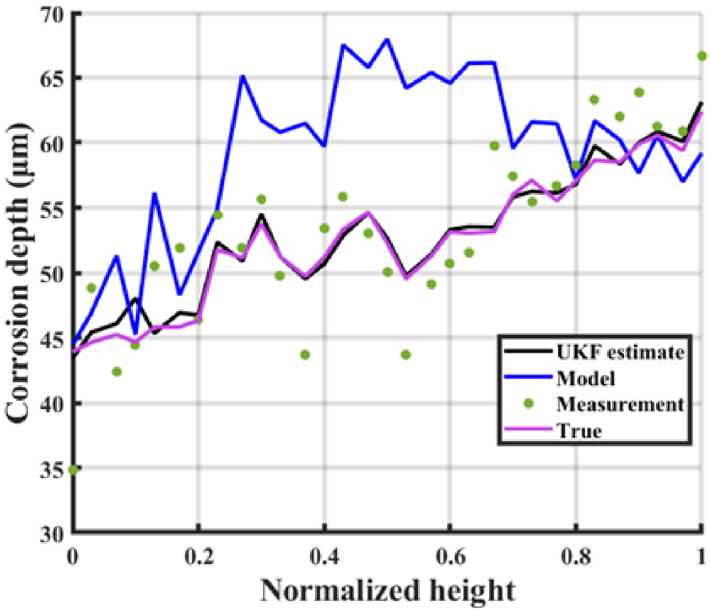

Figure 65: Temporal variation of UKF estimates, sensor measurements, model, and true values of corrosion depth (µm) at candidate location 16 on waterwall

The noisy measurements of corrosion depth are scattered around the true values of corrosion depth. True values of corrosion depth are for reference only and are used nowhere in the estimator. Despite using measurements having high noise and there being large disparity between model and measurements, UKF is performing exceptionally, as the UKF estimates are very close to the true values. In this analysis, more trust is placed on the measurements.

The corrosion rate varies significantly with location due to the dynamic nature of algebraic states. When a corrosion sensor is absent at a certain location, the accuracy of the UKF estimate drops significantly. Corrosion development is a localized phenomenon, where the corrosion rates between two adjacent locations are only related through their inputs. Hence, the potential improvement in corrosion depth estimates due to the placement of algebraic states sensors is evaluated. In the best case, all four types of sensors are presented at all candidate locations. In worst case, all four types of sensors are absent at all locations. The comparison of the best and worst case UKF estimates with the true, model and measurement values of corrosion depth are presented in Figure 66.

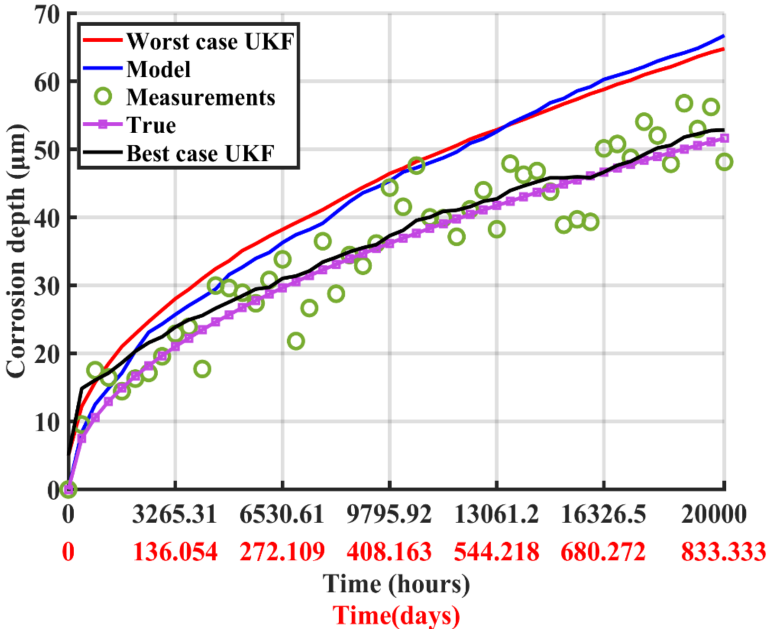

Figure 66: Comparison of UKF estimates under best and worst cases with model, true and measurement values of corrosion depth (µm)

As expected, the best case UKF estimates of corrosion depth quickly converge and stay close to the true with any fluctuations despite using noisy measurements and model with mismatch. On the other hand, worst case UKF estimates are close to the model values. These estimates from the two extreme cases show a significant improvement in estimation accuracy due to sensor placement. The location, type and number of sensors significantly impact estimates' accuracy. Using this as basis, optimal sensor placement was identified.

(4) Economic analysis

According to State of Reliability (SOR) (NERC 2018) report by North American Electric Reliability Council (NERC), coal-fired power plants have the highest forced outage rate of all conventional fuels. Boiler tube leaks are one of the leading causes for these forced outages. Waterwall tubes are one of the dominant locations for boiler tube leaks leading to about 6-7% loss in production time due to forced outages over the past several years. For instance, as per the State of Reliability (SOR) 2018 report, about 17.3 TWh of potential electricity production was lost. The forced outage prevented due to sensor placement improves plants’ availability, in turn increasing potential revenue gain. The aim of this work is to consider the increased availability of the coal fired power plants and estimate the demand and price of electricity by taking market elasticity into account. The improved plant availability can enable the plant to produce more electricity. But the profit the plant will make depends on the market demand and price. Due to similar improvements in the availability of other plants, and due to rapid deployment of renewables, stochasticity in the market demand and price is high. Several factors like population growth, industrial growth, and technological improvements in renewable and non-renewable energy technologies also affect the market dynamics and in turn cost of electricity.

This stochasticity in the electricity demand and price over the specified number of years are taken into account by energy market forecasting software programs and enable consideration of increased availability due to sensor network installation.

Software programs like National Energy Modeling System (NEMS), Long-range Energy Alternatives Planning system (LEAP), The Integrated MARKAL-EFOM System (TIMES) are used for energy trends prediction and planning.(Mirakyan and De Guio 2013) NEMS by Energy Information Administration (EIA) is a widely employed software especially in the U.S. which can be used to project the energy, economic, environmental, and security impacts of alternative energy policies and different assumptions about energy markets. The projection horizon is approximately 25 years into the future. The installation and execution of models through NEMS is convoluted and presents many challenges, as it not a commercial program and does not have official community forum for quires and discussions. LEAP is a software tool used for energy policy analysis and climate change mitigation assessment developed at the Stockholm Environment Institute (SEI). LEAP includes a Technology and Environmental Database (TED) that provides extensive information describing the technical characteristics, costs, and environmental impacts of a wide range of energy technologies. But the source of this data is unspecified as LEAP is not confined to one specific region. Since the interest is in U.S. energy market, appropriate data is desired. The ideal software program was TIMES, which enabled the modeling of U.S. energy system through database EPAUS9rT. TIMES model generator explores possible energy futures that meets the energy service demands, based on scenarios, inputs and constraints. The EPAUS9rT is a 9-region database representation of the U.S. energy system developed by U.S. Environmental Protection Agency (EPA) researchers. The database is updated with every major release of EIA's Annual Energy Outlook (AEO) report.

(5) Reference case analysis

The EPAUS9rT database is subdivided into various sectors, like electricity production sector, transportation sector etc. Processes are identified using technology/process name, input commodity and output commodity. EPAUS9rT model is executed in TIMES and using appropriate identifiers electricity production by coal-fired power plants (CFPP) is extracted. This is compared with 2020 AEO report's predictions in Figure 67.

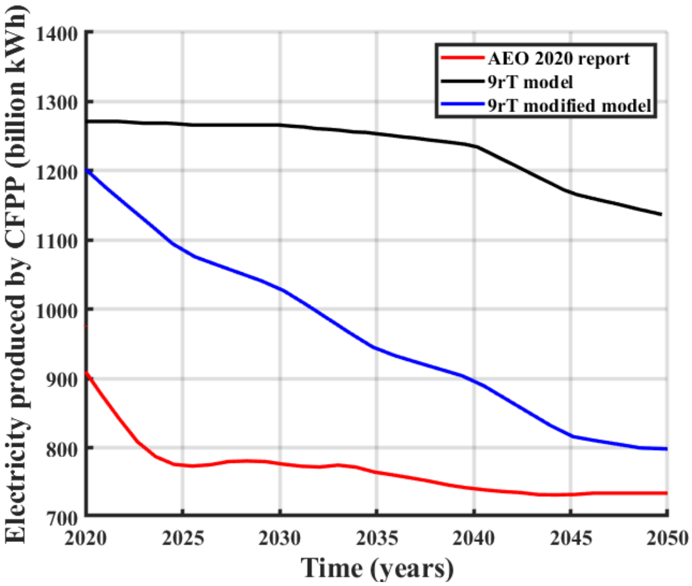

Figure 67: Comparison of the amount of electricity generated by CFPP (billion kWh) from modified and unmodified EPAUS9rT model with AEO 2020 report's predictions

The electricity produced by CFPP in the U.S. calculated by the EPAUS9rT model (9rT model) decreases with time, similar to AEO 2020 report's predictions. But this is a significant trend disparity compared to AEO's predictions. After analyzing AEO report and EPAUS9rT database, several assumptions differed, which caused the distinction, some of which are listed below.

Due to federal tax credits, higher state-level renewable targets, etc., the capital costs for wind and solar power technologies decline according to AEO.

Electricity generation from renewable sources increases, biggest contributor being solar photovoltaic technology. In EPAUS9rT, the investment cost for the installation of new solar technologies does decrease with time. But the rate at which it decreases is not significant. In addition, the fixed operation and maintenance (O&M) costs for solar and wind technology remained constant with time.

In EPAUS9rT, the investment cost for the installation of new solar technologies does decrease with time. The rate at which it decreases varies depending on location, type of technology, etc. In some cases, the decrease is not significant. In addition, the fixed operation and maintenance (O&M) costs remained constant with time. The investment cost for the installation of new wind technologies does not have a fixed trend. In some cases, it increases, while in other cases it remains constant. The fixed O&M costs remain constant with time.

According to AEO, natural gas consumption in the electric sector decreases up to 2030 and after which it increases. But electricity generation from natural gas increases up to 2050. In EPAUS9rT, natural gas consumption for electricity generation does not follow this trend.

The electricity produced by coal reported in AEO 2020 report is significantly lower due to the assumptions that solar and wind renewable technologies' costs decrease and, natural gas prices decrease. These assumptions favor electricity production technologies that use natural gas, wind, and solar power, in turn reducing electricity produced by coal. Scenarios mimicking such predictions were absent in EPAUS9rT model, causing the deviation. Therefore, EPAUS9rT model is modified by adding scenario where fixed O&M and investment costs related to solar and wind technologies is decreased by 60% up to 2050. Additionally, natural gas consumption is increased by 20% up to 2050. The electricity produced by CFPP by the model with this scenario (9rT modified model) is much closer to the AEO predictions as seen in Figure 67, validating the model.

(6) Uncertainty in CFPP

Analysis is conduction to find the effect of increased availability on CFPP production. A scenario is created that increases availability of CFPP as a result of the installation of the corrosion sensors, this applies to all CFPP in U.S. To do so, all the processes that have coal as input commodity and electricity as output commodity are selected. The existing availability factors of these technologies ranged from 82% to 94%. All their availabilities are increased to 98%. The EPAUS9rT model is run, and the electricity produced by coal fired power plants in the U.S. under this scenario is calculated and presented as "9rT model (Case 1)" in Figure 68. With the scenario of increased availability of CFPP the electricity production has increased, with a maximum improvement of 50 billion kWh in 2035. But is still possess the same decreasing trend, and in some years like 2040 and 2045 the improvement over the unaltered model's results is less than 30 billion kWh. This is due to the following reasons:

Scenario just increases availability of coal-fired power plants. But if the cost required to produce electricity by CFPP is more than other technologies, then CFPP will not selected.

In EPAUS9rT model, renewable technologies' investment cost for new facilities decreases with time. Though there is no definite trend in fixed operating costs for renewable technologies, they are of relatively lower value than that of CFPP. Thus, pre-loaded scenarios and base data present in EPAUS9rT favor renewable technologies. In that case, the electricity produced by renewable technologies would be cheap.

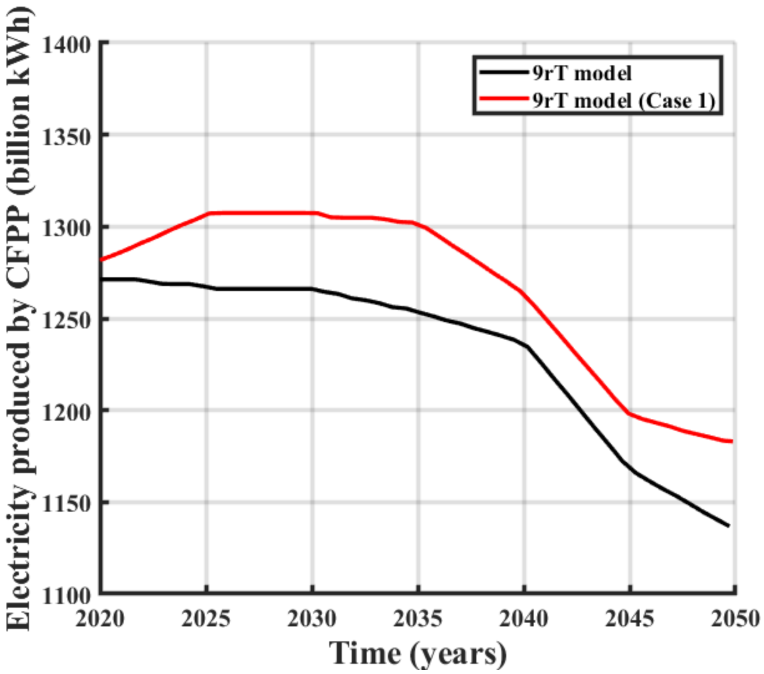

Figure 68: Comparison of amount of electricity generated from CFPP (billion kWh) from EPAUS9rT model with and without case 1 considerations

It is evident from above mentioned reasons that merely increasing the availability of CFPP will not significantly increase their share of electricity production, and other factors also play an important role. According to AEO, a shift in electricity production from coal to natural gas is expected due to the competitive pricing of natural gas. In addition, battery storage is predicted to reach up to 17 GW by 2050. This will help when there is excess production from non-dispatchable renewables like wind, and solar. Therefore, renewables, particularly solar and wind technologies, are expected to grow in the foreseeable future whereas electricity produced from natural gas increases. Hence, technologies in the energy market that significantly affect CFPP electricity production are identified: solar technology, wind technology and natural gas technology. CFPP generation is analyzed under uncertainties in each technology.

(7) Uncertainty in renewable technologies

The behavior of the energy market is analyzed when only renewable technologies wind and solar are uncertain. The model is run under three cases, each case has scenarios that deal with the same solar and wind technologies. But the degree to which they deviate from reference case varies. The cases and their corresponding scenarios are tabulated below.

Table 13: List of the cases and their corresponding scenarios implemented in EPAUS9rT model execution

Case Number	Technologies			
	Solar		Wind	
	Fixed O&M	Investment cost	Fixed O&M	Investment cost
Case 2	↓ 75%	↓ 75%	↓ 80%	↓ 70%
Case 3	↑ 120%	↑ 100%	↑ 110%	↑ 110%
Case 4	↓ 55%	↓ 60%	↓ 67%	↓ 57%

In Case 2, very high growth in renewables is considered, which is achieved by drastically lowering the fixed O&M and investment costs. In Case 3 renewables are heavily discouraged by increasing the costs. Case 1 and case 3 are extremities, while case 4 represents moderate growth in renewables where the magnitude of cost increase is slightly less than in case 1. The electricity produced by CFPP in each case is presented in Figure 69.

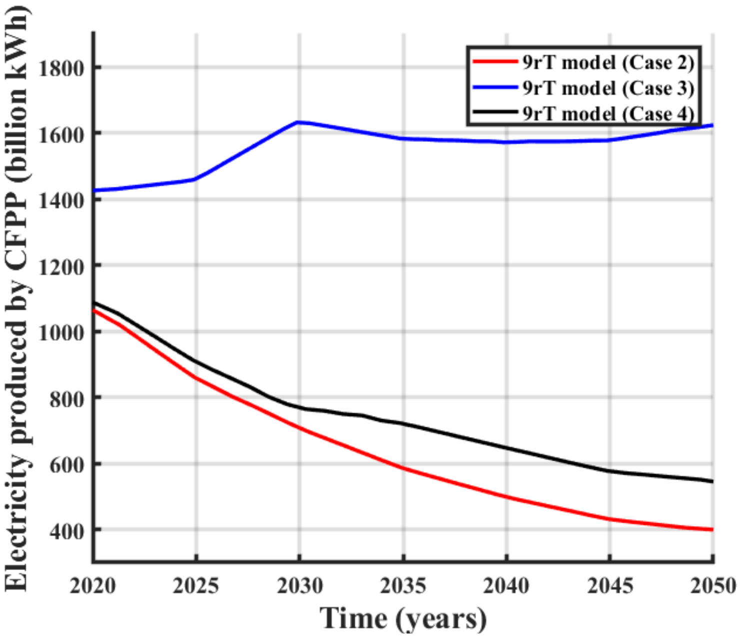

Figure 69: Comparison of amount of electricity generated from CFPP (billion kWh) from EPAUS9rT model under cases 2, 3 and 4

Electricity produced by CFPP under case 2 is the lowest of the three cases and decreasing with time because the energy market favors renewables due to their low cost. Under case 3, electricity produced by CFPP increases time and has greatly increased when compared to case 2. While under case 4 where the growth is intermediate, so is the CFPP generation. The growth of renewables has profound impact on the CFPP generation.

(8) Uncertainty in natural gas combustion cycle technology

The effect of natural gas on electricity produced by CFPP is analyzed by creating four scenarios. In these scenarios natural gas power plants' fixed O&M costs, and investment costs for new capacity were increased by 10%, 30%, 60%, and 90%, respectively. In each scenario, no other technology was altered except for natural gas. The electricity produced from coal and natural gas under each scenario is presented in Figure 70 and Figure 71 respectively.

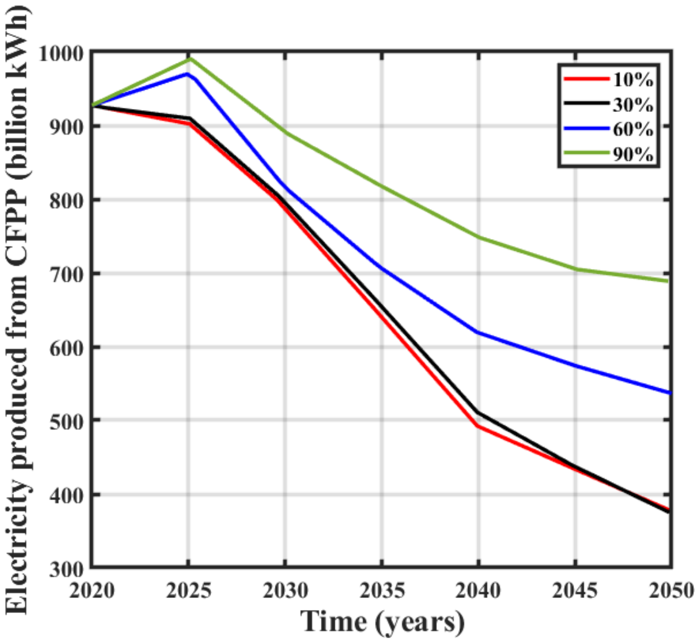

Figure 70: Electricity produced from CFPP under 4 scenarios with increasing costs related to natural gas technology

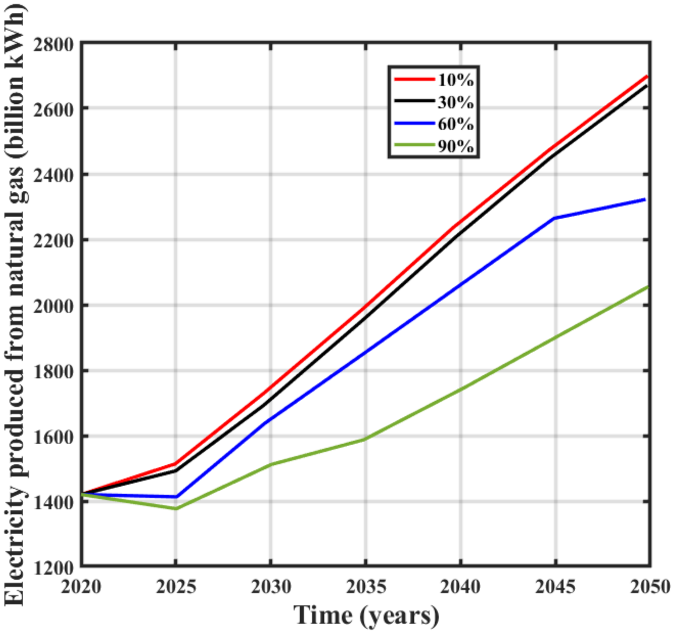

Figure 71: Electricity produced from natural gas under 4 scenarios with increasing costs related to natural gas technology

Discouraging natural gas technology by increasing related costs resulted in increased electricity produced from CFPP, with noticeable difference when costs increase by 60% and above. Simultaneously, electricity produced from natural gas decrease with increasing costs. Natural gas has a significant effect on electricity produced by coal.

(9) Uncertainty in multiple technologies

There is a possibility that there can be deviations from the assumptions made in AEO. For instance, technological development might not reduce the operating cost for solar technologies as assumed. Hence, electricity production from CFPP under such deviations is studied. These deviations are implemented in TIMES by using various scenarios. Random deviation of variables in these scenarios from their current base values is generated using Latin Hypercube Sampling (LHS). In general, there is a normal demand for electricity in the market. In the near-random scenarios generated by LHS, the energy market's stability is disturbed by favoring some technologies over the others. Then the other technology is expected to supply more electricity to fill the shortfall and meet the demand. The following table lists all the variables that significantly impact electricity production from CFPP. Addition of natural gas price to this list is based on the current global scenario, where restrictions on natural gas supply can change their price.

Table 2: Key variables in EPAUS9rT database that impact electricity production from CFPP

Type of technology		Variable
Renewable sources	Solar	Fixed O&M
		Investment cost
	Wind	Fixed O&M
		Investment cost
Non-renewable sources	Natural gas	Fixed O&M
		Investment cost
		Price
	Coal	Fixed O&M
		Variable O&M
		Availability

CFPP electricity generation is initially analyzed under two scenarios, considering four variables (solar and wind technologies' fixed O&M and investment costs). Five sets of values are generated for these four variables considering standard deviation of 10-20%. In the same manner, five sets of random values are generated by LHS for the availability of the coal-fired power plants. The analysis is conducted in the following manner.

Scenario 1: The five sets of values for the four variables representing wind and solar technologies and additional five sets of values for coal-fired power plants' availability are incorporated. Thus, five separate runs have been executed.

Scenario 2: The five sets of values for the four variables representing wind and solar technologies are incorporated, and five separate runs have been executed.

The difference between scenarios 1 and 2 is that, in scenario 1 CFPP availability is changed. In scenario 2, availability of CFPP is unchanged. Thus, the difference in results between scenario 1 and 2 gives a measure of the impact of the availability of the CFPP.

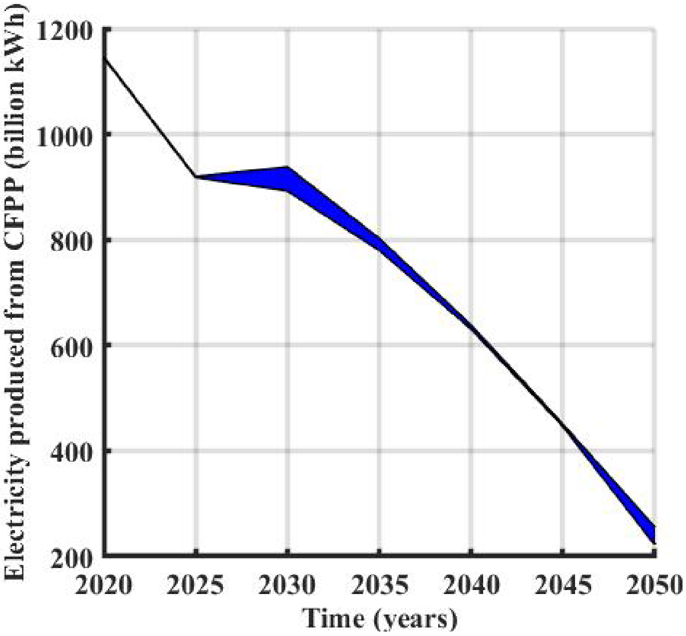

Figure 72: Region showing the electricity produced from CFPP for 5 runs, under scenario 1

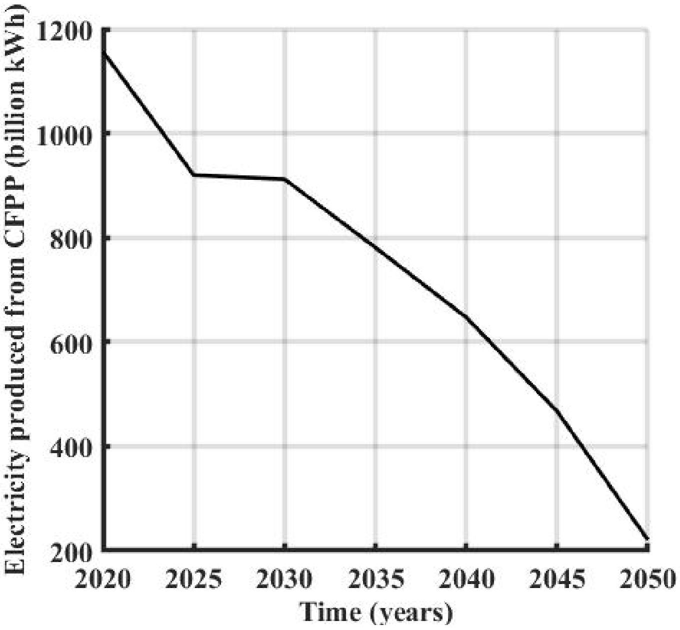

Figure 73: Region showing the electricity produced from CFPP for 5 runs, under scenario 2

Figures 72 and 73 show the results for scenario 1 and 2, respectively. The results show that the random changes considered in the four variables has negligible impact on CFPP electricity production. Comparatively random change in the availability of the CFPP do have a larger impact. A new analysis is conducted, where renewable technologies are subjected to random changes using LHS, but natural gas is specifically discouraged. Natural gas was identified to be the primary influencer, this analysis helps in understanding its magnitude of influence on CFPP production, under variability in renewable technologies.

Three sets of values are generated by LHS for the four variables (solar and wind technologies' fixed O&M and investment costs). A standard deviation of 10-20% is considered. Separately, three scenarios are created where natural gas related costs from Table 13 are increased by 10%, 50% and 100% respectively. Three separate scenarios are created where availability of CFPP was increased 5%, 10%, and 15% respectively. The analysis includes three cases, and in each case three sets of values are generated by LHS for the four variables representing wind and solar technologies. Thus, three separate runs have been executed. The differential scenario in each are as follows:

- Case A: In each run, the scenario where costs related to natural gas from Table 13 are increased by 10% is included.

- Case B: In each run, the scenario where costs related to natural gas from Table 13 are increased by 50% is included.

- Case C: In each run, the scenario where costs related to natural gas from Table 13 are increased by 100% is included.

In all of the above cases CFPP availability was not changed. The difference between the cases is the increase in natural gas related costs. The electricity produced by coal-fired power plants in each case is presented below.

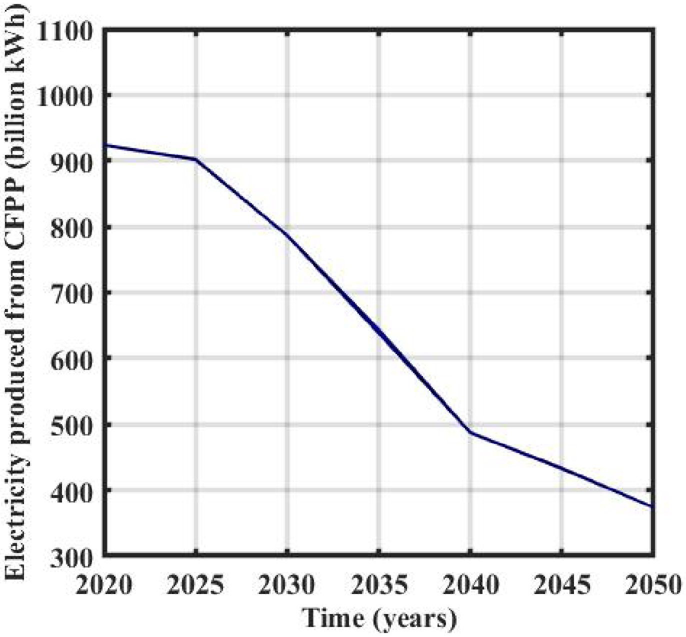

Figure 74: Region showing the electricity produced from CFPP from Case A

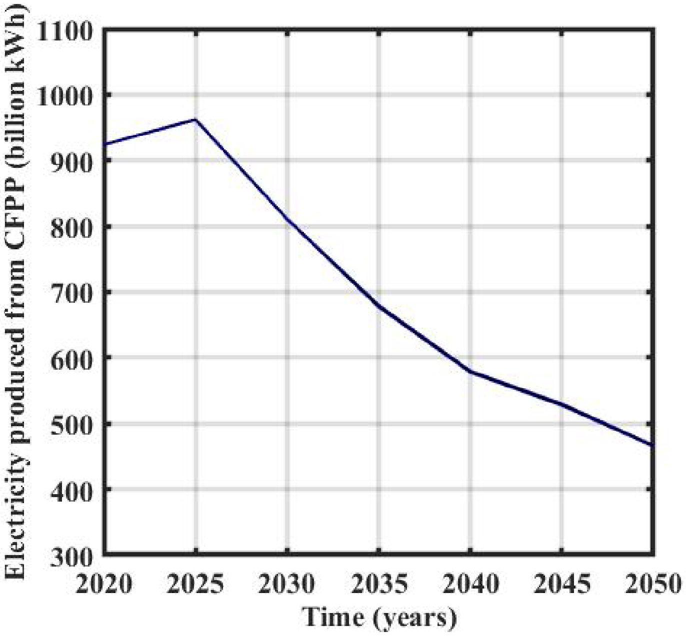

Figure 75: Region showing the electricity produced from CFPP from Case B

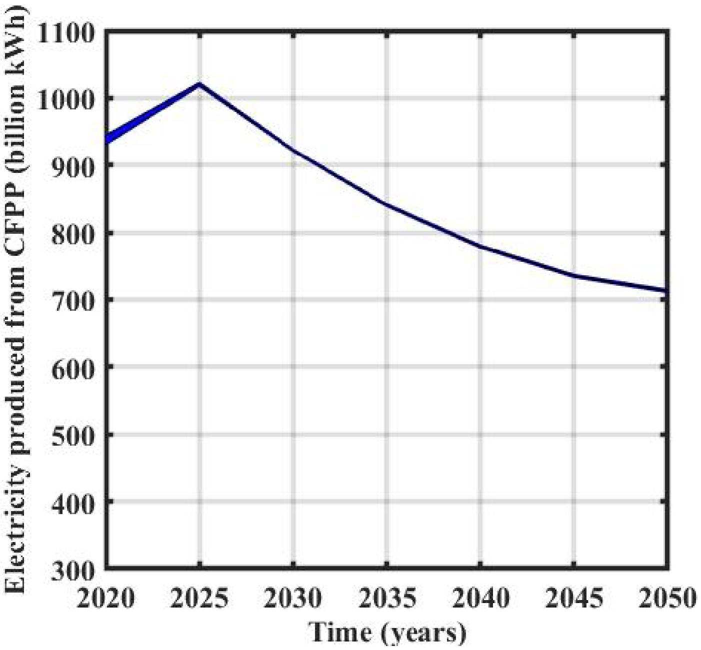

Figure 76: Region showing the electricity produced from
CFPP from Case C

Figures 74-76 show CFPP potential production, where it significantly increases from case 1 to case 3, which is expected, since from case A to case C the natural gas technology's related costs increase.

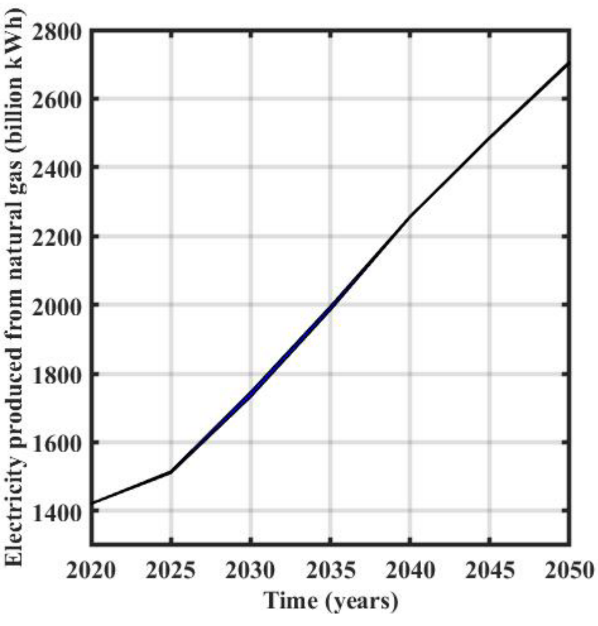

Figure 77: Region showing the electricity produced from natural gas from Case A

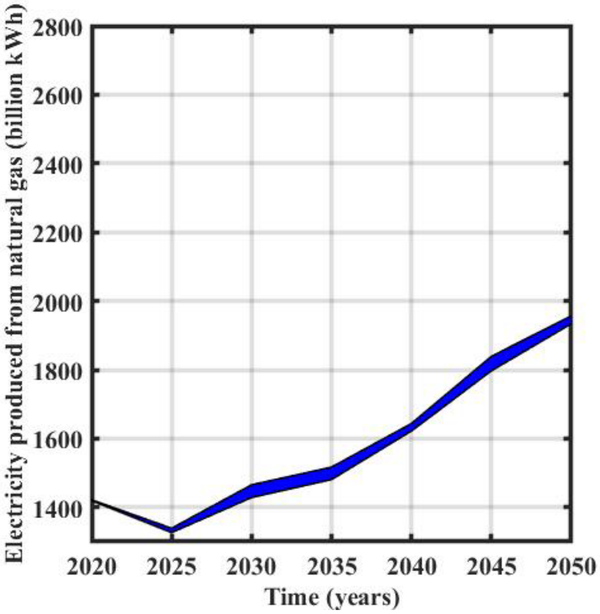

Figure 78: Region showing the electricity produced from natural gas from Case C

In Figures 77-78, the natural gas technology's potential production is shown. The production decreases significantly from case A to case C, which is due to the increase in costs related to natural gas technologies.

The random scenario analysis conducted using LHS so far have few number of runs. A superior near random scenario is generated in the following analysis using large number of runs. CFPP electricity generation is calculated under three new cases. Each case mimics a possible future, where energy market deviates from prediction. In each case, 50 random scenarios based on LHS are generated and the model is executed 50 times. Electricity produced by CFPP from all the 50 runs in each case are compiled and analyzed.

Case 1:

In this case, a future scenario is created where solar, wind, and natural gas technologies have some uncertainties. All variables listed in table 14 corresponding to these technologies are subjected to random changes using LHS. Fifty sets of values are generated by LHS for the 7 variables. The region within which the potential electricity produced by corresponding technology lies is presented in Figure 79, Figure 80, and Figure 81.

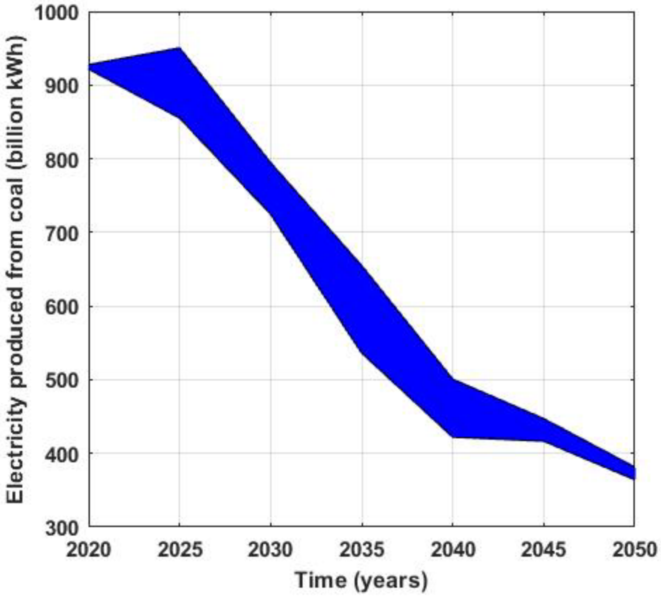

Figure 79: Region showing the potential electricity produced from CFPP from case 1

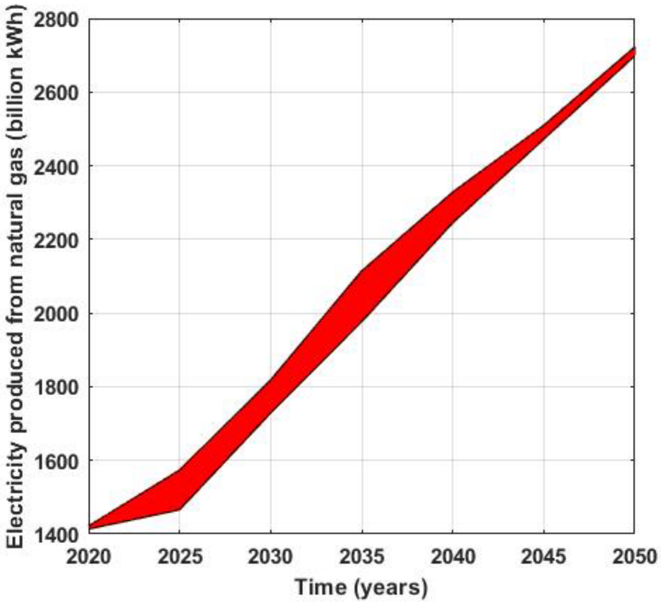

Figure 80: Region showing the potential electricity produced from solar power from case 1

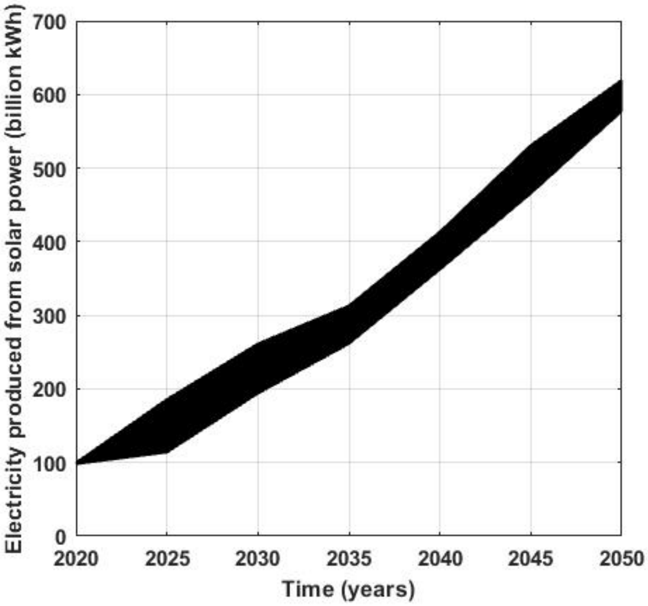

Figure 81: Region showing the electricity produced from solar power from Case 1

Due to significant variation in variables related to solar, wind and natural gas technologies, the region of potential electricity production is large for these solar and natural gas technology as seen in Figure 80 and Figure 81. Interestingly, CFPP potential production also varies significantly even though we did not change any variable related to it, seen in Figure 79. Thus, in a future with uncertainty in solar, wind, and natural gas technologies, CFPP potential production also fluctuates.

Case 2:

In this case, a future is created where only CFPP technologies have some instability. Fixed O&M costs and variable O&M costs related to CFPP are subjected to random changes. Fifty sets of values are generated by LHS for these two variables. Thus, fifty separate runs have been executed. In each run, existing availability is increased by a fixed amount of 20% which is assumed due to sensor placement. The region within which the potential electricity produced by CFPP, and natural gas may lie is presented in Figure 82 and Figure 83 respectively.

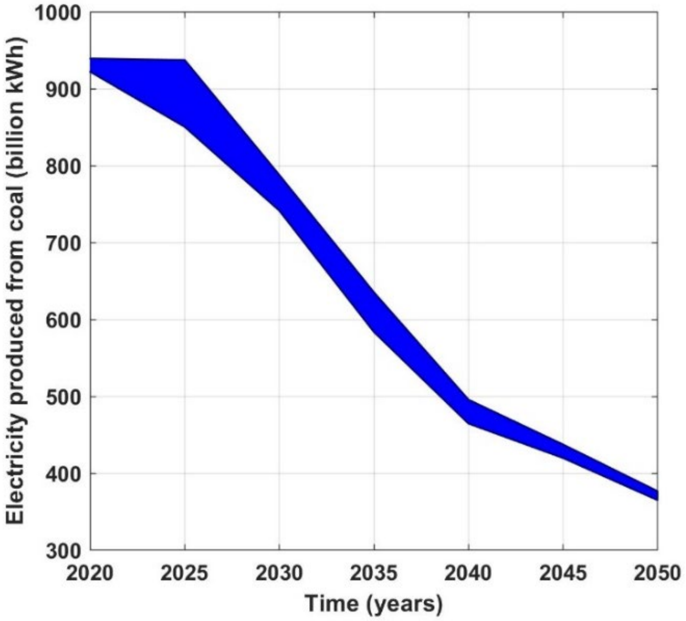

Figure 82: Region showing the electricity produced from CFPP from Case 2

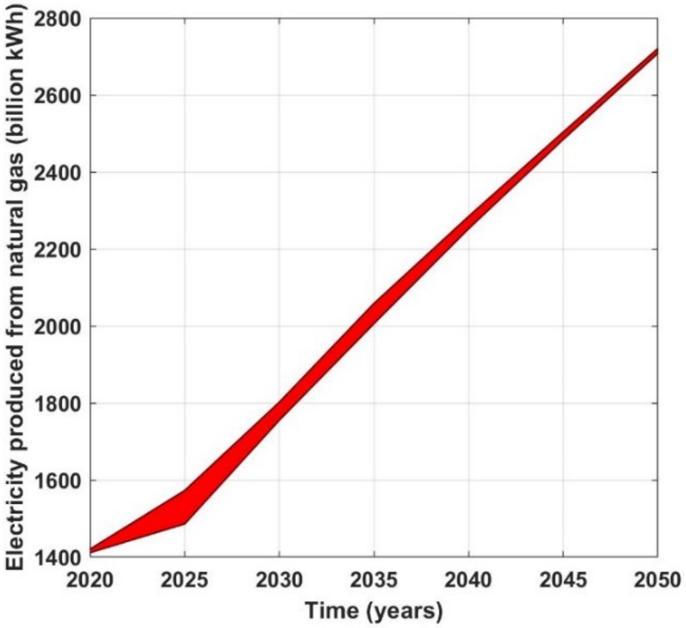

Figure 83: Region showing the electricity produced from natural gas power plants from Case 2

In this case, the potential electricity production from CFPP (seen in Figure 33) varies significantly when along with availability, fixed and variable O&M costs are varied. Also, changes in coal technologies have an effect on electricity production from natural gas technologies, seen in Figure 83. Thus, instability in coal-fired power plant technologies not only alters the potential electricity production of CFPP, but also that of other technologies.

Case 3:

In this case, a future is created where solar, wind, natural gas, and coal-fired electricity production technologies have some uncertainties. In this compound case all variables listed in Table 14 are subjected to random changes using LHS, except for CFPP availability which is increased by 20%. Fifty sets of values are generated by LHS for these nine variables. Thus, fifty separate runs have been executed where in each run existing CFPP availability is increased by 20%.

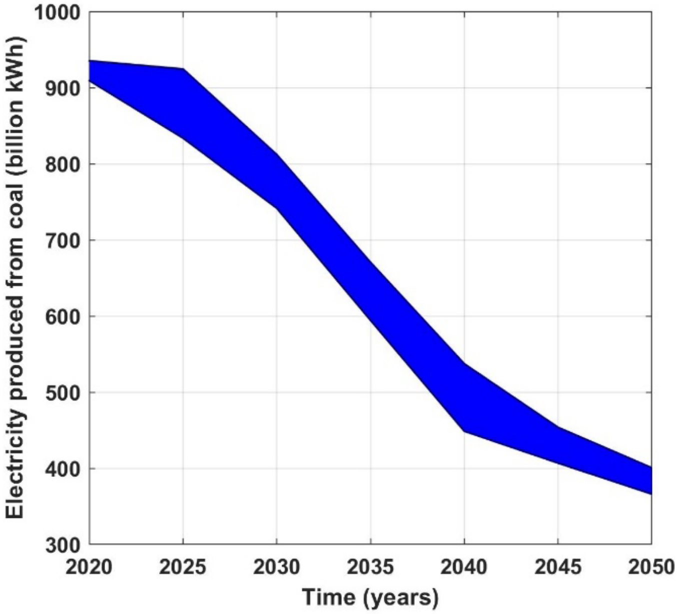

Figure 84: Region showing the electricity produced from CFPP *from Case 3*

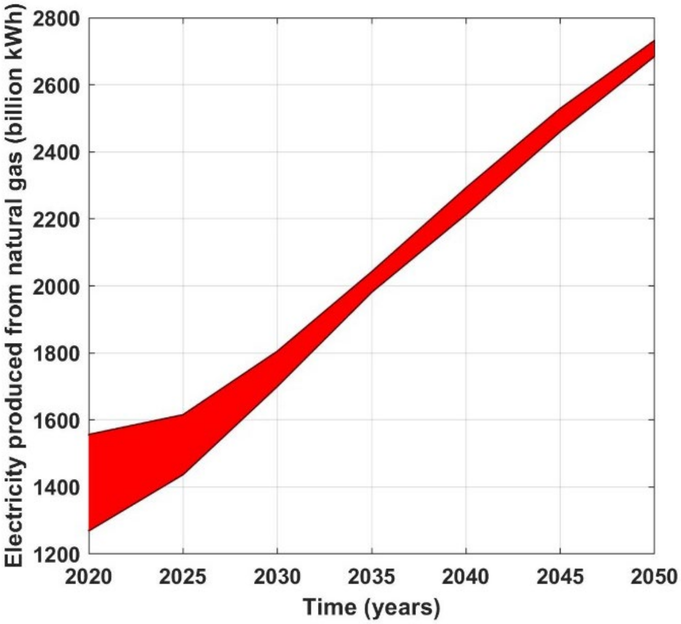

Figure 85: Region showing the electricity produced from natural gas power plants from Case 3

In this complex case where variables related to multiple technologies vary, the potential electricity production from CFPP is varying significantly. Region of potential electricity generation from CFPP is comparable to that from case 1 but is slightly broader. The electricity produced by natural gas technologies is slightly less than that from case 1, which is evident by comparing sizes of regions from Figure 81 and Figure 85. The electricity produced by natural gas is less, but to meet the market demand, CFPP supplied the necessary electricity which is why their production is higher. Thus, in this near random scenario where various technologies are unstable, but CFPP availability increased, prompted the coal-fired power plants to produce more electricity.

(10) Cost of sensors

Multiple sensor placement networks are considered and for each network the corresponding investment cost is calculated. Each candidate location is equally likely to fail if corrosion depth exceeds the threshold. Each sensor network provides an estimated time of failure. If estimated time of failure is close to the true time of failure within tolerance, then failure at that location is considered to be avoided. For each sensor network, investment cost is calculated and denoted by $\sum \boldsymbol{C_j S_j}$, where C_j denotes the cost of sensor and S_j denotes the presence or absence of sensor at each candidate location. The sensor network aims to maximize the NPV of the sensor network, considering the tradeoff between investment cost and potential revenue gained by coal-fired power plants (CFPP) due to avoiding forced outage, which is expressed by equation 1.

$$max\ (NPV) = -\sum C_j S_j + \int_0^{t_{life}} [R_S(x,t) - R_{NS}(x,t)]dt \tag{1}$$

Here, RS is the revenue gained by CFPP under sensor network. RNS is the revenue gained by CFPP under no sensor network. The net potential revenue gained over a time span of 30 years (from 2020 to 2050) is calculated.

For the cost of each type of sensor two extremities are considered, one being the low-cost case and the other high-cost case.

- Metal Temperature sensors: Temperature sensors with method of detection based on fiber optics, filled element liquid (with gas or mercury), pyrometers suction (pneumatic), radiation pyrometers, platinum resistance bulb, and certain special types of thermocouples are capable for operating in temperatures up to at least 1094^{o}C. Cost of these sensors are in two ranges, between \$200 to \$1000, and above \$1000. Waterwall is in a corrosive environment at high temperature, and superior materials of construction are needed for use in such environment.

- O_2 concentration sensors: High temperature zirconium oxide oxygen detectors are considered for measuring O_2 concentration, as they suitable for corrosive environment, can be inserted into the process as a probe and can operate up to 1593^{o}C. Their cost varies between \$5,000 and \$10,000.

- SO_2 concentration sensors: Exact cost information for a high temperature SO_2 concentration sensor was not readily available in open literature. SO_2 sensors with method of detection based on conductimetry, photometry, thermal conductivity are limited to ambient air analysis. Sensors employing technologies like infrared, correlation spectrometry are used for stack gas analysis and hence can be used for high temperature. Permanently installed multiple gas analysis sensor cost varies between \$10,000 and \$20,000.

Hence, based on the above inferences, for metal temperature, SO_2 and O_2 concentration sensors, a low-cost of \$5,000 and a high-cost of \$10,000 is considered.

- Corrosion sensor: Considering the R&D costs, installation costs and cost for materials of construction, a low-cost of \$20,000 and a high-cost of \$40,000 is considered.

(11) Return on investment analysis

The waterwall section is divided into 31 evenly spaced candidate locations along height. The candidate locations layout is depicted in 4. At each candidate location, a sensor can be placed for corrosion depth, metal temperature, SO_2 and O_2 concentrations respectively. ‘1’ (highlighted in green) in a cell indicates that corresponding sensor is present at that location, whereas ‘0’ (highlighted in red) indicates the absence of that sensor. The corrosion depth estimates are calculated under multiple cases, each with a different sensor placement. Temporal variation of UKF estimates of all states is analyzed under each case.

Table 14: Candidate locations layout for sensor placement

	Sensor type			
Candidate Location	x	T_m	O_2	SO_2
31				
30				
…				
2	1	0		
1				

- Best and worst cases: In the best case, all four types of sensors are presented at all candidate locations. In worst case, all four types of sensors are absent at all locations. The UKF estimate of algebraic states under best case are close to the truth due to utilization of measurements. The worst case UKF estimates are close to the model values due to absence of measurements. Based on the individual sensor costs, the total investment cost in sensor network for best case under high-cost case is \$2.17M. And under low-cost case is \$1.08M.
- Intermediate cases: In case 1, corrosion sensors are absent at all locations whereas all types of algebraic states are present at all locations. The investment under high-cost case is \$930k, and under low-cost case is \$465k. Case 2 is an intermediate case, where corrosion sensors are still absent at all locations. SO_2 concentration sensors are present all locations. The burners are generally present between locations 1 and 16 and sensor placement can be infeasible at these locations. Hence, metal temperature and O_2 concentration sensors are present only from locations 17 through 31. The investment cost for sensor network in case 2 under high-cost case is \$610k, and under low-cost case is \$305k. The layout of sensors for these cases is presented in Figure 86 and Figure 87 respectively.

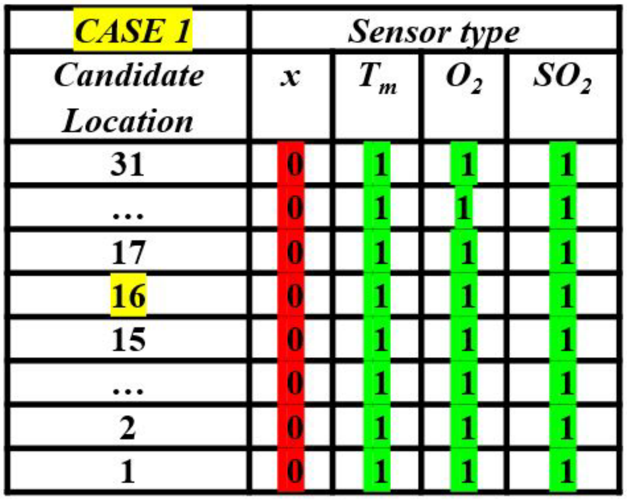

CASE 1	***Sensor type***			
Candidate Location	x	T_m	O_2	SO_2
31	0	1	1	1
…	0	1	1	1
17	0	1	1	1
16	0	1	1	1
15	0	1	1	1
…	0	1	1	1
2	0	1	1	1
1	0	1	1	1

Figure 86: Sensor placement layout under case 1

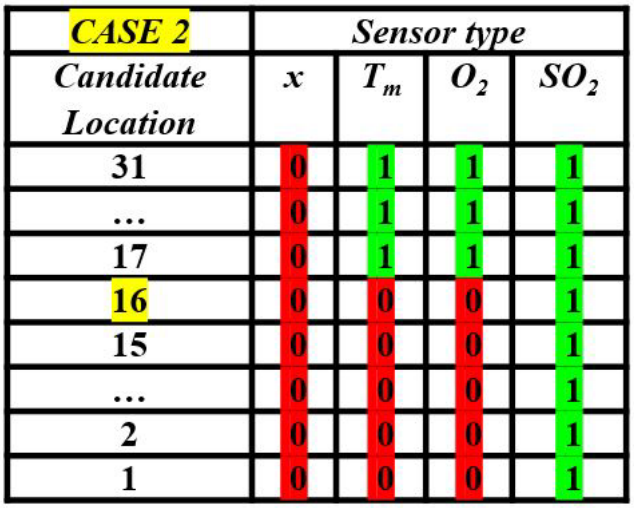

CASE 2	**Sensor type**			
Candidate Location	x	T_m	O_2	SO_2
31	0	1	1	1
…	0	1	1	1
17	0	1	1	1
16	0	0	0	1
15	0	0	0	1
…	0	0	0	1
2	0	0	0	1
1	0	0	0	1

Figure 87: Sensor placement layout under case 2

From the economic analysis, case 1 represents a future scenario where solar, wind, and natural gas technologies have some uncertainties. Case 3 represents a future scenario where solar, wind, natural gas, and coal-fired electricity production technologies have some uncertainty. Hence, the difference in revenue gained between case 1 and case 3 is due to the placement of sensors. The region within which the potential electricity production lies is bounded by the maximum possible and minimum possible electricity production. The maximum and minimum possible change in electricity produced by each CFPP per year is calculated from results of cases 1 and 3 and presented in Figure 88.

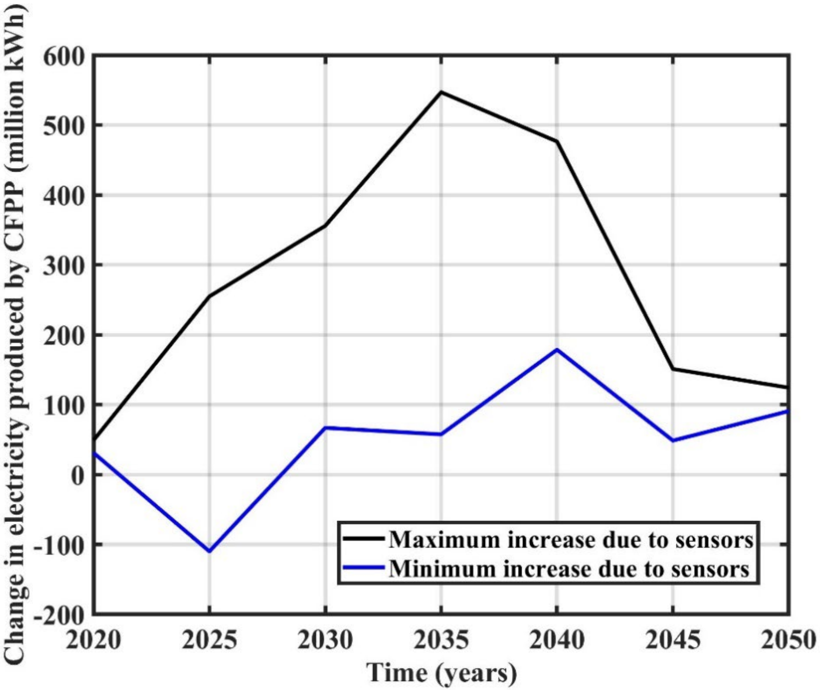

Figure 88: Maximum and minimum change in electricity produced by each CFPP between case 1 and case 3 in million kWh

There are 229 operational CFPP in U.S, and the production presented in Figure 88 is the change in revenue per plant. According to U.S. EIA, the average nominal retail electricity price in 2021 is $ 0.1372 per kWh. The change in electricity production is multiplied with 2021 price of electricity to obtain yearly potential increase in revenue per plant. Subtracting the investment cost in sensor network from the potential revenue increase for each case will yield the Net present value (NPV).

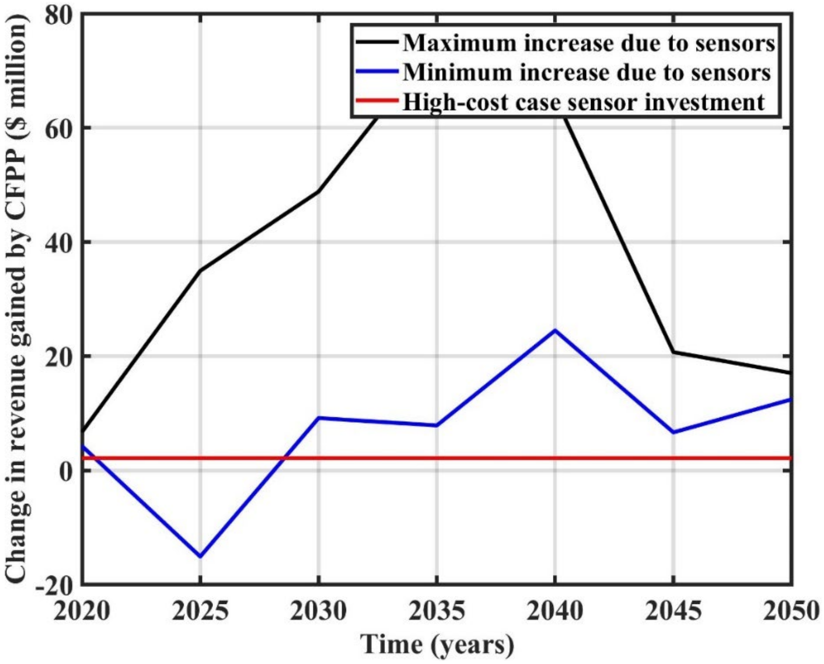

Figure 89: Change in revenue gained by each CFPP compared to the high-cost case investment cost when all types of sensors are placed

In Figure 89, the maximum and minimum possible revenue change in each CFPP is presented. The high-cost case investment cost in sensor network under best case (where all types of sensors are placed) is \$2.17M. The minimum possible increase in revenue gain by each CFPP due to sensor placement surpasses this investment cost of \$2.17M as early as 2030, indicating that best case sensor network yield profits. This implies that in an uncertain energy market with variability in solar, wind, natural gas technologies, by improving CFPP production by sensor network the plant can gain increased revenue. And recover the investment cost in sensor network by 2030, even under minimum possible revenue increase.

Conclusion

A simple corrosion model was developed to calculate the corrosion depth along the waterwall section of a coal-fired boiler and was used in the estimator. The UKF estimates compare well with the 'true' values of corrosion depth along the height of the waterwall with time. Corrosion depth estimation enabled estimation of the failure time of waterwall tube due to corrosion. An increase in the overall availability of CFPP is possible by planning maintenance activities accordingly. Using energy market forecasting software (TIMES), potential revenue gained by preventing forced outages is calculated. Scenarios based analysis was performed with the aim of identifying conditions under which the potential revenue gained will be more than the investment cost of sensor network. All technologies and corresponding factors affecting CFPP production were identified. The individual degree of impact of each of these technologies on CFPP electricity production was demonstrated. A set of near-random scenarios including all effecting technologies were created using the method of Latin Hypercube Sampling. The electricity produced by CFPP with and without improved availability under these random scenarios was calculated and compiled to create a feasible region within which electricity production can lie. From the scenario-based analysis it was identified that, in the near random future with instability in various technologies, increased availability of CFPP has prompted them to produce more electricity. The investment cost in the sensors was calculated for multiple sensor placements. Investment made in sensor placement can be well recovered even with least possible increase in revenue of CFPP by 2030. This implies that the CFPP can turn and stay profitable by 2030, making the decision of investment in sensor network cost efficient.